EXPERIMENTAL AND NUMERICAL INVESTIGATIONS ON FRACTURE CHARACTERISTICS OF 3D PRINTED MATERIAL BASED ON SIZE EFFECT LAW

A Thesis Submitted to Gujarat Technological University
for the Award of

Doctor of Philosophy

in

Mechanical Engineering

by

Patel Sumitkumar Yogeshbhai
Enrollment No: 179999919059

under supervision of

Dr. Chaitanya K. Desai

GUJARAT TECHNOLOGICAL UNIVERSITY
AHMEDABAD

August 2026

DECLARATION

I declare that the thesis entitled **Experimental and numerical investigations on fracture characteristics of 3d printed material based on size effect law** submitted by me for the degree of Doctor of Philosophy is the record of research work carried out by me during the period from April 2018 to August 2026 under the supervision of **Dr. Chaitanya K. Desai** and this has not formed the basis for the award of any degree, diploma, associateship, fellowship, titles in this or any other University or other institution of higher learning.

I further declare that the material obtained from other sources has been duly acknowledged in this thesis. I shall be solely responsible for any plagiarism or other irregularities, if noticed in the thesis.

Signature of the Research Scholar: Date: 21/08/2026

Name of Research Scholar: Patel Sumitkumar Yogeshbhai

Place: Ahmedabad

CERTIFICATE

I certify that work incorporated in the thesis **Experimental and numerical investigations on fracture characteristics of 3d printed material based on size effect law** submitted by **Mr. Patel Sumitkumar Yogeshbhai** , was carried out by the candidate under my supervision/guidance. To the best of my knowledge: (i) the candidate has not submitted the same research work to any other institution for any degree/diploma, Associateship, Fellowship or other similar titles (ii) the thesis submitted is a record of original research work done by the Research Scholar during the period of study under my supervision, and (iii) the thesis represents independent research work on the part of the Research Scholar.

Signature of the Research Supervisor: Date: 21/08/2026

Name of Supervisor: Dr.Chaitanya K. Desai

Place: Ahmedabad

Course-work Completion Certificate

This is to certify that Mr. Patel Sumitkumar Yogeshbhai enrollment no. 179999919059 is enrolled for PhD program in the faculty Mechanical Engineering of Gujarat Technological University, Ahmedabad.

(Please tick the relevant option(s))

- ☐ He has been exempted from the course-work (successfully completed during PhD Course)
- ☐ He has been exempted from the Research Methodology Course only (successfully completed during PhD Course)
- ☐ He has successfully completed the PhD Course work for the partial requirement for the award of PhD Degree. His performance in the course work is as follows-

Grade Obtained in Research Methodology (PH001)	Grade Obtained in Self Study Course (Core Subject) (PH002)
AB	AA

Supervisor's Sign

Dr.Chaitanya K. Desai

Originality Report certificate

It is certified that PhD Thesis titled **Experimental and numerical investigations on fracture characteristics of 3d printed material based on size effect law** by **Mr. Patel Sumitkumar Yogeshbhai** has been examined by us. We under the following:

a. Thesis has significant new work/knowledge as compared already published or are under consideration to be published elsewhere. No sentence, equation, diagram, table, paragraph or section has been copied verbatim from previous work unless it is placed under quotation marks and duly referenced.

b. The work presented is original and own work of the author (there is no plagiarism). No ideas, processes, results or words of others have been presented as Authors work.

c. There is no fabrication of data or results which have been compiled / analyzed.

d. There is no falsification by manipulating research materials, equipment or processes, or changing or omitting data or results such that the research is not accurately represented in the research record.

e. The thesis has been checked using Turnitin Anti-Plagiarism (copy of originality report attached) and found within limits as per GTU Plagiarism Policy and instructions issued from time to time (i.e. permitted similarity index < = 10%)

Signature of the Research Scholar: Date: 21/08/2026

Name of Research Scholar: Patel Sumitkumar Yogeshbhai

Place: Ahmedabad

Signature of the Research Supervisor: Date: 21/08/2026

Name of the Research Supervisor: Dr.Chaitanya K. Desai

Place: Ahmedabad

Sumit Patel

thesis_sumit.pdf

Ph D Thesis

Phd

Gujarat Technological University

Document Details

Submission ID

trn:oid:::1:3626758831

Submission Date

Aug 13, 2026, 12:09 PM GMT+5:30

Download Date

Aug 13, 2026, 12:15 PM GMT+5:30

File Name

thesis_sumit.pdf

File Size

8.2 MB

123 Pages

23,274 Words

122,092 Characters

6% Overall Similarity

The combined total of all matches, including overlapping sources, for each database.

Filtered from the Report

- Bibliography
- Quoted Text
- Cited Text
- Small Matches (less than 14 words)

Match Groups

20 Not Cited or Quoted 6%
Matches with neither in-text citation nor quotation marks

0 Missing Quotations 0%
Matches that are still very similar to source material

0 Missing Citation 0%
Matches that have quotation marks, but no in-text citation

0 Cited and Quoted 0%
Matches with in-text citation present, but no quotation marks

Top Sources

5%	Internet sources
6%	Publications
5%	Submitted works (Student Papers)

Integrity Flags

0 Integrity Flags for Review

No suspicious text manipulations found.

Our system's algorithms look deeply at a document for any inconsistencies that would set it apart from a normal submission. If we notice something strange, we flag it for you to review.

A Flag is not necessarily an indicator of a problem. However, we'd recommend you focus your attention there for further review.

PhD THESIS Non-Exclusive License to GUJARAT TECHNOLOGICAL UNIVERSITY

In consideration of being PhD Research Scholar at GTU and in the interests of the facilitation of research at the University and elsewhere, I **Patel Sumitkumar Yogeshbhai** having (Enrollment No.) **179999919059** here by grant a non-exclusive, royalty free and perpetual license to the University on the following terms:

a) The University is permitted to archive, reproduce and distribute my thesis, in whole or in part, and/or my abstract, in whole or in part (referred to collectively as the "work") anywhere in the world, for non-commercial purposes, in all form of media;

b) The University is permitted to authorize, sub-lease, sub- contract or procure any of the acts mentioned in paragraph(a);

c) The University is authorized to submit the Work at any National/International Library, under the authority of their "Thesis Non-Exclusive License";

d) The Universal copyright notice ©shall appear on all copies made under the authority of this license;

e) I undertake to submit my thesis, through my University, to any Library and Archives. Any abstract submitted with the thesis will be considered to form part of the thesis.

f) I represent that my thesis is my original work, does not infringe any rights of others, including privacy rights, and that I have the right to make the grant conferred by this non–exclusive license.

g) If third party copyrighted material was included in my thesis for which, under the terms of the Copyright Act written permission from the copyright owners is required, I have obtained such permission from the copyright owners to do the acts mentioned in the paragraph (a) above for the full term of copyright protection.

h I understand that the responsibility for the matter as mention in the paragraph (g) rests with the authors / me solely. In no case shall GTU have any liability for any acts / omissions / error / copyright infringement from the publication of the said thesis or otherwise.

i) I retain copyright ownership and moral rights in my thesis, and may deal with the copyright in my thesis, in any way consistent with rights granted by me to my University in this no-exclusive license.

j) GTU logo shall not be used / printed in the book (in any manner whatsoever) being published or any promotional or marketing materials or any such similar documents.

k) The following statement shall be included appropriately and displayed prominently in the book or any material being published anywhere: ''The content of the published work is part of the thesis submitted in partial fulfillment for the award of the degree of Ph.D. in Mechanical Engineering of the Gujarat Technological University".

l) I further promise to inform any person to whom I may hereafter assign or license my copyright in my thesis of the rights granted by me to my University in this no-exclusive license. I shall keep GTU indemnified from any and all claims from the Publisher(s) or any third parties at all times resulting or arising from the publishing or use or intended use of the book / such similar document or its contents.

m) I am aware of and agree to accept the conditions and regulations of PhD including all policy matters related to authorship and plagiarism.

Date: 21/08/2026
Place: Ahmedabad

Signature of the Research Scholar:

Recommendation of the Research Supervisor: Recommended for Submission

Signature of the Research Supervisor

Thesis Approval Form

The viva-voce of the PhD Thesis submitted by **Shri Patel Sumitkumar Yogeshbhai (Enrollment No. 179999919059)** entitled **Experimental and numerical investigations on fracture characteristics of 3d printed material based on size effect law** was conducted at Gujarat Technological University.

(Please tick any one of the following option)

- [x] The performance of the candidate was satisfactory. We recommend that he/she be awarded PhD degree.

- [ ] Any further modifications in research work recommended by the panel after 3 months from the date of first viva-voce upon request of the Supervisor or request of Independent Research scholar after which viva-voce can be re-conducted by the same panel again.

- [ ] The performance of the candidate was unsatisfactory. We recommended that he/she should not be awarded the PhD degree.

Dr. Chaitanya K. Desai,
Research Supervisor

21/08/2026

Dr K. P. Desai,
External Examiner 1

Dr Prabhat Agnihotri,
External Examiner 2

EXPERIMENTAL AND NUMERICAL INVESTIGATIONS ON FRACTURE CHARACTERISTICS OF 3D PRINTED MATERIAL BASED ON SIZE EFFECT LAW

Submitted By
Patel Sumitkumar Yogeshbhai

Abstract

The integration of cutting-edge manufacturing techniques is gaining momentum among both researchers and industry professionals. Additive manufacturing, frequently referred to as 3D printing, continues its rapid development, revealing novel applications in diverse fields. Within the spectrum of additive manufacturing processes, Fused Deposition Modeling (FDM) stands out as a popular choice for part fabrication. However, employing FDM-produced components in larger constructions necessitates a consideration of how their mechanical properties scale.

The primary objective of this work is to characterize, both experimentally and numerically, the size effect of FDM materials. The fracture behavior of FDM parts is assessed based on their ductility level; if parts exhibit quasi-brittle behavior, the Size Effect Law (SEL) is used to evaluate fracture parameters, whereas if the behavior is ductile, the Essential Work of Fracture (EWF) method is employed.

This study investigates the mechanical and fracture properties of FDM parts made from Carbon powder-reinforced Polylactic Acid (CPLA) and Polycarbonate (PC). Dogbone specimens were fabricated according to ASTM D638-14 to evaluate mechanical properties such as the modulus of elasticity (E). Quasi-brittle behavior was observed for CPLA parts; thus, the size effect method was applied. This research examines laminates of three different thicknesses, maintaining a constant raster angle while varying sizes and layer thicknesses. The length-to-width ratio for all size effect specimens was kept constant at 2.225, with width varying in a ratio of 1:2:3:4. From SEL fracture parameter are derived for all specimens.

Furthermore, the study employs both experimental tests and numerical simulations to validate the application of size effect laws to investigate the fracturing

behavior of FDM specimens. Two types of specimens, Single Edge Notched Tension (SENT) and Double Edge Notched Tension (DENT), were assessed. The findings show that as the specimen size increases, the nominal strength decreases Finite Element (FE) simulations were conducted using Abaqus on DENT and SENT specimens, employing a calibrated Traction Separation Law (TSC) for crack propagation analysis. The Cohesive Zone Model (CZM) technique was utilized to model crack propagation, with parameters derived from the size effect analysis of CPLA parts. The FE results correlate well with the experimental results, confirming the acceptability of the CZM model derived from SEL.

Regarding PC parts, specimens with a raster angle greater than 45° exhibited quasi-brittle behavior, which shows the applicability of the size effect method. In this work, PC parts with different raster angles were fabricated using the FDM process. The results show that fracture energy decreases with increasing raster angle. Conversely, if PC parts contained even one layer with a raster angle as 0°, they exhibited ductile behavior, and the EWF approach was applied to derive fracture parameters.

Acknowledgment

It is a matter of immense pride and pleasure to express my sincere gratitude to my guide, **Dr. Chaitanya K. Desai**, Professor and Principal of C.K. Pithawala College of Engineering & Technology, for his encouragement and constant help throughout the research work, right from its inception. He has always provided me with moral support, wise advice, useful discussions, and comments.

I am glad to express my special thanks to both the Doctoral Progress Committee members appointed by GTU, **Dr. Harshit K. Dave** and **Dr. Piyush P. Gohil**, for sparing their valuable time and giving me the necessary guidance throughout my entire research work.

I also extend my thanks to the faculty members of the Mechanical Engineering Department, CKPCET, and the Computational Mechanics Group of CKPCET, Surat. I specially thank Ritesh M. Patel and all those who have spent their valuable time supporting me during the research work.

I would like to express my deep gratitude to Mantra Laboratory and Charusat Laboratory for providing me full support to carry out experimental work.

My heartfelt and utmost sense of gratitude goes to my parents for their patience and moral support, without which this research work would not have been possible. Words fail to express my appreciation for my wife, **Darshni**, whose unwavering love, patience, and sacrifices have been my pillar of strength. To my daughter, **Neer**, thank you for being the cherished ray of sunshine who made the difficult days brighter.

Last but not least, I am very thankful to all those who have helped me directly or indirectly in enabling me to continue this research work.

Patel Sumitkumar Yogeshbhai .

Contents

Nomenclature

FDM	Fused Deposition Modeling
SENT	Single Edge Notched Specimen
DENT	Double Edge Notched Specimen
EWF	Essential work of Fracture
CZM	Cohesive Zone Model
SEL	Size effect Law
FPZ	Fracture Process Zone
PLA	Poly-lactic Acid
CPLA	Carbon powder reinforced poly-lactic acid
TSC	Traction separation curve
PC	Poly-carbonate
FEM	Finite Element Method
P	Force in N
Δ	Displacement in mm
L	Gauge Length in mm
L_T	Total Length of Specimen in mm
D	Width of specimen in mm
a_0	Crack Length
t	Thickness of specimen in mm
K_i	Mode I stress intensity factor
σ_N	Nominal strength of specimen
α	Dimensionless crack length
E_1	Young's Modulus in 1-direction
G_{12}	Shear Modulus in 12-direction
ν_{12}	Poisson's ratio in 12-direction
ν_{21}	Poisson's ratio in 21-direction
E_2	Young's Modulus in 2-direction
$G(\alpha)$	Energy release rate
E^*	Effectiveness elastic modulus
$g(\alpha)$	Dimensionless energy release rate
G_f	Initial fracture energy of specimen
D_L	Ductility Level
t	Total thickness of specimen (mm)

h	Layer height (mm)
θ	Raster Angle
δ	Opening of Fracture process zone
G_f	Fracture energy in kJ/m^2
c_f	Effective length of fracture process zone
$g(\alpha)$	Dimension less energy release rate
r	Length of Fracture process zone
δ	Normal opening of Fracture process zone
l	Ligament length (mm)
W_f	Total work of fracture
w_e	Specific essential work of fracture
$w - p$	Specific non-essential work of fracture

List of Figures

List of Tables

List of Appendices

Chapter 1

Introduction

1.1 Origin of the work:

The structural integrity of engineering components can be compromised by a multitude of factors, ranging from unpredictable environmental conditions and loading uncertainties to design oversights, material imperfections, and construction or maintenance lapses. Catastrophic events are frequently precipitated by the presence of cracks, which may initiate either during the manufacturing process or under service loads. Such failures can have devastating consequences, particularly in critical sectors such as aerospace, automotive, and civil infrastructure, leading to substantial economic setbacks and, in tragic instances, the loss of human life.

Material imperfections are intrinsic and unavoidable, arising from a complex interplay of factors. When engineering structures contain cracks, the traditional principles of continuum mechanics become insufficient. Consequently, the last half-century has seen significant research dedicated to comprehending structural failures associated with cracking, leading to the development of various analytical approaches. This research is generally divided into two complementary fields: material science, which investigates the microscopic composition and crystallographic defects that govern crack nucleation and propagation; and fracture mechanics, which focuses on the macroscopic driving forces acting on a crack and quantifies the material's inherent resistance to fracture.

Consider the two solid bodies Ω_1 and Ω_2 separated by a common interface in the initial configuration as shown in Fig. 1.1. Ω_1 and Ω_2 could also be two regions of the same body connected by a thin (localised) zone of different nature (yield zone or craze). If a body fractures at an interface due to applied loads, new surfaces are formed. This creates a geometric discontinuity that prevents the unique mapping of points from the undeformed reference frame to the current configuration. The newly formed region cannot be uniquely mapped from the undeformed configuration. This is a fundamental problem in modeling fracture in the framework of the mechanics of continuous media. Fracture mechanics provides a necessary framework for analyzing

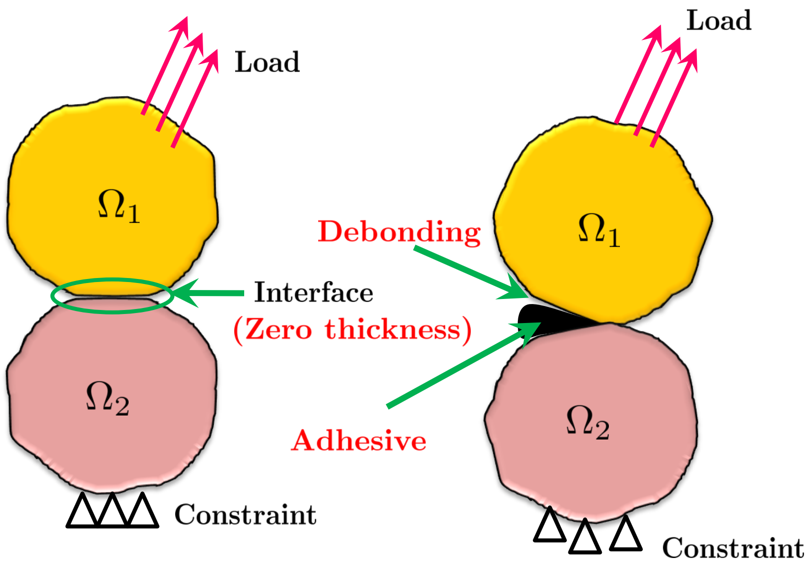

Figure 1.1: Schematic diagram of the interface and its debonding.

structural integrity in the presence of existing flaws, addressing the limitations of traditional elasticity and plasticity theories which cannot adequately model crack propagation. In contrast, damage models typically utilize porous plasticity formulations to simulate material degradation. These models quantify the reduction in load-bearing capacity caused by the nucleation, expansion, and merging of micro-voids under local stress states. Although the Cohesive Zone Model (CZM) describes material failure from a phenomenological perspective, it offers a distinct advantage over Linear Elastic Fracture Mechanics (LEFM): its parameters are intrinsic material properties and are independent of specimen geometry. CZM approach is easy to implement in finite element analysis (FEA) compared to the other two approaches. In this work, parameter for CZM model are derived by the size effect law (SEL) and essential work of fracture (EWF) method, The SEL is applicable to the quasi-brittle material and EWF is applicable to ductile material.

Additive Manufacturing (AM), frequently recognized as 3D printing, is a technique for rapidly developing products by adding layers one over another. This process was historically known as Rapid Prototyping (RP). The first RP technique was developed in the late 1980s, primarily for creating models and prototype parts. Due to the rapid construction time, it was initially used for visual modeling. However, this method is now recognized with high expectations to substitute traditional complex construction methods.

3D printing is an advanced AM technology that creates physical models from digital designs. High-quality prototypes, regardless of geometric intricacy, are effortlessly produced by this technology. In Computer-Aided Design (CAD) software, a 3D model is meshed and converted into a Standard Tessellation Language (STL) file. The 3D printing software processes this STL file, slicing the model into 2D layers [1]. The slicer generates a set of G-Code instructions that act as a blueprint for the printer. By following these commands, the machine deposits material in sequential cross-sections, which fuse to build the intended 3D shape. Modern developments have made 3D printers easy to operate and accessible at low costs. Most low-cost printers utilize Acrylonitrile Butadiene Styrene (ABS) or Polylactic Acid (PLA). Commercially available RP techniques include Stereolithography (SLA), Selective Laser Sintering (SLS), Laminated Object Manufacturing (LOM), Fused Deposition Modeling (FDM), Solid Ground Curing (SGC), and Ink Jet printing [2]. Among these, FDM is one of the most widely used techniques in the industry [3].

1.2 Fused Deposition Modeling (FDM)

In the 1990s, Stratasys Inc. introduced the FDM process for concept modeling [3]. Recognized for its ease of use in desktop applications, FDM prints components layer-by-layer, depositing material in a path similar to line drawing. Unlike techniques such as ink-jet printing or flexography, FDM is a viable alternative for adjusting to various textile substrates [4]. FDM has become a vital tool for producing fixtures and functional parts. As applications expand, FDM requires strict adherence to geometrical characterization specifications. FDM creates complex solid components by depositing layers bottom-up. Each layer must be deposited onto a solidified surface to prevent material deformation before hardening. Boundary conditions must be controlled, as the material cools rapidly. This technology allows for prototyping and manufacturing 3D geometries without tooling [3]. Figure 1.2 shows the schematic diagram of the FDM technique.

Initially developed for prototyping, this technology is now utilized for manufacturing tools and end-use parts. However, for serial production, components must meet specific mechanical requirements [2]. FDM forms material layer by layer in the X and Y directions via the precise movement of a liquefier nozzle. Upon layer completion, the platform moves in the Z-direction to introduce the subsequent layer. The filaments frequently utilized in the FDM process are ABS, PLA, various blends, and Polycarbonate (PC). The FDM technique deposits molten filament in a crisscross pattern, resulting in direction-dependent (anisotropic) properties [4]. A secondary nozzle often extrudes support material for features with overhangs less than 45°, preventing collapse. A vertical extruder melts thermoplastic onto the horizontal platform, where it solidifies. During this process, controlled relative motion occurs between the extruder and platform. After each layer, the platform moves vertically to facilitate bonding the next. Appropriate software creates precise extrusion trajectories. The layer by layer fabrication is described in Figure 1.2.

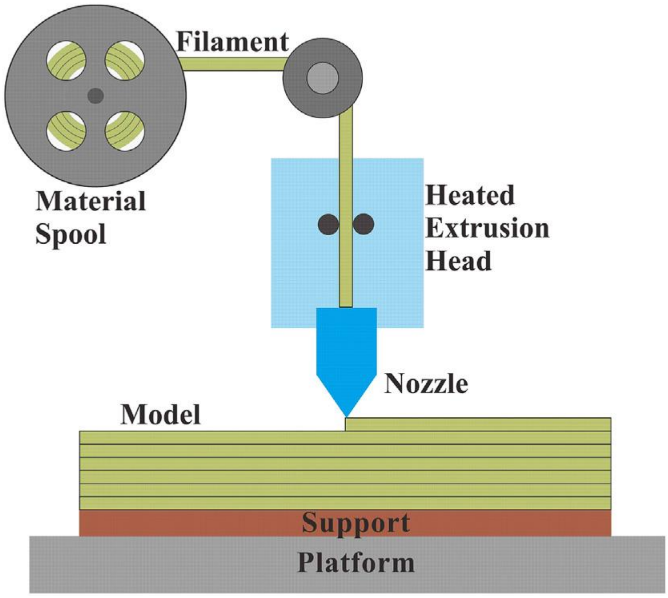

Figure 1.2: Schematic view of the model built layer by layer

Material properties are the most critical aspect of 3D printing. Numerous process parameters influence the distortion and meso structure configuration, directly affecting the printed material. Parameters such as layer thickness, air gap, filament color, and raster angle impact performance. These influences are typically evaluated using mechanical testing methods like compression, tension, and bending [5]. Mechanical strengths (tensile, compression, flexural) are highly anisotropic. Parameters including raster angle, width, air gap, and part orientation affect the strength, surface roughness, and geometric accuracy [4]. FDM parts generally exhibit strength two orders of magnitude lower than those produced by Selective Laser Sintering (SLS). While easier to fabricate, FDM thermoplastic parts typically possess lower stiffness and strength than SLS parts. Mechanical properties depend on the build direction due to the layered microstructure [6]. Raster fill is a critical tool for filling the part interior [7]. A key process parameter is the raster angle the direction of the nozzle path relative to the X axis which directly influences the part's mechanical properties and precision. While this angle can vary between 0° and 90°, a common strategy involves alternating the raster direction by 90 degrees between layers [6]. Stiffness and tensile strength increase with a negative air gap (overlap). Experimental results confirm that air gap and raster orientation affect tensile strength more significantly than processing temperature, raster width, or filament color [5].

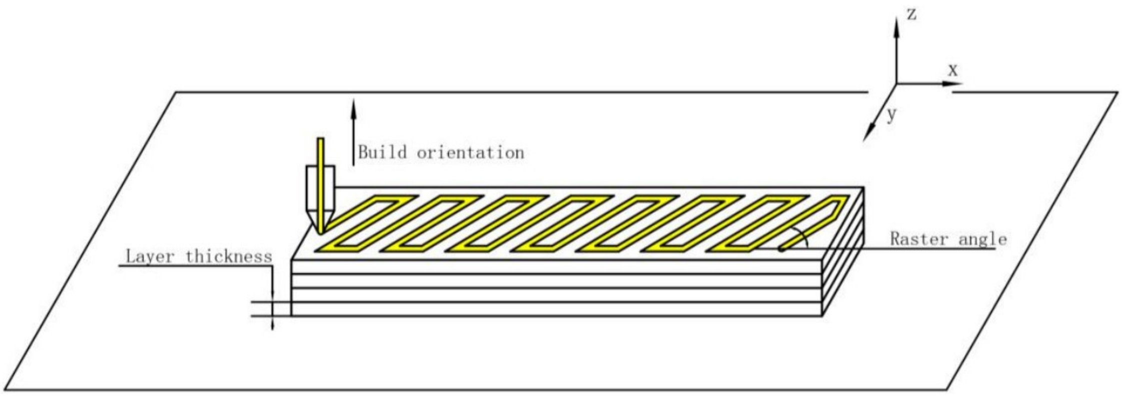

Figure 1.3: Schematic of layer thickness, raster angle, and build orientation in the 3D model

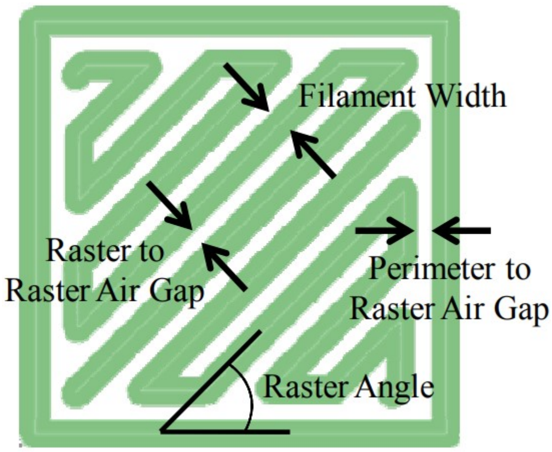

Figure 1.4: Schematic of Tool Path Parameters

End product mechanical properties are highly sensitive; minor parameter changes can significantly alter performance. Printed part properties are often lower than the bulk parent material. Layer thickness, the height of each deposited layer, is crucial. While thicker layers decrease accuracy and increase surface roughness, thinner layers improve accuracy but increase printing time. Layer thickness affects accuracy, nozzle diameter, and material properties [6]. Consequently, creating a new FDM part requires optimizing multiple parameters [7]. Components manufactured using 3D printing technology have various applications in automotive engineering [8], aerospace industries [9, 10, 11], medical fields [10, 12], and architecture. However, a primary challenge in applying such products is the variability of mechanical properties, which depend heavily on building parameters. Therefore, it is crucial to study these parameters and their individual effects on the strength of the end product.

1.3 Size Effect Law

The failure of any material can be analyzed through the relationship between stress and strain. This relationship is governed by various failure criteria. Basic failure criteria include maximum stress, maximum strain, deviatoric strain energy, and tensor polynomial criteria. However, as these are macro-mechanical approaches, they do not account for micro mechanical failures that predominantly occur near notches. When failure criteria involve energy, the analytical perspective shifts significantly. The most important consequence of this energy-based approach is the *size effect*.

According to classical theories of elastic and plastic materials, every structure made from the same material possesses a nominal strength that is independent of the structure's size. However, when analyzing geometrically similar structures, any deviation from this property is termed the size effect. The size effect is defined as the variation in nominal strength (σ_N) as the dimensions (typically width, D) of the structure vary.

The energetic size effect is caused by the release of fracture energy and becomes significant in the study of concrete, rock, ceramics, and other quasi-brittle materials. It has been observed that the size effect represents a transitional behavior between plasticity and Linear Elastic Fracture Mechanics (LEFM) where the size effect is most prominent as shown in Figure 1.5. This phenomenon is predominantly observed in tensile, torsional, and shear failures of quasi brittle materials.

For structures containing pre existing cracks or notches, the size effect is observed when geometrically similar notched specimens are considered. This energetic size effect can be explained by the nominal stress σ_N. According to Bažant [13], the Size Effect Law (SEL) is defined as:

$$\sigma_N = \sigma_0 \left(1 + \frac{D}{D_0}\right)^{-\frac{1}{2}} \tag{1.1}$$

Here, σ_0 and D_0 are empirical parameters dependent on the geometry of the structure. Equation (4.2) demonstrates that the nominal strength decreases as the structure size increases, as illustrated in Figure 1.5.

The parameters σ_0 and D_0 are defined as:

$$\sigma_0 = \frac{\sqrt{EG_f}}{c_f g'(\alpha)}; \quad D_0 = c_f \frac{g'(\alpha)}{g(\alpha_0)} \tag{1.2}$$

In these expressions, G_f stands for the fracture energy, c_f indicates the effective size of the fracture process zone, and $g(\alpha)$ refers to the normalized energy release rate. Fitting Equation (4.2) to σ_N data obtained from tests on geometrically similar notched specimens is the simplest method to determine the values of G_f and c_f.

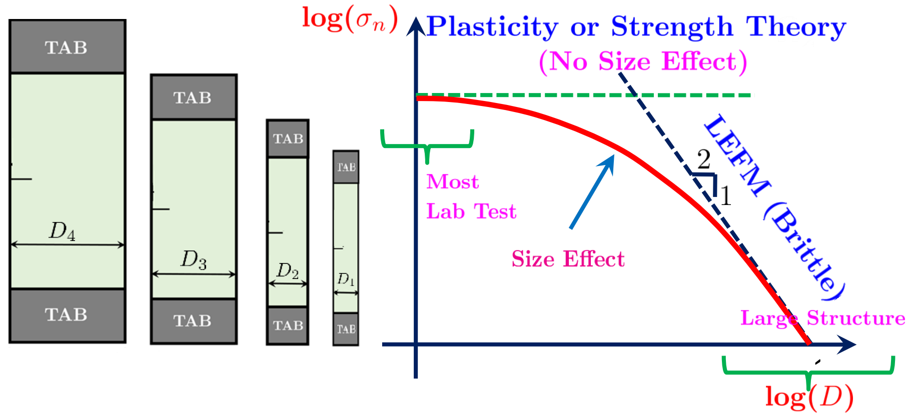

Figure 1.5: Size effect in notched specimen

FDM specimens will be manufactured for size effect testing in accordance with Bažant's methodology. If quasi-brittle behavior is observed, the Size Effect Law (SEL) will be applied to evaluate the various fracture parameters.

1.4 Structure of the thesis

The thesis is organized into 7 chapters, each of which is self contained.

Chapter 1 introduces the origin of the work and a review on the status of the research and development in the field of CZM. In this chapter FDM process also discussed.

Chapter 2 discussed the literature on different cohesive zone models, research developments in the FDM process, and literature of size effect.

Chapter 3 discusses the Objective of the present work.

Chapter 4 discusses the size effect analysis of FDM specimens fabricated from CPLA. Here, the complete procedure for the extraction of fracture parameters from SEL and the FE simulation of the specimens are discussed.

Chapter 5 discusses the size effect analysis of FDM specimens fabricated from PC. Here, for PC, various fracture parameters were derived from SEL.

Chapter 6 discusses the EWF method for FDM specimens fabricated from PC.

Chapter 7 discusses the conclusions and future scope.

Chapter 2

Literature Review

Extensive research has been conducted in the field of the CZM, resulting in a vast body of published literature. This chapter reviews the literature concerning various types of CZM and their implementation techniques. Additionally, studies regarding the FDM process including process parameters, specimen preparation, and testing protocols are discussed. Finally, the literature pertaining to the Size Effect Law (SEL) is reviewed, specifically focusing on various specimen geometries, size of specimens, and the criteria for applying SEL

2.1 Concept of Cohesive Zone Model

The CZM was originally introduced by Dugdale [14] and Barenblatt [15] (see Figure 2.1). In the analysis of material fracture, a Fracture Process Zone (FPZ) typically develops ahead of the crack tip. Within this zone, micro-cracks initiate, propagate, and eventually merge with the primary crack. The mechanical response within the FPZ is distinct from that of the surrounding bulk material, rendering conventional elastic-plastic constitutive relations which govern the bulk material unsuitable for this localized region of degradation.

In the CZM framework, the FPZ is conceptualized as a cohesive interface composed of two surfaces held together by cohesive tractions that separate during deformation. This approach aims to simulate the complex deformation mechanics within the FPZ using a simplified cohesive interface model. The relationship between the cohesive traction and the separation (displacement jump) of these surfaces is defined by the Traction Separation curve (TSC). Unlike standard continuum mechanics, which assumes continuity, CZM explicitly permits a displacement jump within the medium, effectively decoupling the material behavior into two components: bulk deformation and interfacial separation. The bulk deformation is handled by conventional continuum models, while the separation is governed by the TSL (see

Fig. 2.2).

The CZM methodology offers several distinct advantages: (1) it eliminates the requirement to assume fully bonded or pre cracked interfaces; (2) it is applicable even when the non linear zone size is significant relative to the cracked geometry; and (3) it can be readily integrated into finite element (FE) codes.

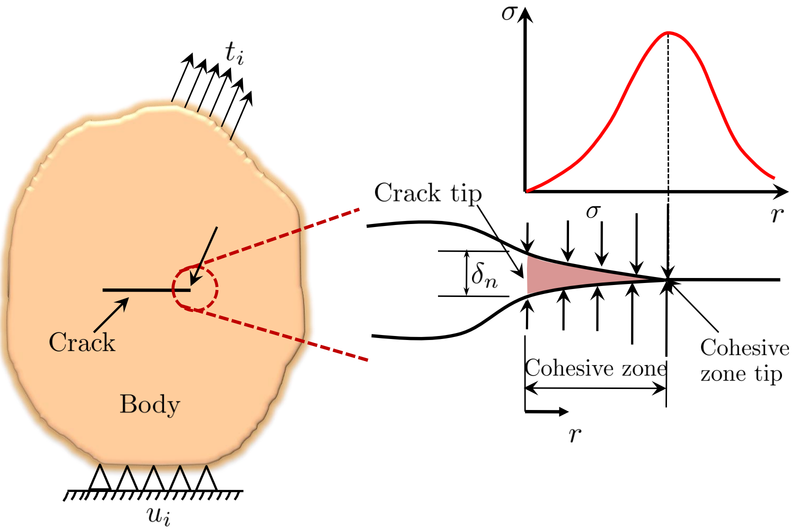

Figure 2.1: Concept of the CZM.

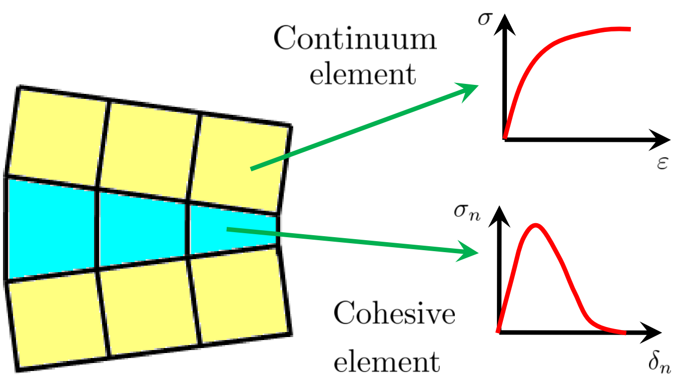

Figure 2.2: CZM modeling strategy.

Implementing a basic CZM requires two primary parameters: fracture toughness and either the cohesive strength or the critical separation value. Fracture toughness is typically determined via laboratory testing of the specific material system. This experimental value is then utilized in conjunction with Finite Element (FE) analysis to determine the cohesive strength through an inverse approach. In this framework, crack propagation initiates when the crack tip displacement reaches a critical threshold and sufficient energy is available from the system to generate new fracture surfaces. As with any constitutive model, the specific TSc parameters must be derived experimentally, though isolating these parameters through testing remains a challenging endeavor.

Dugdale [14] formulated a microscopic plasticity model for ductile materials, commonly referred to as the **strip yield model**. Independently, Barenblatt [15] proposed a comparable model for brittle materials, accounting for molecular cohesion. These formulations, collectively known as the Dugdale Barenblatt (D-B) models, resolve the issue of physically non existent stress singularities in cracked bodies and have been widely adopted across various fracture mechanics applications.

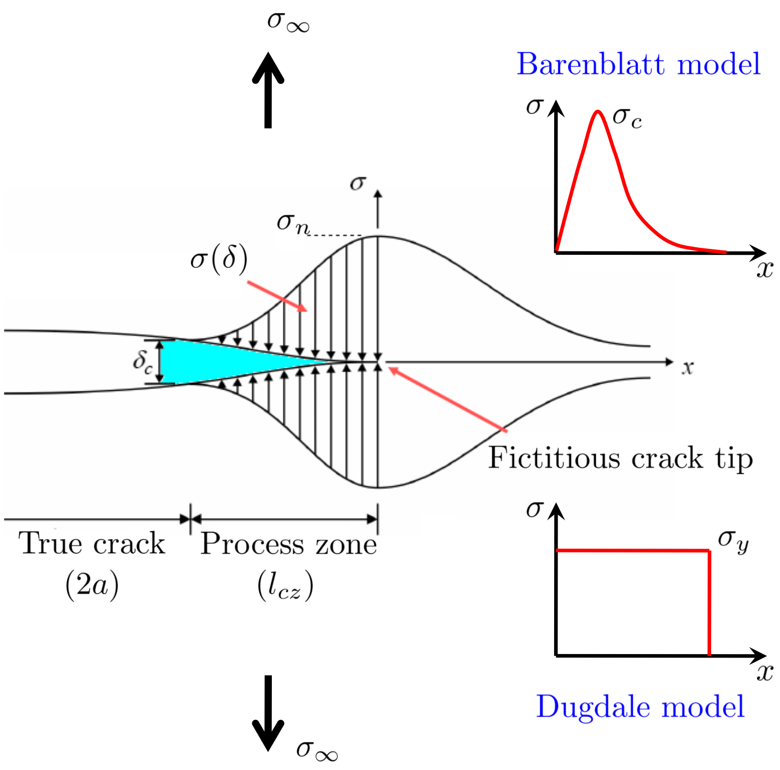

Figure 2.3: Dugdale-Barenblatt model (D-B model).

2.1.1 Crack Tip Process Zone

Figure 2.4(a) provides a magnified view of the crack tip process zone. This region lies between the separating surfaces where non zero tractions exist, governed by the TSC. It is important to note that the TSC does not account for plastic zone effects (energy dissipation) occurring outside the cohesive zone boundaries.

Typically, a TSC demonstrates an increase in traction as separation grows, peaking at a maximum value before declining to zero, which indicates complete material separation (see Fig. 2.4(b)). The total energy release rate (ERR) is represented by the area under the TSC curve. Various cohesive law shapes have been postulated and tested within the CZM framework.

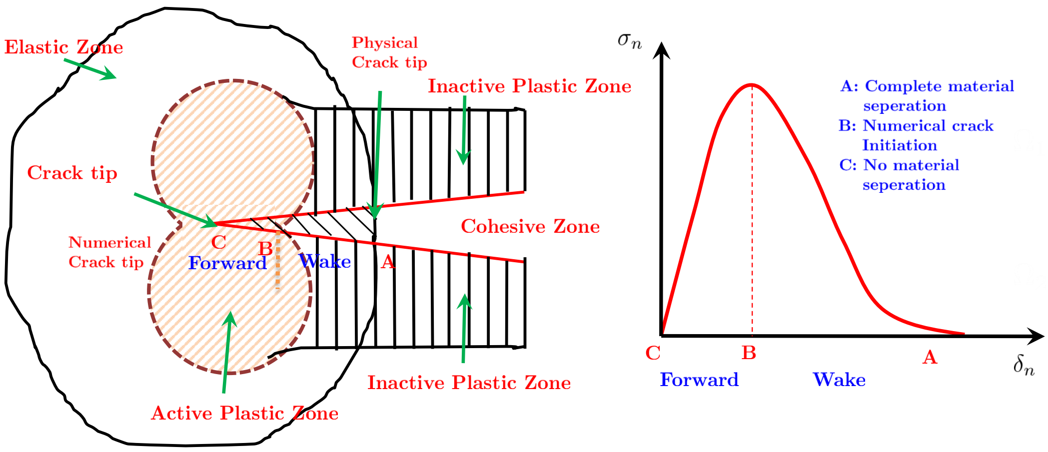

Figure 2.4: (a) Cohesive zone, and (b) typical TSC of CZM.

Li and Chandra [16] proposed a micromechanical perspective on CZM, suggesting that an intrinsic CZM is comprised of four distinct stages (Fig. 2.5(a)) based on physical assumptions for numerical simulation. In first stage, Characterized by general elastic behavior with no separation. In stage II, Marks the initiation of a crack once a specific criterion, such as critical hoop stress or strain energy density, is satisfied. Stage III, Involves damage evolution governed by a non linear cohesive law (softening curve), relating stress to crack opening width. As the cohesive law defines the FPZ characteristics, the specific shape of this softening curve is critical. Stage IV, Represents complete failure, occurring when the crack opening width reaches its critical limit. In this stage, traction drops to zero, representing newly generated surfaces.

Figure 2.5(b) illustrates the distinction between extrinsic and intrinsic energy dissipation zones.

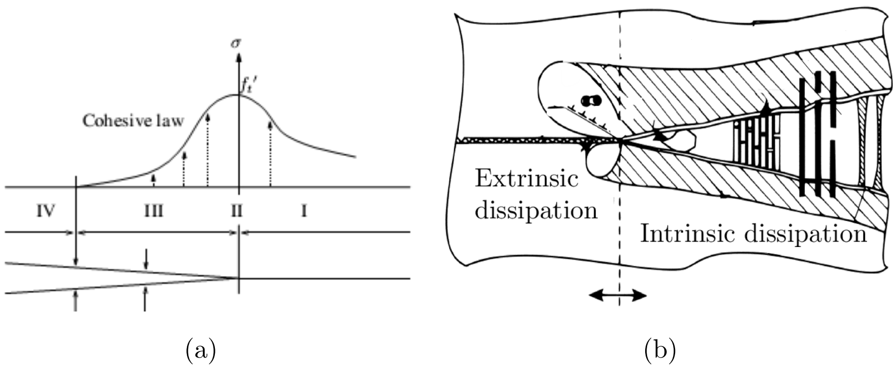

Figure 2.5: Schematic of Cohesive Concept.

2.1.2 Features of the Cohesive Law

Developing a cohesive law generally follows one of two approaches: direct experimental measurement or a phenomenological method using predefined functional assumptions and estimated parameters. Due to the lack of effective experimental methods for directly measuring the traction separation relation, direct experimental determination is rare [17]. Consequently, the prevailing approach involves assuming a specific traction separation shape and treating cohesive parameters as calibration constants, determined by fitting CZM simulation outputs to experimental datasets. The defining features of any CZM are the shape of the traction separation curve and the magnitude of the cohesive parameters.

Numerous cohesive model variations have been widely applied to predict fracture behavior. Needleman [18] introduced a polynomial law to describe void nucleation in metal matrices. Influenced by atomistic calculations of interfacial separation [19, 20], [21] later adopted an exponential form. Needleman [18] expanded the use of exponential models to investigate void nucleation at particle matrix interfaces, rapid crack growth in brittle materials under dynamic loads, and dynamic crack propagation along bimaterial interfaces. Tvergaard and Hutchinson [22] utilized a trapezoidal model to assess crack growth resistance in elasto plastic materials, while Suresh [23] applied a linear cohesive law to intergranular fracture, where traction rises linearly to a critical opening before dropping to zero. Additionally, Camacho and Ortiz [24] implemented a linearly decreasing cohesive model to simulate multiple crack propagation paths during impact damage in brittle solids. Modern CZM applications predominantly utilize exponential, bilinear, polynomial, or trapezoidal TSC forms. Representative shapes are shown in Fig. 2.6.

Despite the variety of cohesive laws, they share a fundamental characteristic: cohesive traction increases with separation up to a peak value, followed by a decline toward zero as separation continues. While the initial rising section is sometimes omitted in extrinsic approaches, the softening trend representing material degradation is universal. This response arises from microstructural mechanisms such as atomic interaction, void nucleation, and coalescence. The defining attributes of a CZM include the peak traction (cohesive strength), the total work of separation (calculated as the area under the traction separation curve), and the separation distance at which damage initiation occurs (characteristic length) It is widely recognized that these parameters are not intrinsic material constants but are dependent on the specific modeling context. In purely elastic analyses (e.g., brittle fracture), external work is partitioned between recoverable elastic strain energy and non recoverable cohesive energy. In elastic-plastic analyses, work is dissipated as inelastic strain energy in addition to the cohesive energy. For small scale yielding, cohesive

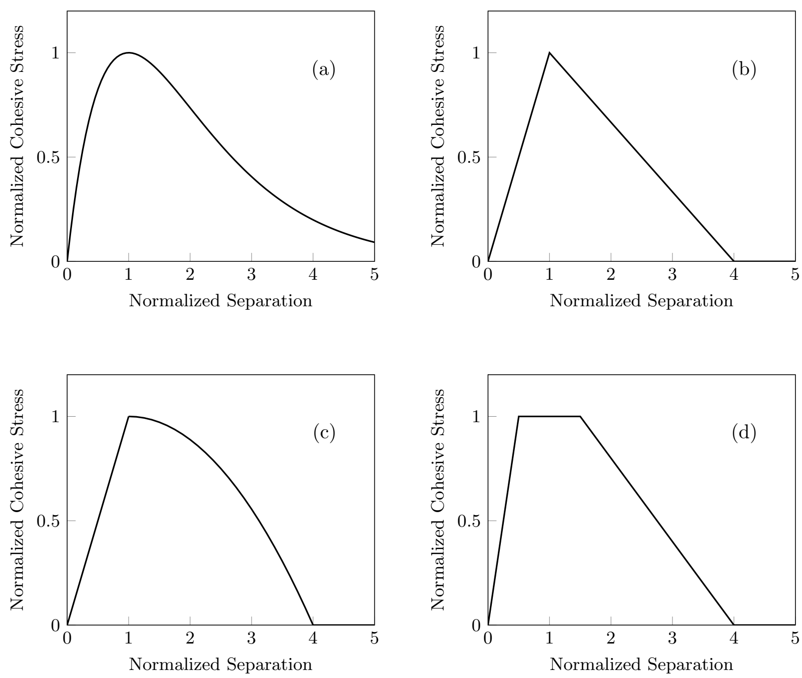

Figure 2.6: Different forms of TSC. (a) Exponential, (b) Bilinear, (c) Polynomial, (d) Trapezoidal.

energy aggregates all dissipative processes within the FPZ (bridging, cavitation, etc.), excluding inelastic strain. However, Tvergaard et al.[22] noted that if cohesive strength is high relative to yield stress, the cohesive zone may induce secondary energy absorbing processes, such as plastic dissipation. Researchers have extensively investigated distinct CZM formulations, including polynomial, exponential, and tabular models, effectively applying them to predict fracture behavior [25, 23]

Desai [26] demonstrated the determination of the numerical cohesive zone length for adhesive joints using DCB specimens in Abaqus. Figure 2.7 illustrates this development using a mode-I DCB specimen under linearly increasing Δ.

When displacement begins, the element at the crack tip attains its ultimate strength and immediately starts to soften. Continued displacement causes adjacent elements to yield, thereby defining the process zone length, l_{cz}. Within this zone, the stress profile builds up to the maximum interfacial strength ahead of the physical crack tip. This length reaches a maximum, l_{czf}, when the crack tip element fails completely, marking the onset of propagation.

It is crucial to distinguish between the *true physical cohesive zone length* (where irreversible damage occurs) and the *numerical cohesive zone length* (where elements are on the softening path). For accurate numerical representation, the TSL shape should ideally reflect the stress distribution of the physical damage mechanisms.

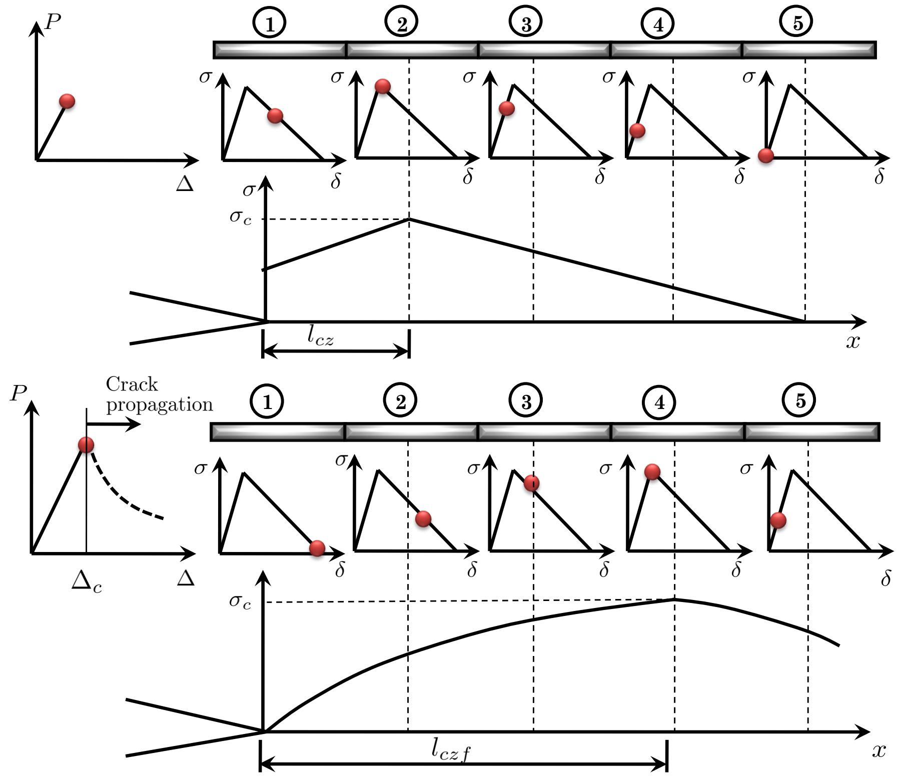

Figure 2.7: Development of the numerical cohesive zone.

However, measuring this distribution is experimentally difficult. Fortunately, for global load-displacement analysis, results are relatively insensitive to the exact TSC shape, provided the correct interfacial strength and fracture toughness are maintained. This robustness explains the popularity of the geometrically simple bilinear TSC. Furthermore, once a crack initiates, results become less sensitive to interfacial strength, with fracture toughness becoming the dominant parameter.

Desai et al. ([27] utilized CZM to simulate failure in adhesive joints, employing two distinct approaches to measure the TSC for an adherend/adhesive system exhibiting interfacial failure.

- **Method 1 (Differentiation):** The TSC is derived by differentiating the experimentally measured J-integral with respect to opening displacement.

- **Method 2 (Inverse FE):** An inverse Finite Element analysis is performed where the adhesive layer and cohesive elements are modeled. The TSC is determined iteratively by matching numerical load-displacement data with experimental results (see Figure 2.8).

Martinez AB et al. [28] introduced an alternative criterion for characterizing fracture behavior by defining a parameter known as the Ductility Level (D_L). Their

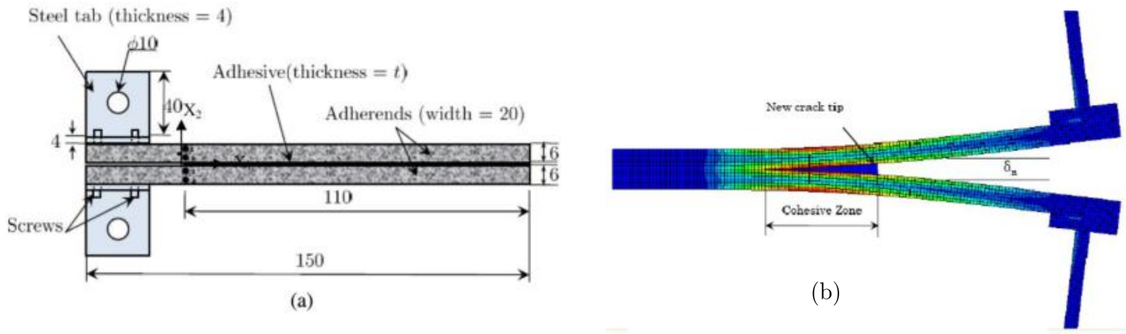

Figure 2.8: (a) Schematic of DCB Specimen (b) FE Deformed configuration of DCB Specimen [[27]]

study focused on accurately identifying the lower ligament threshold that demarcates the transition from a mixed mode stress state to a plane stress state. For pre cracked specimens, they formulated the ductility level as the ratio of displacement at rupture (d_r) to the initial ligament length (l), expressed as $D_L = d_r/l$. A clear correlation was established between the average ductility level and the specific fracture mode. Based on their classification,Figure 2.9 (a) Brittle ($D_L < 0.1$); (b) Ductile instability ($0.1 < D_L < 0.15$); (c) Blunting ($1 < D_L < 1.5$); (d) Necking ($1.5 < D_L$); (e) Post-yielding ($0.15 < D_L < 1$). A D_L falling within the range of 0.15 to 1.5 signifies a ductile fracture mechanism.

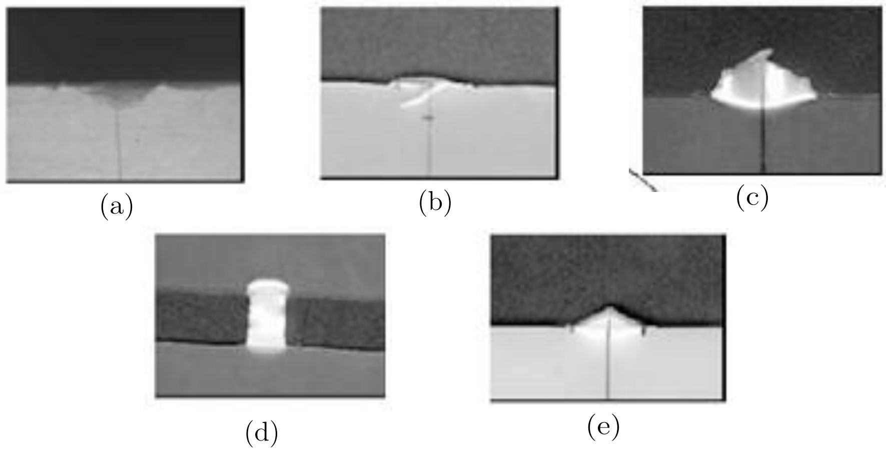

Figure 2.9: Classification of fracture types by Ductility Level (D_L):

Their study concluded that the differentiation approach yielded TSCs dependent on adhesive thickness and loading rate. In contrast, the inverse approach produced a TSC independent of these variables. Consequently, the TSC derived via the inverse method is considered intrinsic to the adhesive/adherend pair and, in that context, unique.

2.2 Research and Development in the FDM Process

Extensive research has been conducted to determine how various process parameters such as layer thickness, raster angle, and printing speed influence the mechanical properties of 3D printed materials. Additive manufacturing, specifically 3D printing, has found widespread application across diverse sectors, including automotive engineering [8], aerospace [9, 10], medical fields [10, 12], and architecture. While several techniques exist, such as Stereolithography (SLA), Selective Laser Sintering (SLS), Laminated Object Manufacturing (LOM), and Solid Ground Curing (SGC) [2], Fused Deposition Modeling (FDM) remains one of the most prevalent industrial techniques [3].

In the FDM process, components are fabricated by depositing material layer by layer. Filament is supplied to a heated nozzle, melted, and subsequently extruded atop the previously printed structure. The nozzle traverses two mutually perpendicular directions to build a layer before indexing up in the Z direction. Common materials include thermoplastics like PLA, ABS, Nylon, Carbon-PLA, and Polycarbonate. However, this layer by layer deposition results in direction dependent, or anisotropic, material properties [4]. Consequently, the mechanical performance is heavily governed by printing parameters such as raster angle, layer height, filament width, and flow percentage.

The orientation of the polymer beads, in particular, significantly dictates strength. Ahn et al. [29] investigated the effects of air gap, raster orientation, temperature, and color on the tensile strength of FDM parts. They concluded that while temperature and color have minimal impact, air gap and raster orientation are critical. They recommended using a negative air gap to enhance strength and stiffness. Similarly, Es-Said et al. [30] studied layer orientation effects on tensile, bending, and impact strength. Their findings indicated that the 0° raster angle yielded the highest tensile and impact strengths, outperforming other orientations significantly. Zhao et al. [31] and Yao et al. [32] further developed theoretical models to calculate Ultimate Tensile Strength (UTS) and Young's modulus for various raster angles, validating experimentally that these properties improve as layer thickness decreases.

In terms of material behavior, Wu et al. [33] conducted a comparative study using ABS and Polyether-ether-ketone (PEEK). They observed that the tensile properties of FDM parts are generally inferior to those manufactured via injection molding. Specifically, they noted a non-linear relationship with layer thickness: tensile properties improved when thickness increased from 200 μm to 300 μm but degraded significantly at 400 μm.

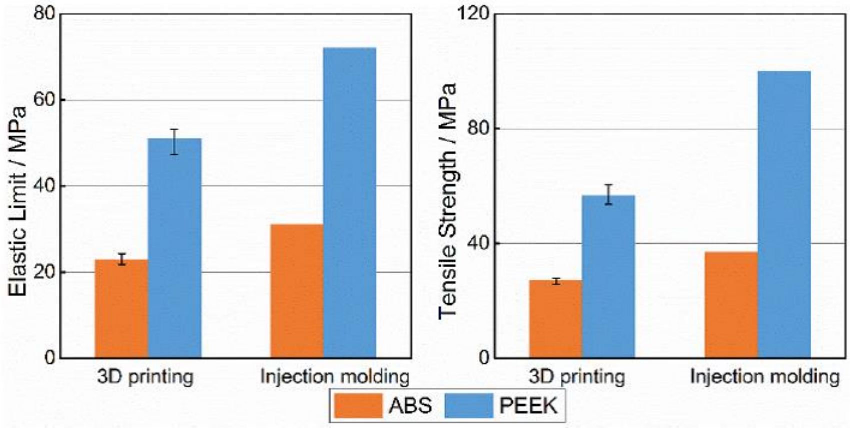

Figure 2.10: Comparison on tensile property between acrylonitrile butadiene styrene (ABS) and polyether-ether-ketone (PEEK) [33].

Furthermore, Tymrak et al. [34] evaluated the viability of low cost, open source RepRap printers against commercial systems. Their study on elastic modulus and tensile strength concluded that open source printers, when properly tuned, are mechanically functional for tensile applications.

Testing standards and specimen geometry also play a vital role in characterizing these materials. Laureto and Pearce [35] highlighted the anisotropic mechanical differences between ASTM D638 Type I and Type V specimens using FFF printed PLA (see Figure 2.11). They prepared 405 specimens varying layer height, temperature, speed, and flow percentage.

Figure 2.11: Tensile Specimens of ASTM D638-14 Type I vs. Type IV.

Their results demonstrated that horizontally printed Type IV specimens exhibited 4.4% to 17.0% higher maximum tensile strength compared to Type I. Furthermore, orientation proved critical; horizontally oriented Type IV specimens showed a UTS 47.9% greater than their vertically printed counterparts (see Figure 2.12).

Given the layered nature of FDM parts, researchers have applied composite

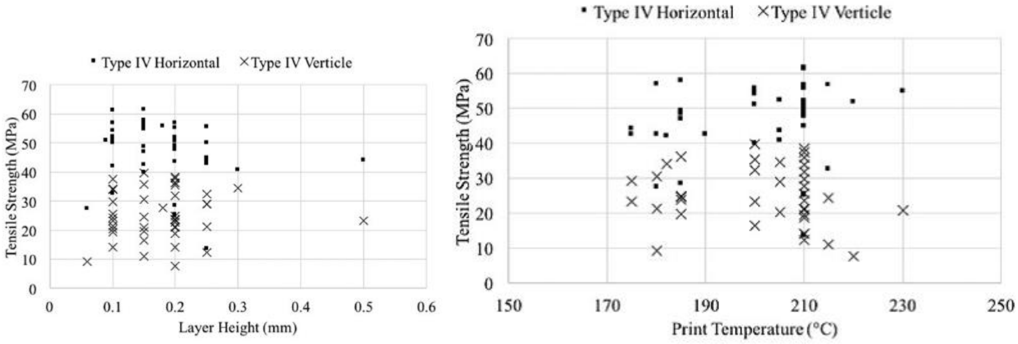

Figure 2.12: UTS (MPa) distribution Vs Layer Height and Print Temperature for Type IV Horizontal and Type IV Vertical specimen.

material theories to predict performance. Casavola et al. [36] characterized the behavior of FDM parts using Classical Laminate Theory (CLT). By testing single layer specimens at 0° and 90° (Figure 2.13) and measuring Poisson's ratio via strain gauges, they found that CLT is capable of predicting the mechanical properties of FDM parts.

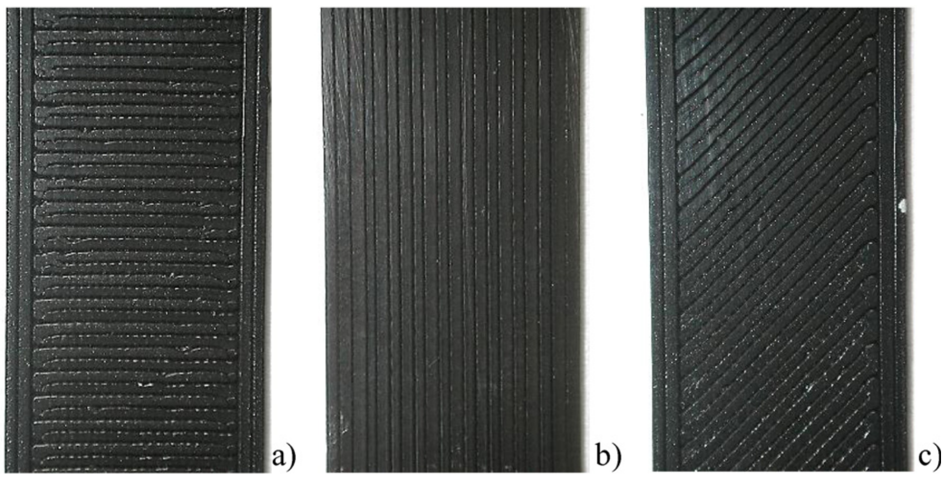

Figure 2.13: Single Layer Microscopic view of the specimens: a) raster angle 90°; b) raster angle 0°; c) raster angle 45° [36].

Their experiments revealed that increasing the raster angle from 0° to 90° reduced Young's modulus by 35.72% for ABS and 11.12% for PLA. They concluded that ABS exhibits more pronounced orthotropic behavior than PLA. Additionally, Durgun and Ertan [37] investigated the trade off between mechanical properties and production cost (surface roughness and support material), analyzing roughness along parallel and perpendicular directions (Figure 2.14).

Ahn et al. [29] established that FDM components exhibit orthotropic behavior, implying that their mechanical performance is inherently dependent on the

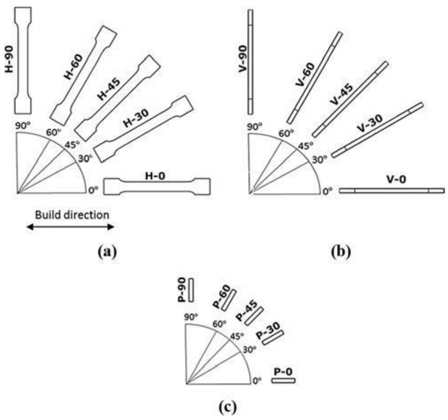

Figure 2.14: Schematic view of the raster angles for (a) horizontal, (b) vertical and (c) perpendicular part positioning.

direction of raster orientation. Additionally, Al Abadi et al.[38] assessed the performance of reinforced FDM parts, concluding that both raster orientation and the presence of reinforcement significantly dictate the tensile strength of printed composite components. Song et al. [39] characterized unidirectional FDM 3D printed PLA, revealing an orthotropic elasto-plastic response marked by significant tension compression asymmetry. Notably, they found that 3D-printed specimens exhibited superior toughness compared to homogeneous injection molded PLA, particularly when loaded in the extrusion direction. Kozior et al. [40] presented experimental results demonstrating the effect of build orientation and platform positioning on the compressive properties and stress relaxation of ABS components produced via FDM. Due to this orthotropic nature, fracture behavior plays a critical role in structural integrity. During fracture, a large non-linear Fracture Process Zone (FPZ) develops where micro cracks initiate, grow, and coalesce [41, 42]. The strength and stability of components can be accurately predicted if the size of the FPZ is known. One effective approach to predicting the geometrical parameters of the FPZ is the Size Effect Law proposed by Bazantet al. [43]. This law, based on fracture energy release, is particularly relevant for quasi brittle materials. Bazantet al. [43] further proposed a methodology for extracting FPZ parameters using the R-curve concept (Crack Resistance curve).

2.3 Review of Size Effect Law (SEL)

Given the expanding applications of additive manufacturing, understanding the failure mechanisms of 3D printed materials is paramount for safety and structural integrity. Traditionally, the failure of composite materials has been characterized by stress and strain based criteria, such as maximum stress, maximum strain, deviatoric strain energy, and tensor polynomial criteria. However, when failure criteria incorporate energy release, a critical phenomenon known as the *size effect* emerges.

According to classical elastic or plastic theories, the nominal strength (σ_n) of a structure made from a specific material should remain constant regardless of the structure's size (D), provided the structures are geometrically similar. Any deviation from this size independence is defined as the size effect.

Bazant [13] originally established the concept of the size effect through extensive research on concrete, rock, and metals. He observed that fracture in quasi brittle materials (like concrete and rock) is characterized by a fracture process zone (FPZ) of micro cracking, whereas ductile metals exhibit a yielding zone. This FPZ causes significant deviations from Linear Elastic Fracture Mechanics (LEFM). Experimental results demonstrated that for rock and concrete, the strength of larger structures is noticeably lower than that of geometrically similar smaller structures, a behavior that classical LEFM cannot fully predict.

Bazant et al. [44] extended this research to composite materials, measuring the size effect on notched specimens of graphite/epoxy cross ply and quasi isotropic laminates. The experimental setup involved rectangular specimens with widths of 6.4, 12.7, 25.4, and 50.8 mm, maintaining geometric similarity in the remaining dimensions (see Figure 2.15).

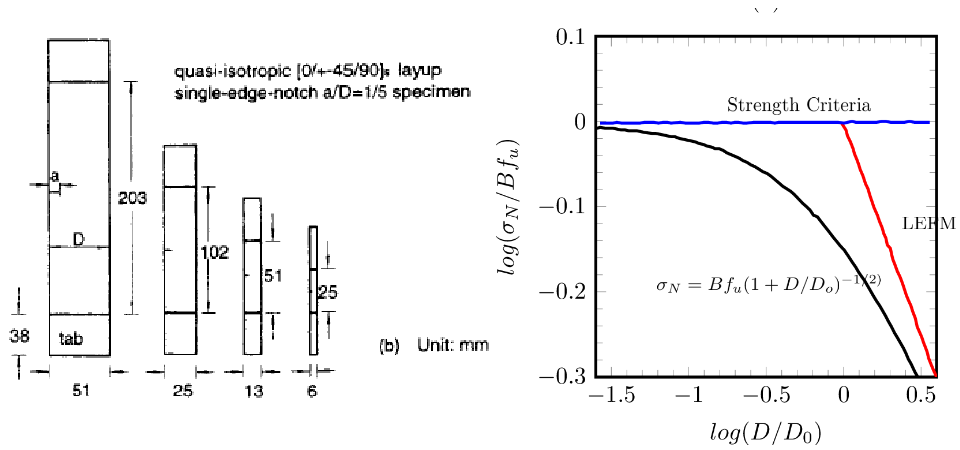

Figure 2.15: Schematic view of Specimen Size and Size Effect Law

The gauge lengths were scaled to 25, 51, 102, and 203 mm respectively. To test fracture behavior, Double Edge Notched Tension (DENT) geometry with a crack length $a = D/16$ was applied to cross ply specimens, while Single Edge Notched Tension (SENT) geometry with $a = D/5$ was machined into quasi isotropic specimens. The results confirmed a strong correlation between structural size and the strength of the composite material, showing close agreement with Bažant's theoretical derivation:

$$\sigma_N = Bf_u(1+\beta)^{\frac{-1}{2}}, \qquad \beta = \frac{D}{D_0} \tag{2.1}$$

where β represents the relative structure size, σ_N is the nominal strength (P_{max}/bD), and D_0 is a reference size. By curve fitting experimental data to this equation, the size effect law for composite materials was validated.

Furthering this domain, Salviato et al. [45] emphasized that the scaling of mechanical properties is essential for the design of large scale composite structures. Their study utilized geometrically similar SENT specimens fabricated from 0° epoxy/carbon twill 2×2 laminates. They tested specimens of three different sizes (scaled 1:2:4), all equipped with 38 mm glass/epoxy tabs for gripping (Figure 2.16).

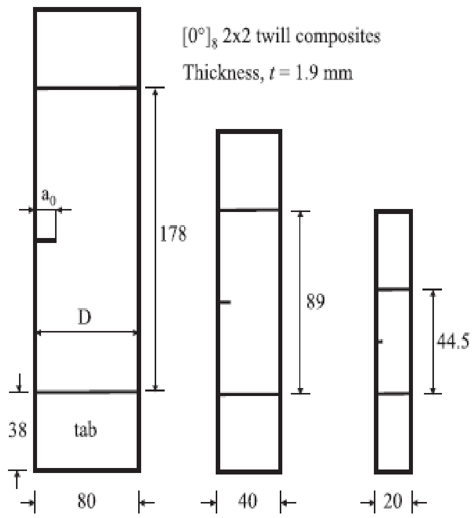

Figure 2.16: Schematic view of Specimen Size

Their findings corroborated that nominal strength decreases as specimen size increases. The data showed excellent alignment with Bažant's Size Effect Law (SEL), allowing for the accurate measurement of the material's inter laminar fracture energy (G_f).

Chen et al. [46] performed a comprehensive analysis of the size effect in open hole tensile composites. They evaluated three distinct models: the Classical Laminate Theory (CLT) model, the Continuum Shell Layered Interface (CSLI) model, and the Continuum Shell Ply Block (CSPB) model. Their analysis concluded that while the CLT model is sufficient for laminates failing in a purely brittle manner, the CSLI model is necessary for accurately predicting fracture properties when delamination is present.

Given their orthotropic mechanical characteristics, FDM components are increasingly utilized in the fabrication of large scale structures. However, during failure, these materials exhibit a distinct non linear Fracture Process Zone (FPZ) [41, 42]. A comprehensive analysis of this FPZ is essential for accurately evaluating the structural strength and stability of such components. While extensive studies have characterized the general mechanical behavior and parameter sensitivity of FDM parts [47, 48, 49, 50, 51], the accurate extraction of specific fracture properties remains a relatively unexplored area. The present study addresses this gap by focusing on the detailed evaluation of these fracture parameters. Therefore,the current study aims to investigate the fracture properties and SEL of FDM parts with varying thickness, following the approach by Bazant et al[43].

2.4 Research Gap

1. The CZM concept is widely used for crack propagation analysis in various material systems subjected to different loadings. However, for the effective use of CZM, its parameters such as maximum traction, critical separation, cohesive energy, and, most importantly, its shape need to be calibrated experimentally.

2. Work reported in the literature is primarily related to finding the plane stress fracture toughness of materials. The extraction of CZM parameters from experiments is not an easy task.

3. Existing literature extensively covers the effect of various FDM parameters on general mechanical properties. However, the determination of fracture parameters and the numerical simulation of FDM specimens remain areas with scope for further research.

4. The SEL is commonly used to analyze scaling effects in quasi brittle materials. However, deriving and applying the Size Effect Law specifically for FDM printed quasi brittle materials is an area that still offers scope for research.

5. For FDM specimens, extracting various cohesive zone and fracture parameters from Size Effect Law experiments is a challenging task that remains a key scope for research.

6. Various parameters, such as layer height, raster angle, and infill pattern, influence the mechanical performance of FDM manufactured specimens. Consequently, investigating the specific impact of these parameters on fracture strength also offers scope for research.

7. Following the derivation of parameters, the implementation of CZM in Finite Element (FE) analysis for FDM specimens remains an area for research.

8. If FDM specimens exhibit ductile behavior, methods such as the Essential Work of Fracture (EWF) approach are suitable for characterizing fracture toughness under plane stress conditions.

Chapter 3

Objective of work

- To fabricate specimens with various geometries, sizes, raster angles, and thicknesses using the FDM process.
- To investigate the size dependence of the FDM specimens, assessing whether it exhibits behavior characteristic of composite materials.
- To characterize the size effect phenomenon in the the FDM specimens, specifically testing for quasi-brittle behavior. and to derive size effect parameter of FDM specimens
- To apply the SEL in order to extract the fracture parameters G_f and c_f for components fabricated with diverse thicknesses and raster orientations
- To extract CZM parameters for FDM-manufactured specimens using the SEL.
- To validate the efficacy of the experimentally measured CZM parameters through Finite Element Method (FEM) simulations by comparing local and global mechanical responses.
- To evaluate the fracture energy using the Essential Work of Fracture (EWF) method, should the FDM specimens exhibit ductile behavior rather than quasi-brittle characteristics.
- To analyze the influence of various governing factors such as specimen geometry, material type, specimen thickness, and raster orientation on the parameters of CZM and SEL.

Chapter 4

Size Effect Analysis of FDM Specimens Fabricated from CPLA

In this chapter, the size effect analysis of specimens manufactured from Carbon-PLA (CPLA) using the FDM process is discussed. The experimental phase involved the fabrication of tensile dogbone specimens to determine elastic properties, followed by the preparation of scaled notched specimens for size effect testing. Fracture tests were carried out to obtain the necessary load-displacement data. Using Bažant's [43] SEL as the theoretical basis, the experimental data were analyzed to extract the specific fracture energy (G_f) and the length of the fracture process zone (c_f). Additionally, a Traction Separation Curve (TSC) was derived to characterize the softening behavior of the material. To ensure the efficacy of these experimentally derived parameters, a Finite Element (FE) analysis was performed, verifying the consistency between the numerical simulations and the physical test results.

4.1 Materials and Methods

The 3D modeling of the specimens was carried out using Autodesk Inventor. Subsequently, the resulting STL files were imported into Simplify3D slicing software to generate the G code. Specimens were manufactured using a Zonestar FDM printer equipped with a 0.4 mm nozzle and a build volume of 200 × 200 × 200 mm. The filament material was carbon powder reinforced polylactic acid (CPLA), made of 20% carbon powder reinforced with polylactic acid, was used to manufacture parts through FDM process. For the printing process, the bed temperature was maintained at 60°C, while the nozzle temperature was fixed at 220°C. The air gap defined as the distance between two successive beads in the same layer was set to 0 mm to maximize density. Two contour lines (perimeters) were printed before filling the interior. The layer thickness (h), representing the height of the deposited filament, varied according to specific specimen requirements. Beads were deposited at specific orientations, referred to as the raster angle (e.g., a 0° raster angle indicates beads deposited parallel to the loading direction). All specimens were sliced using Simplify3D software with a rectilinear pattern and 100% fill density. To find mechanical properties, The geometry of the CPLA specimens followed the ASTM D638-14 standard [52] for tensile testing, as illustrated in Figure 4.1. The shape of the specimens with details are as shown in the figure 4.1. Figure 4.1 illustrates the FDM layer build direction and the corresponding dimensions with all details of The solid model of the specimens are created using Autodesk Inventor which is further sliced using Simplify3D to generate G code file. Subsequently, the generated G code was given to the FDM unit to initiate fabrication. As illustrated in Figure 4.2, the printing setup involves feeding the CPLA filament into a heated liquefier, where it is melted and extruded through a 0.4 mm nozzle onto the build platform. Figure 4.2 shows the FDM printer and its components: the filament tube, extruder, heated liquefier, and print bed. The Dogbone specimens were manufactured using the FDM process with a thickness (t) of 1.4 mm.

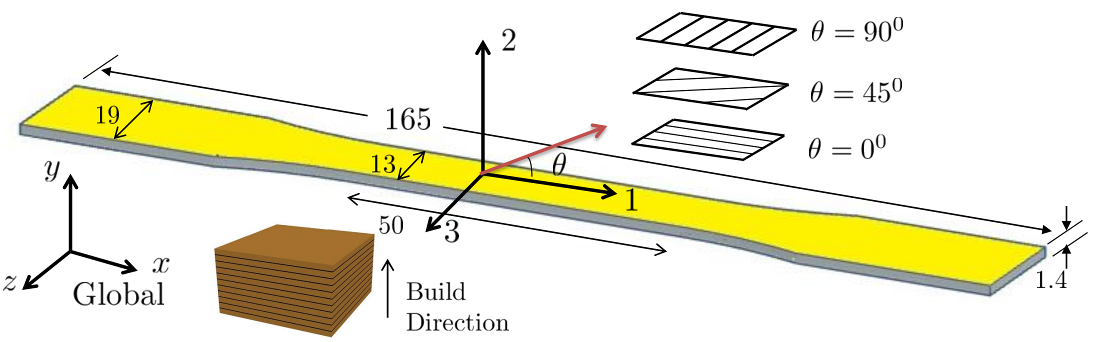

Figure 4.1: ASTM D638 dogbone shaped test specimen with Details.

Specimens were manufactured using a design comprising three raster angles ($\theta = 0°, 45°, 90°$) and three layer heights ($h = 0.12, 0.23, 0.35$ mm). For every unique parameter combination, five specimens were prepared, all with a uniform thickness (t) of 1.4 mm. specimens for each direction and each layer thickness have been made for the experimental measure of the elastic modulus (E) of the CPLA material in the longitudinal and transverse direction with raster angle 0°, 45° and 90 ° is made. 0° raster angle specimens are for longitudinal direction(E_1), 45° raster angle specimens are for direction(E_{45}) and 90° raster angle specimens are for transverse direction(E_2). The experiments(i.e Tensile test) had been conducted on an Instron Universal testing machine (UTM) with a load cell of 5000 N and a crosshead speed(Load Rate) of 5 mm/min. Figure4.3 shows the UTM with grip section and load cell.

Figure 4.4a illustrates the fractured CPLA dogbone specimens tested at raster

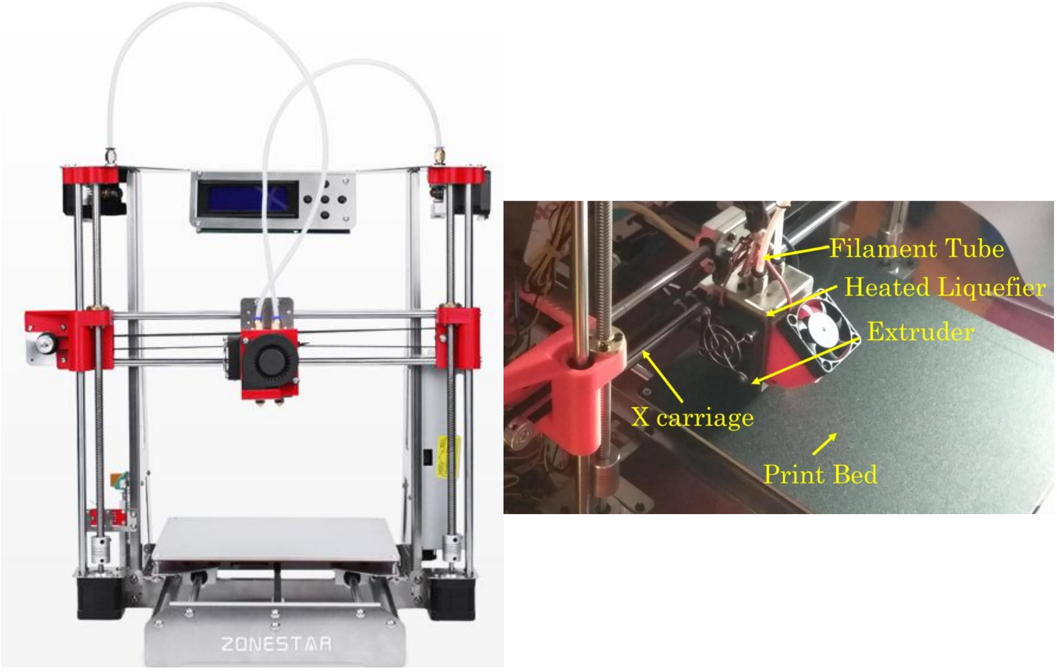

Figure 4.2: FDM Printer

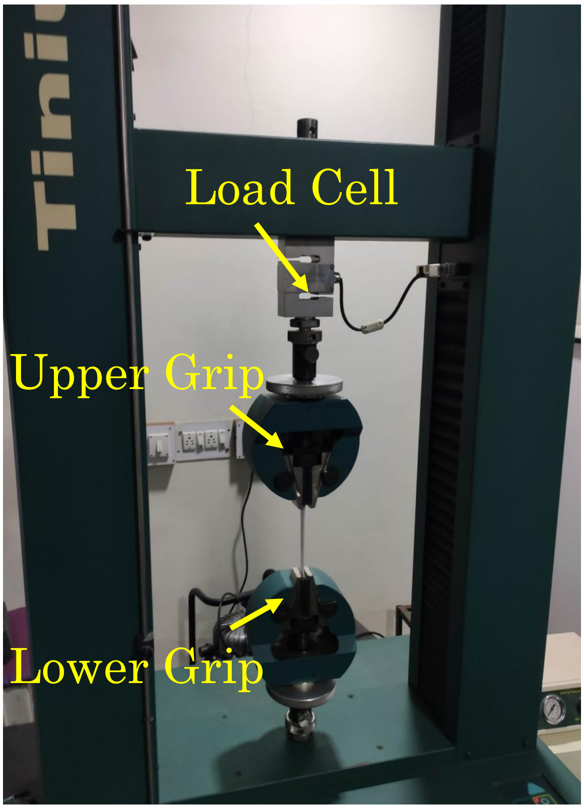

Figure 4.3: Tensile testing machine

angles of $\theta = 0°, 45°$, and $90°$, for a h of 0.12 mm. Similarly, Figure 4.4b and Figure 4.5a present detailed views of the tensile tested specimens corresponding to layer heights of 0.23 mm and 0.35 mm, respectively, across all three raster orientations. Additionally, Figure 4.5b provides a close up view of the specimen surfaces, clearly highlighting the raster deposition path and printing direction relative to the loading axis.

(a) $h = 0.12$ mm (b) $h = 0.23$ mm

Figure 4.4: Tensile tested ASTM D638-14 specimens with $\theta = 0°, 45°, 90°$ (a) $h = 0.12$ mm (b)$h = 0.23$ mm

Following the mechanical testing, the experimental stress (σ)-strain (ϵ) curves for all examined configurations are compiled and presented in Figure 4.6. Figure 4.6a, Figure 4.6b and Figure 4.6c shows σ- ϵ curves for $h = 0.12$, $h = 0.23$ and $h = 0.35$ mm respectively. Here Based on these results, the key material properties were derived: the elastic modulus in the longitudinal direction (E_1) was measured from the $0°$ orientation, the modulus in the transverse direction (E_2) from the $90°$ orientation, and the modulus for the shear related orientation (E_{45}) was obtained from the $45°$ specimens. The shear modulus(G_{12})[53][36] was calculated using relation

$$G_{12} = 1/(\frac{4}{E_{45}} - \frac{1}{E_1} - \frac{1}{E_2} + \frac{2\mu_{12}}{E_1}) \tag{4.1}$$

The results are reported in table 4.1 for all cases. Values which mentioned in the table have been determined by taking linear portion of the σ- ϵ diagram and slope has been calculated by doing a linear fit. Based on the analysis of the experimental

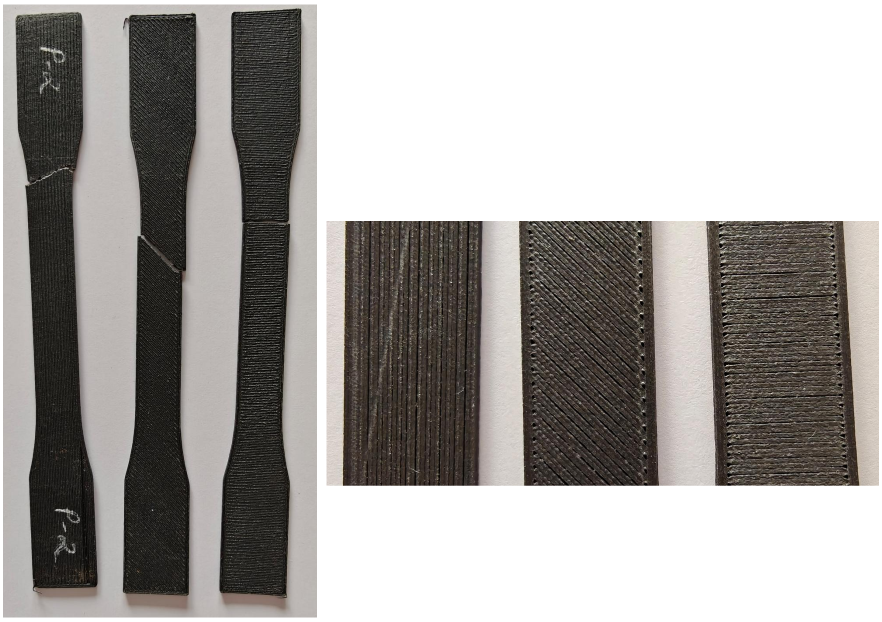

(a) $h = 0.35$ mm (b)

Figure 4.5: (a) Tensile tested ASTM D638-14 specimens with $\theta = 0°, 45°, 90°$ and $h = 0.35$ mm. (b)Close view near specimen

test results, it has been observed that the modulus of elasticity E decreases as the layer height h increases.

Table 4.1: Tensile Test Results for CPLA Specimens

Layer (h) (mm)	E_1 (MPa)	E_{45} (MPa)	E_2 (MPa)	ν_{12}	G_{12} (MPa)
0.35	1980	1561	980	0.36	713.96
0.23	2085	1642	1028	0.36	752.44
0.12	2189	1730	1057	0.36	807.7

Ultimate tensile strength (UTS) has been determined by taking the ratio of maximum load reach during the test and the c/s area. The constitutive mechanical properties of the CPLA laminates, constructed from individual CPLA laminae, were derived using the framework of Classical Laminated Plate Theory (CLT). This theoretical approach is fundamentally based on the kinematic assumptions of Kirchhoff's hypothesis for thin plates and is widely cited in composite mechanics literature [36, 54]. By applying the governing equations of CLT, the effective stiffness and compliance matrices were calculated for the specific laminate stacking orientations utilized in this study. To automate and ensure the accuracy of these complex matrix

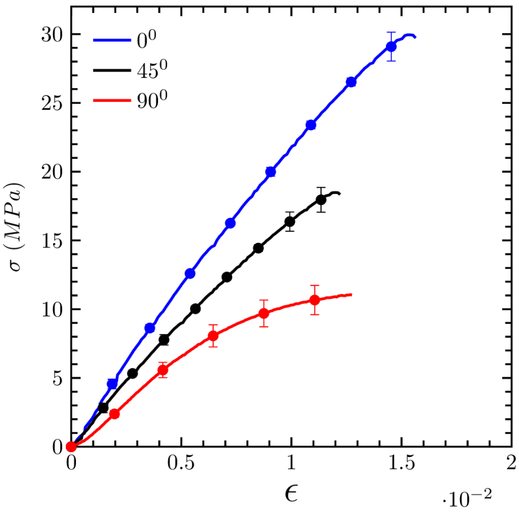

(a) $h = 0.12$ mm

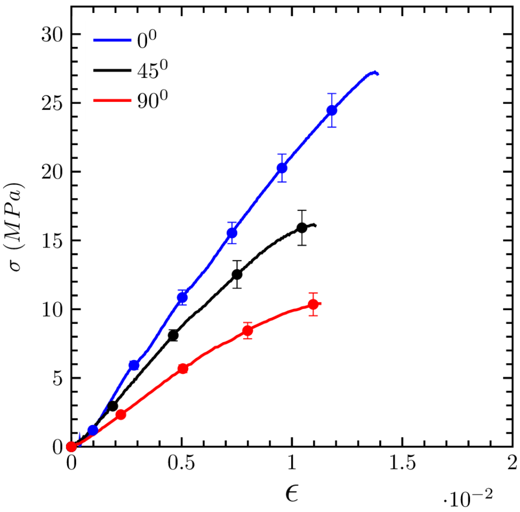

(b) $h = 0.23$ mm

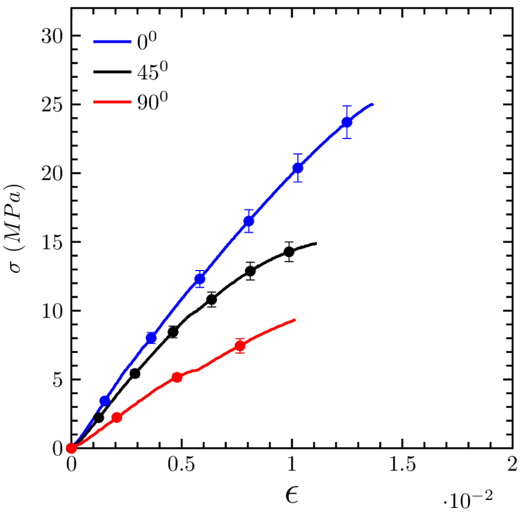

(c) $h = 0.35$ mm

Figure 4.6: Stress - Strain Curve (a) $h = 0.12$ mm (b)$h = 0.23$ mm mm (c) $h = 0.35$ mm

operations, a dedicated computational script was developed using MATLAB. The complete source code and algorithmic details are provided in Appendix A.

4.2 Size Effect analysis

According to the classical theories of elasticity and plasticity, it is assumed that every structure fabricated from the same material possesses a nominal strength that is independent of the structure's physical size. However, when analyzing geometrically similar structures, any deviation from this size independent behavior is referred to as the Size Effect. Fundamentally, the size effect characterizes the dependency of the nominal strength (σ_N) on the structure's characteristic dimension, which is typically represented by the width (D).

This phenomenon is primarily driven by the release of stored energy during fracture. It becomes particularly significant in the analysis of concrete, rocks, ceramics and quasi brittle materials. Research has established that the size effect represents a transitional behavior bridging the gap between plastic limit analysis (where strength is constant) and Linear Elastic Fracture Mechanics (LEFM), where the size effect is most pronounced. A detailed theoretical background and derivation of the size effect have been discussed in Sections 4.3.1 and 4.3.2.

4.2.1 Specimen Preparation

To determine size effect, three sets of Single edge notched tension (SENT) and Double edge notched tension (DENT) specimens were prepared using FDM with CPLA filament (see Figure 4.7 and Figure 4.11). Each specimen set had a total thickness (t in mm) of 0.7 , 1.4 , 2.1 and a layer height (h in mm) of 0.12 , 0.23 , 0.35 respectively. The specimens were fabricated using a six ply laminate structure arranged in a symmetric $[\pm 45/0]_s$ stacking sequence (see Fig 4.10). To induce fracture, initial pre cracks were precision cut using a laser. Notched size in SENT specimen was taken as D/5 where D is the width of specimen and notched size in DENT specimen was taken as D/16 [44]. Specimens of different sizes which were geometrically scaled as 1:2:3:4 as shown in the Table 4.2 for SENT. L/D ratio is kept constant in all specimens as 2.225. All the specimens had gripped with 38 mm gripping section. The length of gripping section is constant (not scaled) in all specimen because the failure of specimen occurs at a maximum distance from the grips. Table4.2 shows the dimensions of the SENT specimens. Figure 4.7 shows the schematic geometry of the specimens. other printing parameter for FDM process are kept same as discussed in 4.1

Table 4.2: Dimensions of the SENT specimens (mm).

Size	Width(D)	Gauge length,L	Length	Crack Length(a)	Thickness
1	7.5	16.69	92.69	1.5	0.7 1.4 2.1
2	15	33.39	109.38	3	0.7 1.4 2.1
3	22.5	50.06	126.06	4.5	0.7 1.4 2.1
4	30	66.75	142.75	6.0	0.7 1.4 2.1

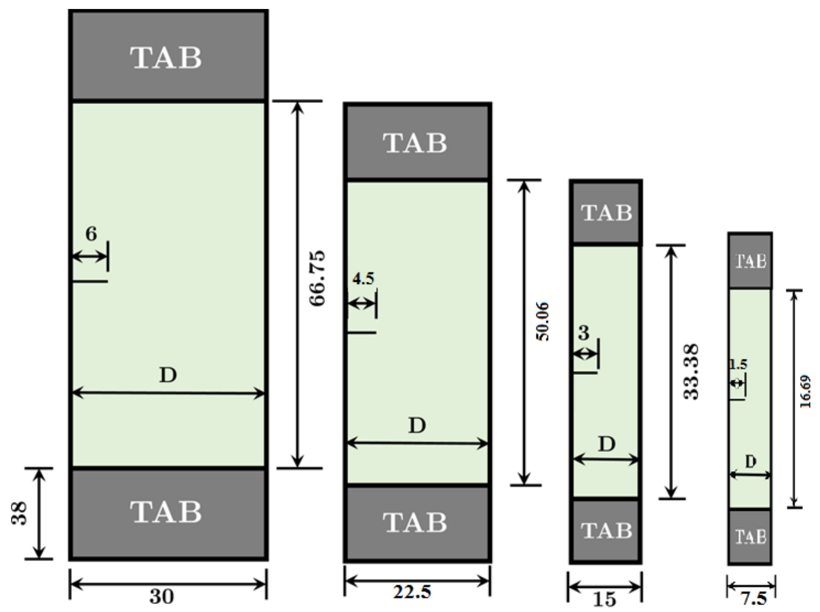

Figure 4.7: Schematic of SENT specimens (Dimensions are in mm)

3d printed CPLA material SENT specimens are shown in Figure 4.8 and 4.9.

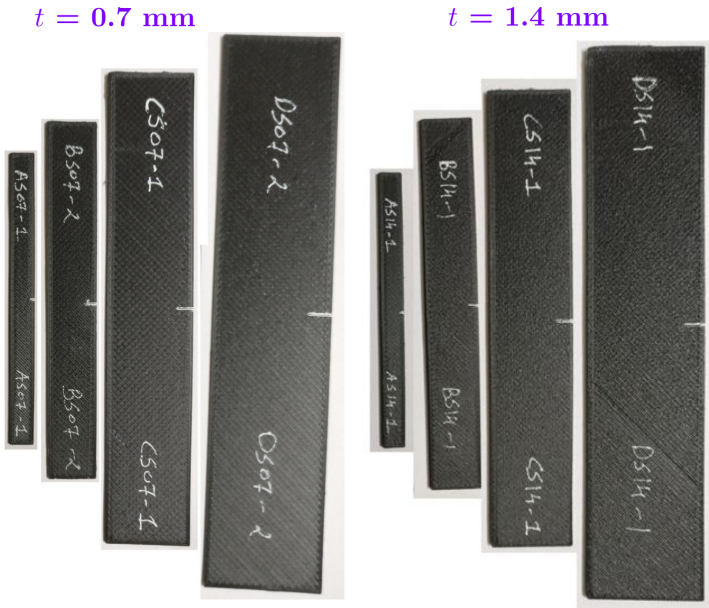

Figure 4.8: 3D printed SENT specimen

Figure 4.9: 3D printed SENT specimen

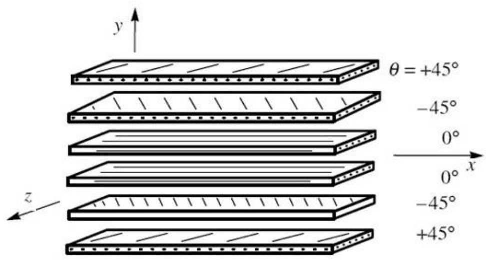

Figure 4.10: Layer wise raster angle

Table 4.3 and Figure 4.11 shows the dimensions and the geometrical representation of DENT specimens.

Table 4.3: Dimensions of the DENT specimens (mm).

Size	Width(D)	Gauge length,L	Length	Crack Length(a)	Thickness
					0.7
1	7.5	16.69	92.69	0.468	1.4
					2.1
					0.7
2	15	33.39	109.38	0.937	1.4
					2.1
					0.7
3	22.5	50.06	126.06	1.4	1.4
					2.1
					0.7
4	30	66.75	142.75	1.1875	1.4
					2.1

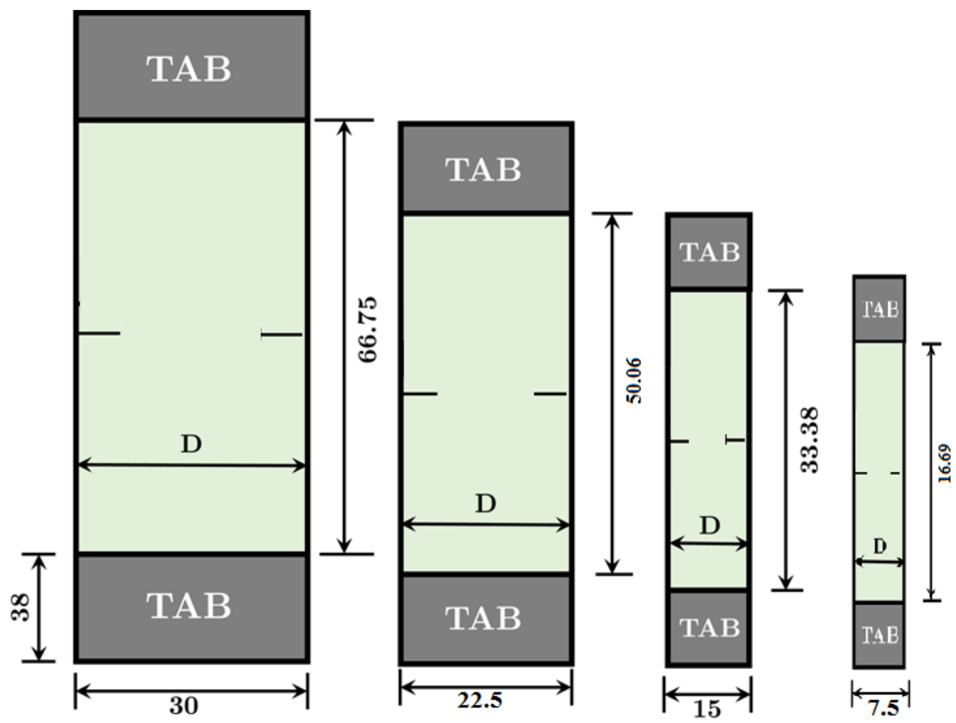

Figure 4.11: Schematic of DENT specimens (Dimensions are in mm)

4.3 Mechanical Testing and Results

Tensile testing was conducted on UTM having load cell of 5000 N. To ensure consistent loading conditions, the displacement rate was maintained at a constant 2 mm/min. During the experiments,load (P) and displacement(Δ) data were recorded for further analysis. The Ductility Level (D_L) was calculated according to Martinez AB et al. [28]. Since the measured value is less than 0.15 ($D_L < 0.15$), the material exhibits quasi-brittle behavior. From the recorded P-Δ data, the Nominal Strength (σ_N) was derived. This parameter is defined as the ratio of the maximum recorded load (P_{max}) to the initial cross sectional area of the specimen. SENT and DENT specimens after tensile testing are shown in Figure 4.12,Figure 4.13a, Figure 4.14 and Figure 4.13b.

The experimental $P - \Delta$ curves, encompassing SENT specimens of varying widths (D) and thicknesses (t), are systematically presented in Figure 4.15. Specifically, Figures 4.15a, 4.15b, and 4.15c correspond to specimen thicknesses of 0.7 mm, 1.4 mm, and 2.1 mm, respectively. To ensure statistical reliability, Three to four identical specimens were tested for each geometric configuration. Consequently, the plotted curves represent the mean response of these tests.

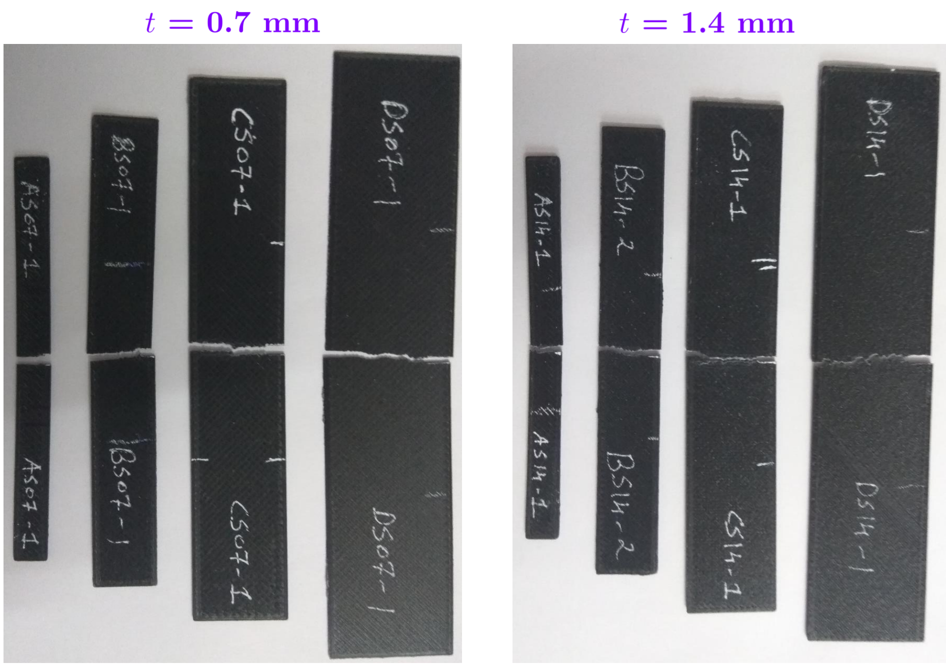

Figure 4.12: SENT specimens after tensile testing

t = **2.1 mm**

(a)

t = **2.1 mm**

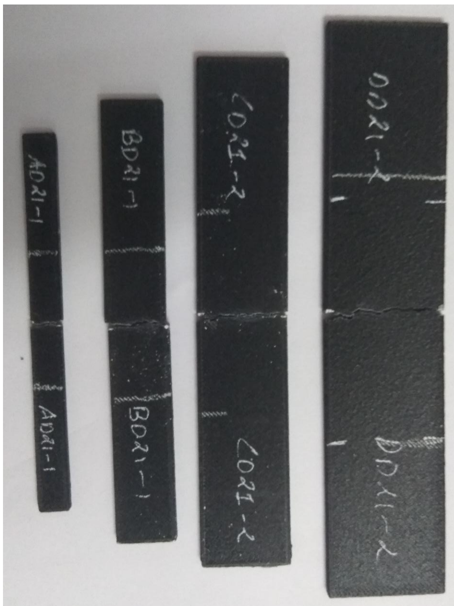

(b)

Figure 4.13: (a)SENT (b) DENT specimens after tensile testing

t = **0.7 mm**

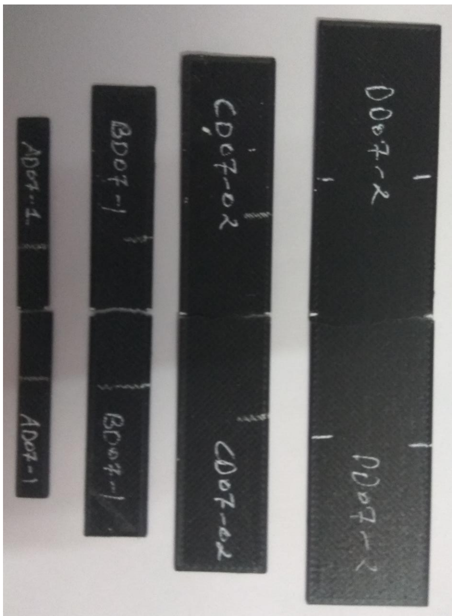

t = **1.4 mm**

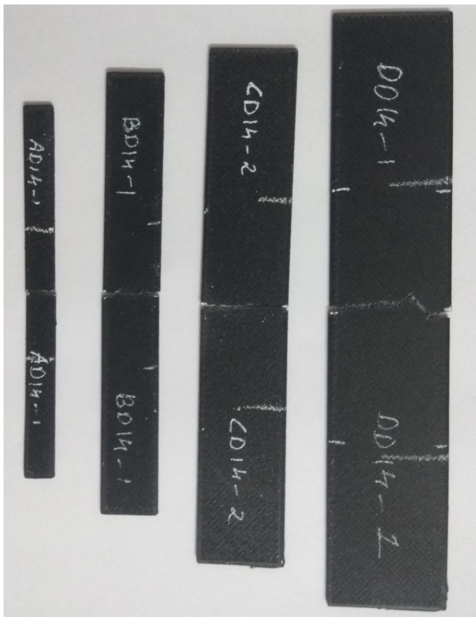

Figure 4.14: DENT specimens after tensile testing

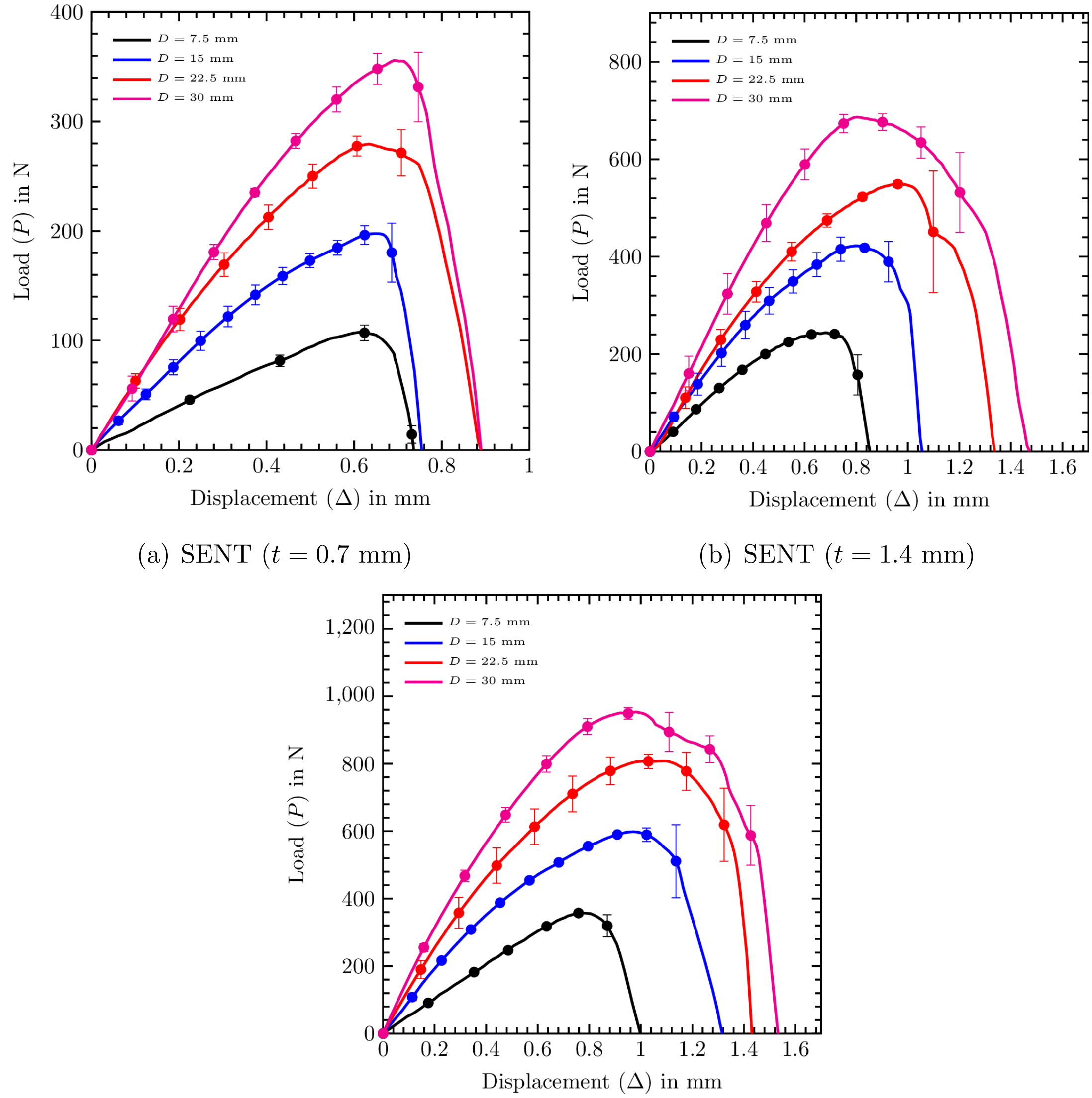

(a) SENT ($t = 0.7$ mm)

(b) SENT ($t = 1.4$ mm)

(c) SENT-($t = 2.1$ mm)

Figure 4.15: $P - \Delta$ diagram of SENT specimens

For the sake of visual clarity and to prevent the overlapping of data points, error bars representing the variance in load are displayed at selected displacement intervals rather than continuously. The recorded $P - \Delta$ curves exhibit a predominantly linear response up to the point of fracture, behavior that underscores the inherent brittleness of the material. In this linear region, the experimental consistency is high, resulting in minimal scatter and small error bars across the specimen sets. In contrast, the deviation into non linear behavior immediately following the peak load signals the onset of inelastic deformation. This non linearity is indicative of inelastic hardening behavior and the development of a fracture process zone, suggesting a reduction in brittleness (or a quasi-brittle response) at smaller scales. Consequently, catastrophic failure occurs abruptly after the maximum load is reached. The physical failure mechanisms were identified as a combination of inter-layer delamination and intra layer microcracking. This complex, stochastic damage process in the post peak regime leads to significant divergence in the $P-\Delta$ curves among identical specimens, which is visually represented by a substantial increase in the magnitude of the error bars.

The tensile test results for the SENT specimens of varying sizes are summarized in Tables 4.4, 4.5, and 4.6. According to classical strength based failure criteria, the nominal strength should theoretically remain independent of the specimen size. However, the data presented in Table 4.4 demonstrates a significant deviation from this theory, revealing a notable decrease in nominal strength (σ_N) as the specimen size (D) increases, thereby confirming the existence of a size effect.

Table 4.4: Tensile test results for SENT specimens with $t = 0.7$ mm

Specimen	Specimen width	Average Load P_{avg}(N)	Average Nominal strength (σ_N)(MPa)
1	7.5	110.52	21.05
2	15	203.33	19.36
3	80	286.78	18.2
4	80	357.54	17.02

Table 4.5: Tensile test results for SENT specimens with $t = 1.4$ mm

Specimen	Specimen width	Average Load P_{avg}(N)	Average Nominal strength (σ_N)(MPa)
1	7.5	241.39	22.99
2	15	431.4	20.54
3	80	550.8	17.48
4	80	687.22	16.36

Table 4.6: Tensile test results for SENT specimens with $t = 2.1$ mm

Specimen	Specimen width	Average Load P_{avg}(N)	Average Nominal strength (σ_N)(MPa)
1	7.5	361.08	22.92
2	15	599.84	19.04
3	80	829.33	17.55
4	80	960.24	15.24

Similarly, the data obtained from the tensile testing of the DENT specimens is presented in Figure 4.16. Specifically, Figures 4.16a, 4.16b, and 4.16c correspond to specimen thicknesses of 0.7 mm, 1.4 mm, and 2.1 mm, respectively. Furthermore, the detailed numerical values associated with these tests are tabulated in Tables 4.7, 4.8, and 4.9. Here also size effect observed in the test data result.

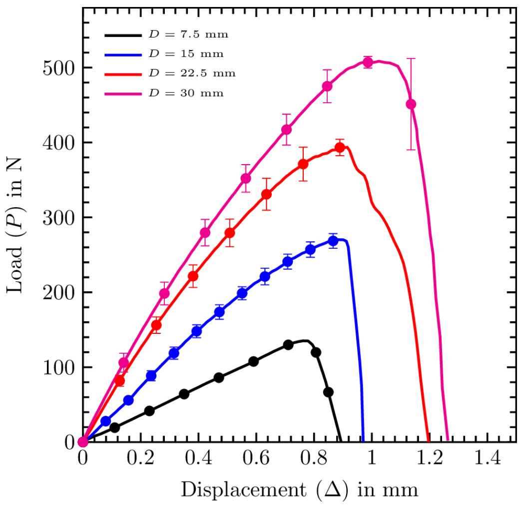

(a) DENT-($t = 0.7$ mm)

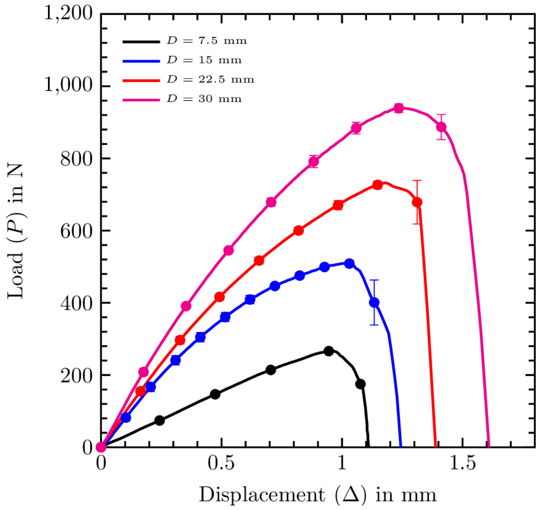

(b) DENT-($t = 1.4$ mm)

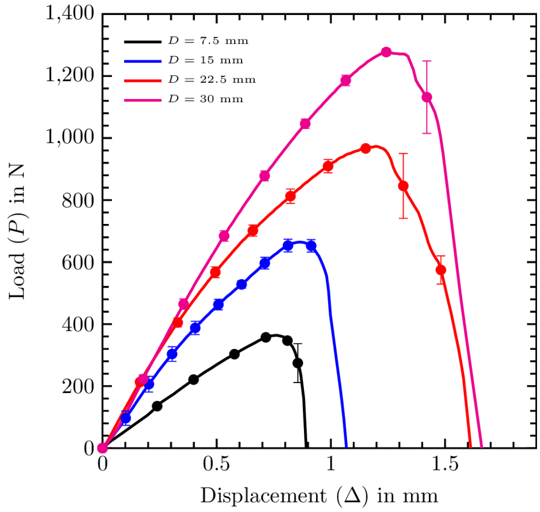

(c) DENT-($t = 2.1$ mm)

Figure 4.16: $P - \Delta$ diagram of DENT Specimens

Table 4.7: Tensile test results for DENT specimens with $t = 0.7$ mm

Specimen	Specimen width	Average Load P_{avg}(N)	Average Nominal strength (σ_N)(MPa)
1	7.5	141.74	26.99
2	15	276.32	26.31
3	80	399.87	25.38
4	80	525.09	25.00

Table 4.8: Tensile test results for DENT specimens with $t = 1.4$ mm

Specimen	Specimen width	Average Load P_{avg}(N)	Average Nominal strength (σ_N)(MPa)
1	7.5	267.80	25.5
2	15	510.08	24.28
3	80	740.72	23.51
4	80	945.056	22.5

Table 4.9: Tensile test results for DENT specimens with $t = 2.1$ mm

Specimen	Specimen width	Average Load P_{avg}(N)	Average Nominal strength (σ_N)(MPa)
1	7.5	365.02	23.17
2	15	680.15	21.59
3	22.5	969.5	20.51
4	30	1295.05	20.55

4.3.1 Analysis of test results using Size Effect Law

The fracture behavior of geometrically similar structures containing pre existing notches is effectively described by the Type-II SEL proposed by [43, 55]. This fundamental law establishes a critical relationship between the nominal strength of the structure (σ_N) and its characteristic dimension (D).

To extract the fracture parameters from the experimental test data, a regression analysis was performed. According to Bazant [43], the Type-II size effect for quasi brittle materials is mathematically expressed as:

$$\sigma_N = \sigma_0 \left(1 + \frac{D}{D_0}\right)^{-\frac{1}{2}} \tag{4.2}$$

In this formulation, $\sigma_N = P_{max}/(tD)$ represents the nominal strength (where t is the thickness), while σ_0 and D_0 are material constants dependent on the FPZ and the specific specimen geometry. To determine these constants experimentally, the non linear equation (4.2) can be linearized into a standard linear regression form:

$$Y = C + AX \tag{4.3}$$

Here, the transformed variables are defined as $Y = \sigma_N^{-2}$ and $X = D$. Consequently, the fracture parameters can be derived from the slope (A) and the y-intercept (C) of the regression line, where $D_0 = C/A$ and $\sigma_0 = 1/\sqrt{C}$.

Using the experimental results, a linear regression was conducted by plotting Y against X. Figure 4.17a illustrates this linear fit specifically for the SENT specimens with a thickness of $t = 0.7$ mm, yielding a characteristic size $D_0 = 35.52$ mm.

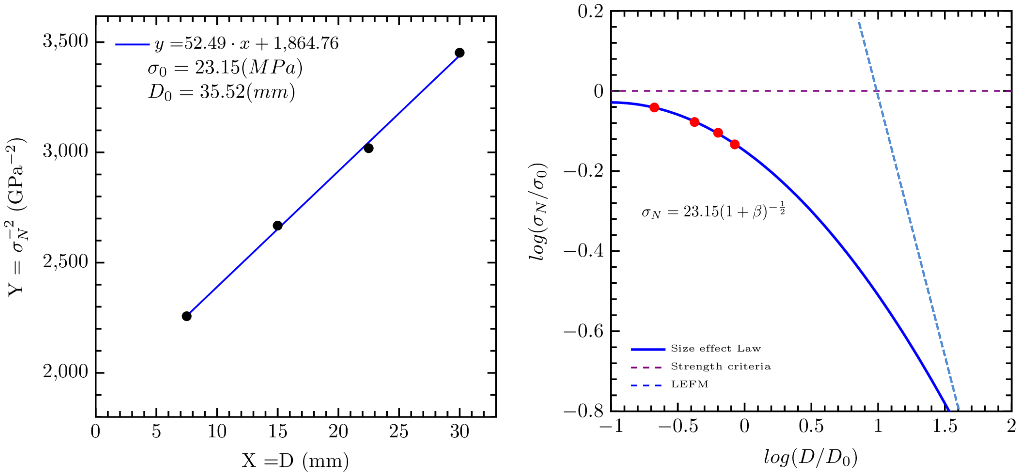

(a)

(b)

Figure 4.17: SENT specimens ($t = 0.7$ mm): (a) Regression analysis for size effect parameters; (b) Obtained Size Effect Law

This regression methodology was systematically repeated for the remaining specimen groups. The linear regression analysis curves for the remaining SENT and DENT specimen thicknesses are presented in Appendix C. Following the determination of σ_0 and D_0, the theoretical SEL was generated by plotting the normalized strength (σ_N/σ_0) against the brittleness number ($\beta = D/D_0$). Figure 4.17b depicts this comparison for the 0.7 mm thickness group. The complete set of extracted fracture parameters and the resulting SEL equations for all thicknesses are summarized in Table 4.10 for SENT and Table 4.10 for DENT

The logarithmic plot in Figure 4.17b visually captures the transition in failure mechanisms. The curve typically spans from the plastic limit (indicated by a horizontal asymptote with slope 0) to Linear Elastic Fracture Mechanics (LEFM)

Table 4.10: Summary of Extracted Size Effect Parameters for SENT Specimens

Thickness(t) (mm)	D_0 (mm)	σ_0 (MPa)	Derived Size Effect Law
0.7	35.52	23.15	$\sigma_N = 23.15(1+\beta)^{-\frac{1}{2}}$
1.4	14.09	28.75	$\sigma_N = 28.75(1+\beta)^{-\frac{1}{2}}$
2.1	11.015	29.74	$\sigma_N = 29.74(1+\beta)^{-\frac{1}{2}}$

Table 4.11: Summary of Extracted Size Effect Parameters for DENT Specimens

thickness(t) (mm)	D_0 (mm)	σ_0 (MPa)	Derived Size Effect Law
0.7	123.02	27.78	$\sigma_N = 27.78(1+\beta)^{-\frac{1}{2}}$
1.4	73.58	26.74	$\sigma_N = 26.74(1+\beta)^{-\frac{1}{2}}$
2.1	77.48	23.89	$\sigma_N = 23.89(1+\beta)^{-\frac{1}{2}}$

behavior (indicated by an asymptote with a slope of -0.5). This representation explicitly demonstrates: (1) the significant influence of structural size on the failure stress of FDM printed CPLA components, and (2) the gradual transition from strength based failure to fracture mechanics governed failure. These findings are important for structural design and safety assessment. They allow for the extrapolation of laboratory scale prototype data to predict the load bearing capacity of large scale structural parts, specifically those susceptible to stable crack growth prior to catastrophic failure. Furthermore, the variation in parameters across Table 4.10 and Table 4.11suggests that the Size Effect Law is distinctively influenced by the specimen thickness and the associated fracture lengths.

4.3.2 Determination of fracture properties from the SEL

Bao et al. [56] derived analytical solutions for both the stress intensity factor and the energy release rate in orthotropic materials. The functional relationship between the energy release rate and the normalized crack length is expressed as The energy release rate, $G(\alpha)$, is related to the stress intensity factor, K_I, and the effective modulus, E^*, by the expression:

$$G(\alpha) = \frac{K_I^2}{E^*} \tag{4.4}$$

By defining the geometric shape function as $g(\alpha) = \pi\alpha[F(\alpha)]^2$, the relationship can be expressed in terms of the nominal stress σ_N:

$$G(\alpha) = \frac{\sigma_N^2 D}{E^*} g(\alpha) \tag{4.5}$$

The effective modulus for the orthotropic material, E^*, is determined by:

$$E^* = \frac{1}{[Y(\rho)]^2}\sqrt{\frac{2E_xE_y\sqrt{\lambda}}{1+\rho}} \tag{4.6}$$

In Equation (4.6), the term $g(\alpha)$ represents the dimensionless form of the energy release rate, while E^* denotes the effective elastic modulus, which is a function of the material's orthotropic parameters. For the DENT specimens:

$$F(\alpha) = (0.122\cos^4\frac{\pi\alpha}{2} + 1)\sqrt{\tan(\frac{\pi\alpha}{2})\frac{2}{\pi\alpha}} \tag{4.7}$$

For the SENT specimens,

$$F(\alpha) = (10.55\alpha^2 + 30.38\alpha^4 - 0.231\alpha - 21.71\alpha^3 + 1.122) \tag{4.8}$$

According to the theoretical framework established by Bažant [43], there is a direct correlation between D and σ_N. This relationship is presented below

$$\sigma_N = \sigma_0\left[1 + \frac{D}{D_0}\right]^{-1/2} \tag{4.9}$$

The geometry-dependent constants, D_0 and σ_0, are defined based on the fracture energy G_f and the effective modulus E^*:

$$D_0 = \frac{c_f g'(\alpha_0)}{g(\alpha_0)} \tag{4.10}$$

$$\sigma_0 = \sqrt{\frac{E^*G_f}{c_f g'(\alpha_0)}} \tag{4.11}$$

The constants σ_0 and D_0 can be evaluated from the regression analysis of experimental data as mentioned in section In Eq. (4.10), $g(\alpha) = \pi\alpha[F(\alpha)]^2$. Thus, for the DENT:

$$g(\alpha) = \tan\frac{\pi\alpha}{2}2\left(0.122\cos^4\frac{\pi\alpha}{2} + 1\right)$$

$$g'(\alpha) = \left[\left(1 + 0.122\cos^4\frac{\pi\alpha}{2}\right)\left(\tan\frac{\pi\alpha}{2}\right) - 0.244\sin^2\pi\alpha\left(0.122\cos^4\frac{\pi\alpha}{2} + 1\right)\right]\pi \tag{4.12}$$

where, $\alpha = 0.125$ for DENT.
For the SENT specimens,

$$g(\alpha) = \pi\alpha\left(-21.71\alpha^3 + 30.38\alpha^4 - 0.231\alpha + 10.55\alpha^2 + 1.122\right)^2$$

$$g'(\alpha) = \frac{dg(\alpha)}{d\alpha}$$

$$g'(\alpha) = \pi\left(947.5\alpha^4 + 71.18\alpha^2 - 1.037\alpha - 214.4\alpha^3 + 1.259\right) \tag{4.13}$$

where, $\alpha = 0.2$ for SENT and DENT specimens. Eq. (4.11) can be rewritten as,

$$G_f = \frac{\sigma_0^2}{E^*} g(\alpha_0) D_0, \; c_f = D_0 \frac{g(\alpha_0)}{g'(\alpha_0)} \tag{4.14}$$

Substituting the experimentally determined parameters σ_0 and D_0 (listed in Table 4.10 for SENT and Table 4.11 for DENT) into Equation (4.14) allowed for the calculation of the fracture energy (G_f) and the effective length of the fracture process zone (c_f). The resulting values from this derivation are summarized in Table 4.12

Table 4.12: Fracture Properties of SENT and DENT CPLA material obtained by SEL

t (mm)	SENT		DENT	
	G_f (kJ/m^2)	c_f (mm)	G_f (kJ/m^2)	c_f (mm)
0.7	11.4	4.213	11.9	7.6458
1.4	7.73	1.6710	6.59	4.5733
2.1	6.49	1.306	5.37	4.6713

As observed in Table 4.12, both the fracture energy (G_f) and the FPZ length (c_f) exhibit a downward trend as the specimen thickness t increases. Conversely, when comparing the two different geometries (SENT vs. DENT), the calculated G_f values are nearly identical. This consistency indicates that the fracture energy is not dependent on the specimen geometry.

Following Bazant [57], the fracture resistance curve (R-curve) is established using a parametric approach defined by the following pair of equations:

$$R(c) = \frac{c g'(\alpha)}{c_f g'(\alpha_0)} G_f \tag{4.15}$$

$$\frac{c}{c_f} = \left(\alpha_0 + \frac{g(\alpha)}{g'(\alpha)} - \alpha \right) \frac{g'(\alpha_0)}{g(\alpha_0)} \tag{4.16}$$

To reconstruct the R-curve envelope, the material constants G_f and D_0 are first extracted using the SEL. Subsequently, a range of values for the relative crack length parameter, α, is selected. For each increment of α, the equivalent structural dimension D is calculated as:

$$D = \frac{D_0 g(\alpha)}{g'(\alpha)(\alpha - \alpha_0)} - D_0 \tag{4.17}$$

Finally, the effective crack extension, c, is derived using the geometric relation:

$$c = D(\alpha - \alpha_0) \tag{4.18}$$

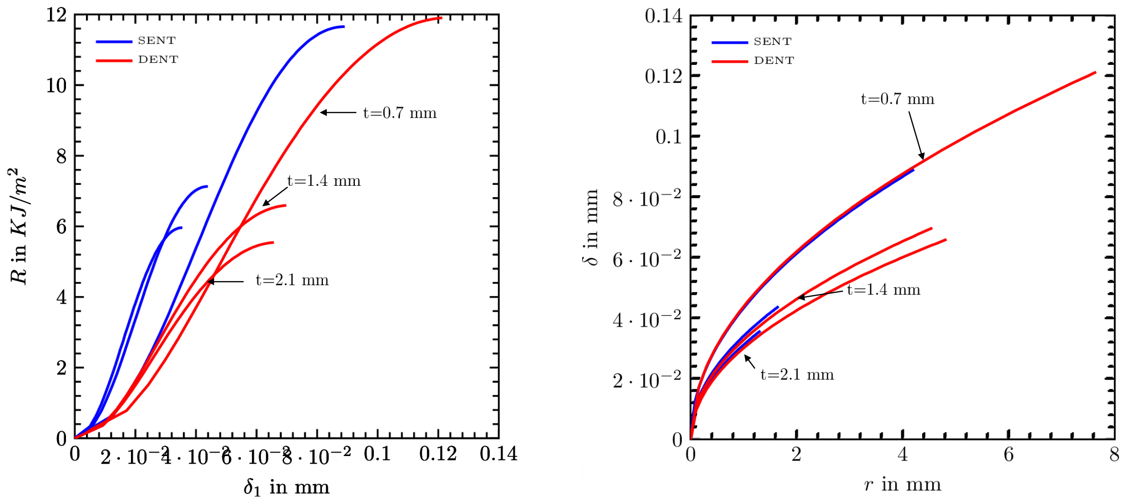

Figure 4.18: (a) Fracture energy to Opening of FPZ (δ) (b)FPZ to Normal opening of Fracture process zone (δ)

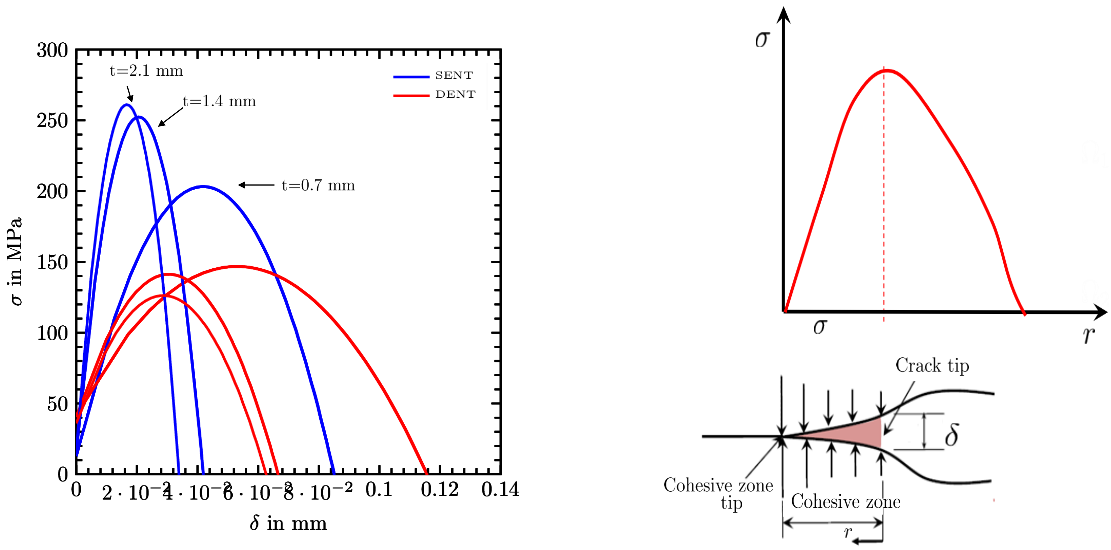

Figure 4.19: (a) Traction-separation Curve (b) Cohesive zone Model

The parametric system of equations defined in Eqs. (4.15)–(4.18) was solved numerically using Newton's iteration method, implemented via a custom MATLAB script. Complete MATLAB code is given in Appendix B This computational approach facilitated a detailed characterization of the R-curve, the FPZ evolution, and the resulting Traction Separation Curve (TSC). The derived R-curves, plotted with respect to the FPZ opening, reveal critical insights into the material's resistance behavior. As illustrated in Figure 4.18a for SENT and DENT specimens, the resistance R exhibits a clear dependency on specimen thickness; specifically, lower thickness specimens display higher R values, indicating a greater energy consumption capacity during fracture. When comparing geometries (Figure 4.19b), it is evident that while the peak magnitude of R is comparable for both SENT and DENT specimens, the profile of the curve is strongly geometry dependent. Notably, the SENT geometry reaches its maximum resistance at a significantly smaller FPZ opening compared to the DENT configuration. This variance underscores the necessity of determining geometry specific R-curves prior to conducting fracture analysis. The normal opening of the FPZ (δ) along the distance r from the crack tip was calculated for all configurations. As shown in Figure 4.18b, a distinct size effect is observed where thinner specimens develop a longer FPZ length.

Table 4.13: Comparison of G_f values for SENT and DENT specimens derived via SEL and TSC

	SENT		DENT	
t in mm	G_f by SEL (kJ/m^2)	G_f by TSC (kJ/m^2)	G_f by SEL (kJ/m^2)	G_f by TSC (kJ/m^2)
0.7	11.4	11.34	11.9	11.95
1.4	7.37	7.33	6.96	6.99
2.1	6.49	6.35	5.91	5.94

Furthermore, a geometric comparison reveals that DENT specimens maintain a significantly longer FPZ compared to SENT specimens, a finding consistent with their higher effective FPZ length (c_f). By applying a third order polynomial approximation to the normal opening data, the TSC was extracted. This curve serves as a vital constitutive law for defining cohesive element properties in Finite Element Method (FEM) simulations. Figure 4.19a demonstrate that the TSC is sensitive to both thickness and geometry. Specifically, the SENT geometry reaches peak stress at a smaller displacement opening compared to DENT. G_f was computed by calculating the area under the extracted TSCs. These results, summarized in Table 4.13, indicate that G_f increases with decreasing thickness. However, when comparing the two geometries, the integrated fracture energy remains effectively constant despite the differences in the shape of their traction laws. This consistency reinforces the classification of G_f as an intrinsic material property. Furthermore, the G_f values derived from the TSC method show excellent agreement with those obtained via SEL, validating the accuracy of the numerical approach.

4.4 Numerical Simulation using CZM

To validate the experimental findings and the applicability of the TSC derived from SEL, a numerical investigation was conducted. The study employed FEM to simulate crack propagation in both SENT and DENT specimens using the FEM software Abaqus Standard [58]. The simulation strategy utilized a Cohesive Zone Model (CZM), where the fracture behavior is governed by the TSC previously determined in Section 4.3.2 (see Fig. 4.19a). This approach allows for the correlation of the global load-displacement response with the local fracture process, providing a robust verification of the extracted material properties. Two dimensional (2D) plane stress FE models were developed to simulate the full range of specimen sizes and t (0.7 mm, 1.4 mm, and 2.1 mm) for both the SENT and DENT geometries. As illustrated in Figure 4.20, the model domain was partitioned into three distinct functional zones to accurately capture the mechanical behavior:

1. **Rigid Zone:** The gripping sections of the specimen were modeled as rigid bodies by assigning a high modulus of elasticity, ensuring that deformation is localized to the gauge length.

2. **Bulk Material Zone:** The CPLA laminate body was modeled using the engineering constants derived from CLT, as listed in Table 4.1 using MATLAB code for particular laminate orientation.

3. **Cohesive Zone:** The potential crack propagation path (ligament length) was modeled using a cohesive zone with zero geometric thickness. This zone shares nodes with the adjacent bulk material elements.

Similarly, Figure 4.22 shows the FE model for the DENT specimen. The discretization of the domain was performed using a structured meshing technique. The bulk material (Rigid and CPLA zones) was meshed using 4 node bilinear plane stress quadrilateral elements with reduced integration (CPS4R). The critical cohesive zone was meshed using 4 node two dimensional cohesive elements (COH2D4).To ensure numerical accuracy, a mesh sensitivity approach was adopted where the element density was significantly increased in the cohesive zone and the region immediately surrounding the crack tip (see Figure 4.21). For the SENT specimens, the total element count varied with size: 8,560 elements for $D = 7.5$ mm, increasing to 54,388 elements for $D = 30$ mm. A similar refinement strategy was applied to the DENT models.

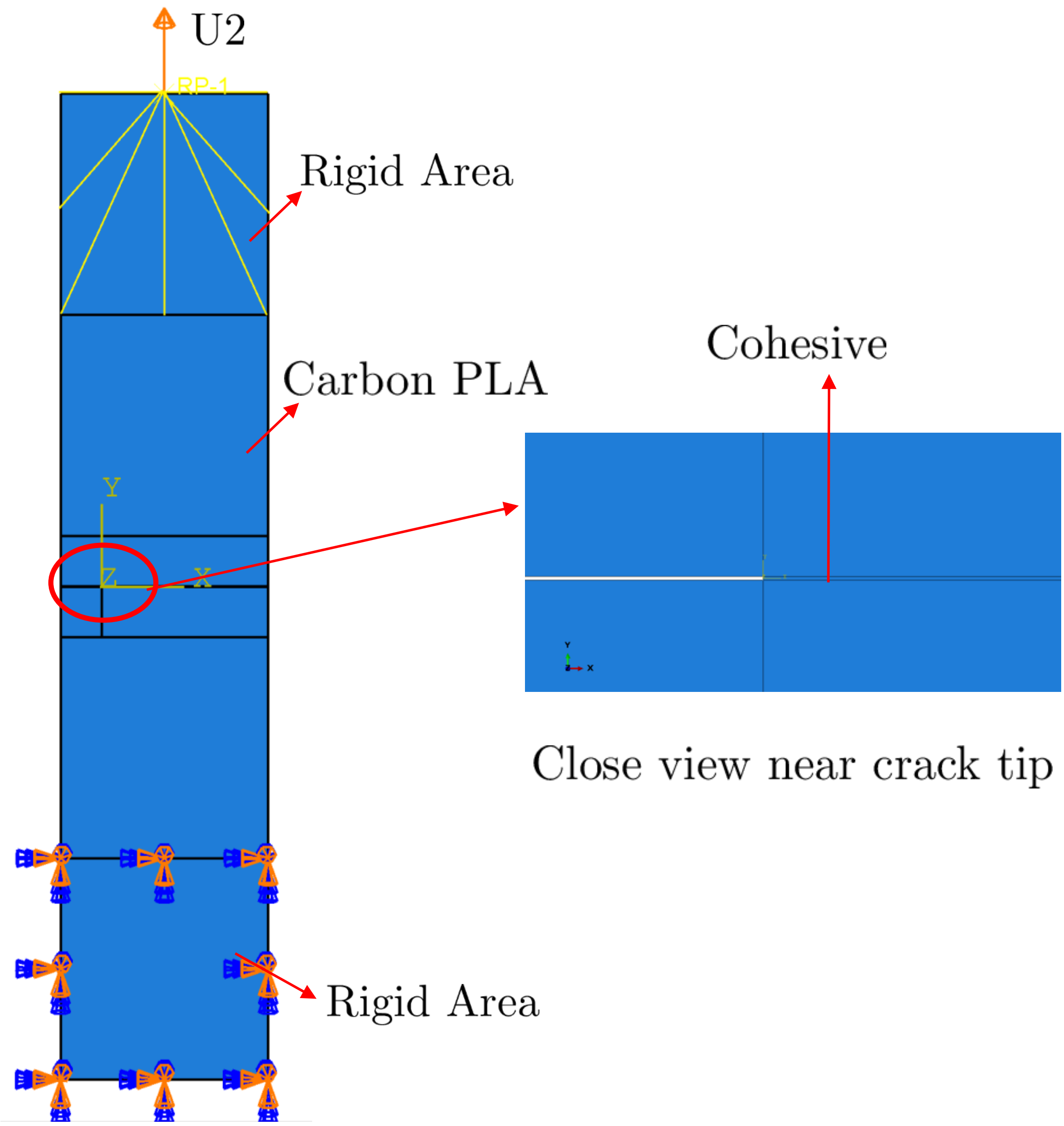

Figure 4.20: SENT Finite Element model with zones

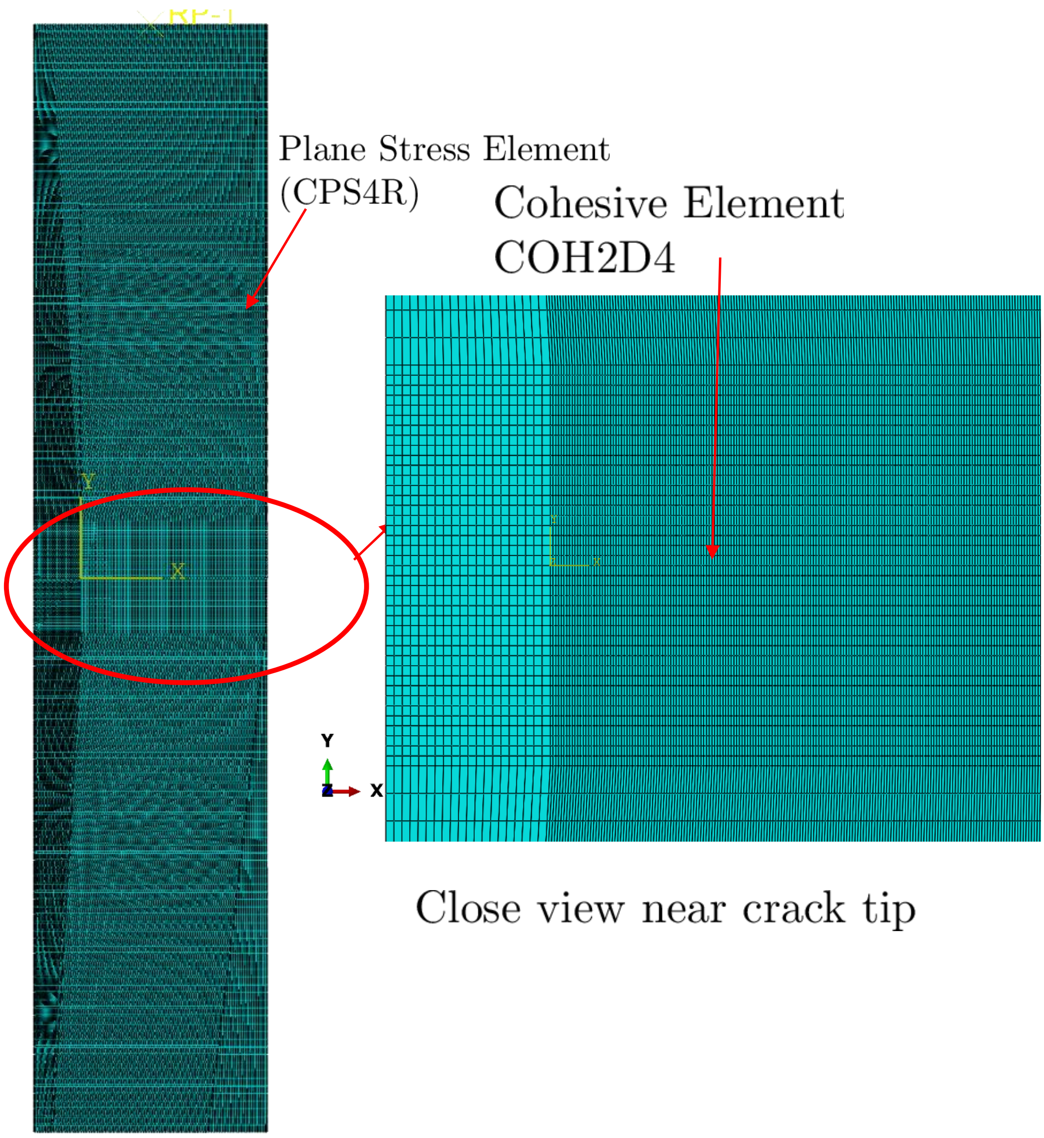

Figure 4.21: Mesh refinement in the cohesive zone.

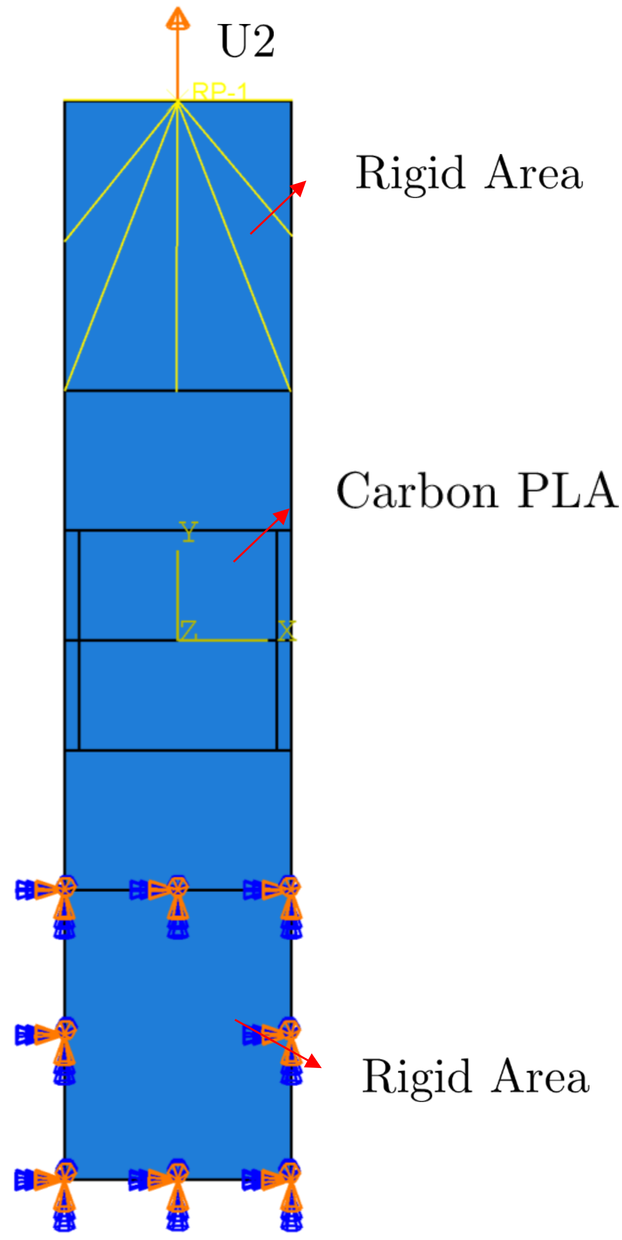

Figure 4.22: DENT Finite Element model with zones

The constitutive behavior of the cohesive elements was defined using the TSC derived from SEL. Taking the 2.1 mm thickness SENT specimen as a representative case, the linear elastic portion of the TSC (Point A to B in Figure 4.19a) was input as the initial stiffness. The softening branch (Point B to C in Fig. 4.19a), which governs damage evolution, was discretized into a tabular dataset comprising 15 to 20 points form Figure 4.19a. The other cohesive parameters were defined with an interface strength of 29 MPa and a viscosity coefficient of 0.04. Boundary conditions were applied to replicate the experimental tensile test setup. The bottom edge of the specimen was fully constrained (encastre), while a predefined displacement was applied to the top edge. The displacement magnitude was based on experimental failure limits, applied in increments ranging from 0.01 to 0.1 in a general static step. The numerical simulations were successfully converged for all specimen configurations. The global $P - \Delta$ responses obtained from the FEA were compared against the experimental datasets.

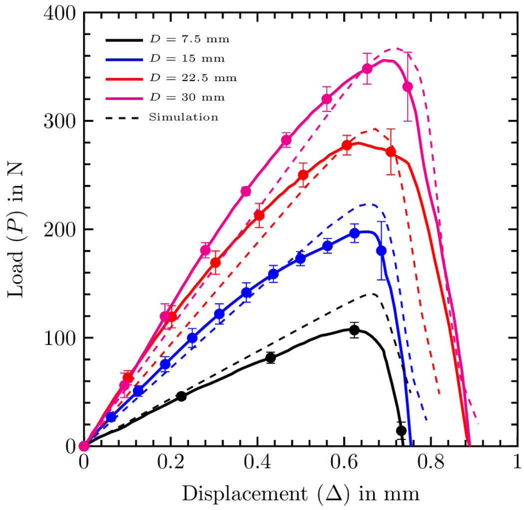

(a) SENT-($t = 0.7$ mm)

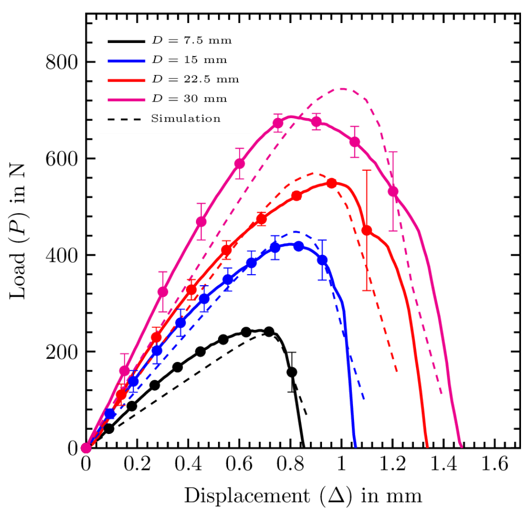

(b) SENT-($t = 1.4$ mm)

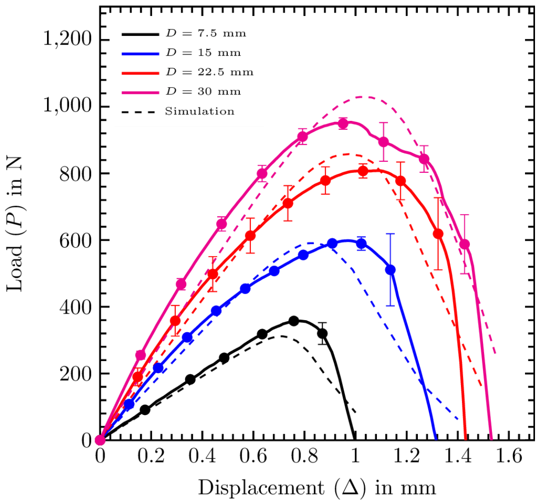

(c) SENT-($t = 2.1$ mm)

Figure 4.23: Comparison of Experimental and Numerical $P - \Delta$ response for SENT Specimens.

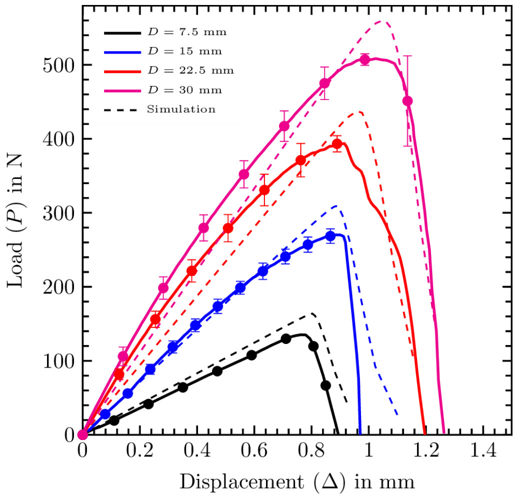

(a) DENT-($t = 0.7$ mm)

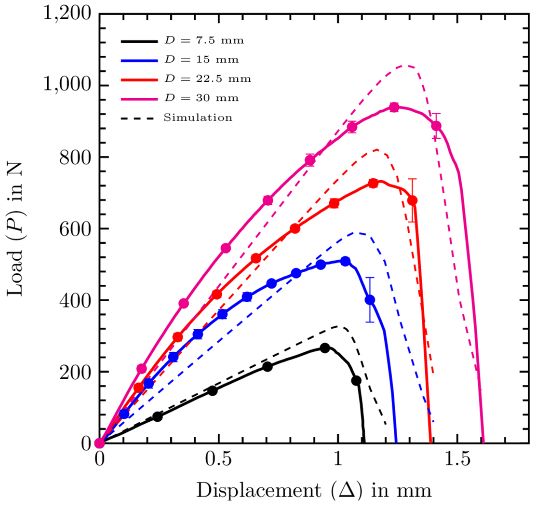

(b) DENT-($t = 1.4$ mm)

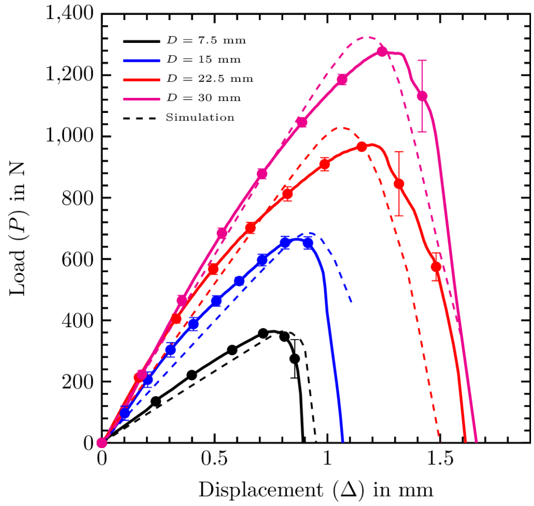

(c) DENT-($t = 2.1$ mm)

Figure 4.24: Comparison of Experimental and Numerical $P - \Delta$ response for DENT Specimens.

Figure 4.23 presents the comparison for SENT specimens across thicknesses of 0.7 mm, 1.4 mm, and 2.1 mm. Similarly, Figure 4.24 illustrates the validation for the DENT specimens. In the plots, the dashed lines represent the numerical predictions. The close agreement between $P - \Delta$ the experimental curves and the numerical results confirms that the traction separation curve derived from the SEL accurately captures the fracture energy and softening behavior of the FDM printed CPLA material. This validation suggests that the proposed SEL based method is a reliable tool for predicting the failure of cracked FDM components.

Chapter 5

Size Effect Analysis of FDM Specimens Fabricated from Polycarbonate

This chapter extends the size effect analysis to specimens fabricated from Polycarbonate (PC) using the FDM process. While the fundamental experimental methodology aligns with the procedures established in Chapter 4, this investigation specifically focuses on the influence of raster angle orientation on fracture behavior. In this study DENT specimens printed and used with varying raster angles. By applying Bažant's Type-II SEL [43] to the experimental data, the specific fracture energy (G_f) and the effective length of the fracture process zone (c_f) are determined for each raster configuration. This analysis aims to quantify how the deposition strategy affects the quasi-brittle fracture characteristics of PC.

5.1 Materials and Experimental Methods

The manufacturing process for PC specimens followed a 3D printing workflow similar to that described in the previous chapter 4. The 3D solid models were generated using Autodesk Inventor and subsequently exported as STL files. These files were processed using Simplify3D slicing software to generate the requisite G code for the FDM machine. The fabrication was carried out using a Zonestar FDM printer equipped with a 0.4 mm diameter nozzle with PC filament. For the printing process, the bed temperature was maintained at 110°C, while the nozzle temperature was fixed at 245°C. Rectilinear pattern used for Fabrication of all specimens other printing parameter are same as mentioned in 4.1. To maximize the structural density, the air gap between adjacent beads was set to 0 mm, and a 100% fill density was applied with a rectilinear infill pattern.

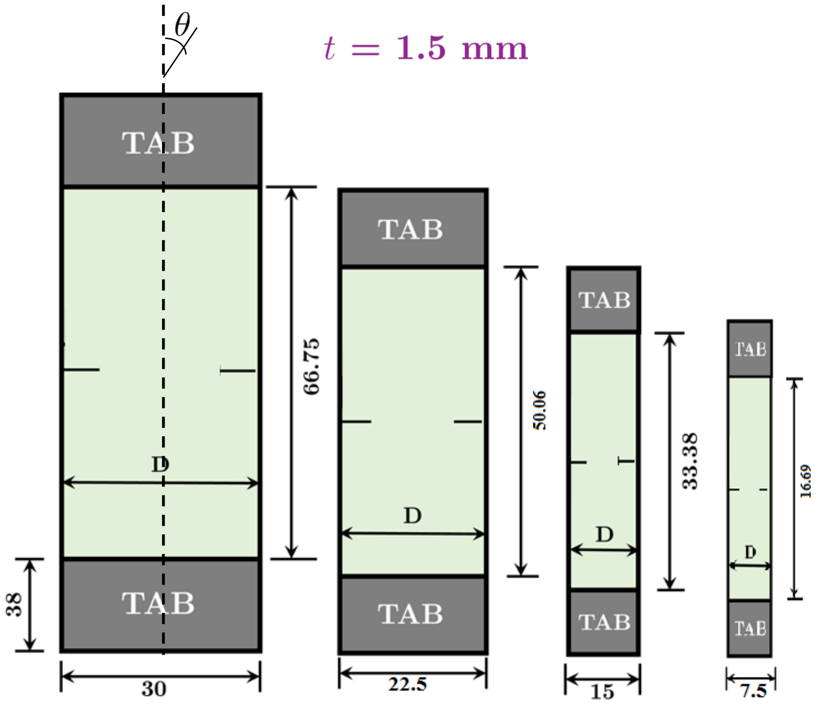

Figure 5.1: Schematic of DENT specimens (Dimensions are in mm)

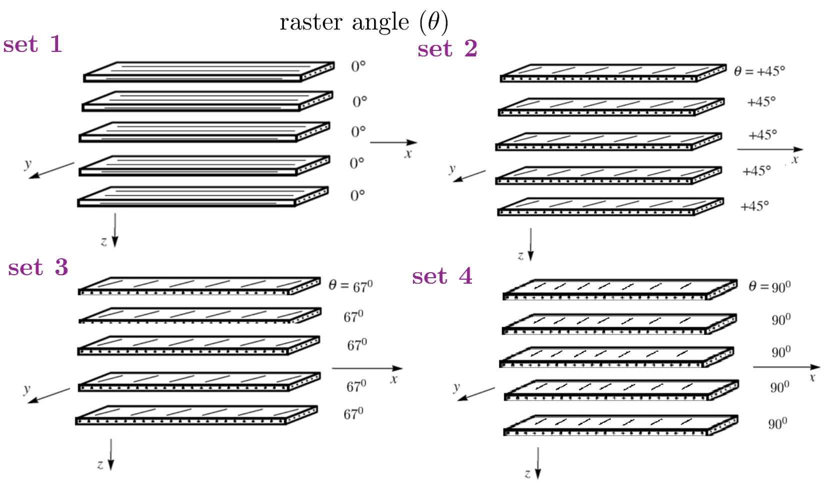

Figure 5.2: Layer wise Raster angles

The dogbone specimens were manufactured with three raster angles ($\theta = 0°, 45°, 90°$), a fixed layer height(h) of 0.3 mm, and a total thickness (t) of 2.1 mm . Dogbone specimen dimensions are taken as shown in Figure 4.1 as per ASTM D638-14. The tensile testing was performed using UTM at a loading rate of 5 mm/min for dogbone specimen. For the size effect test, DENT specimens were prepared with three raster angles ($\theta = 45°, 67°, 90°$), a fixed layer height (h) of 0.3 mm, and a total thickness

(t) of 1.5 mm. In accordance with Bažant's SEL the specimens were scaled in a ratio of 1:2:3:4. Schematics of DENT specimens with layer wise raster angels are shown in Figure 5.1 and Figure 5.2.

5.2 Tensile test results

The tensile test were conducted on UTM and experimental σ-(ϵ) curves plotted and shown in Figure 5.4. Dogbone specimens after testing are shown in Figure 5.3. The fracture tests were conducted on the same UTM setup. Figure 5.5a, Figure 5.5b and Figure 5.6a show DENT specimens after tensile testing for $\theta = 0°, 45°, 90°$, respectively. Corresponding $P - \Delta$ diagram of DENT specimens are shown in Figure 5.6b, Figure 5.7a and Figure 5.7b. Form the results, it can be seen that D_L for all specimens was below 0.15. This indicates quasi brittle behavior; although PC is naturally a ductile material, the FDM fabricated PC exhibits quasi brittle characteristics. SEL analysis is applicable to this geometry. The peak load (P_{max}) data obtained from the scaled specimens was analyzed using the regression method of the SEL. This analysis facilitated the calculation of the specific fracture energy (G_f) and the effective length of the fracture process zone (c_f) for each raster angle configuration. Furthermore, the experimental data was used to derive the TSC to describe the post peak softening behavior of the PC FDM parts. Same MATLAB code is with mentioned in Appendix B was used to do size effect analysis of PC DENT specimens with E_1,E_2 and E_{45} derived from dogbone tensile test.

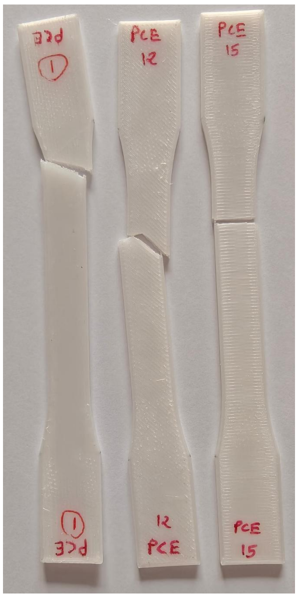

Figure 5.3: Tensile tested PC specimens with $\theta = 0°, 45°, 90°$

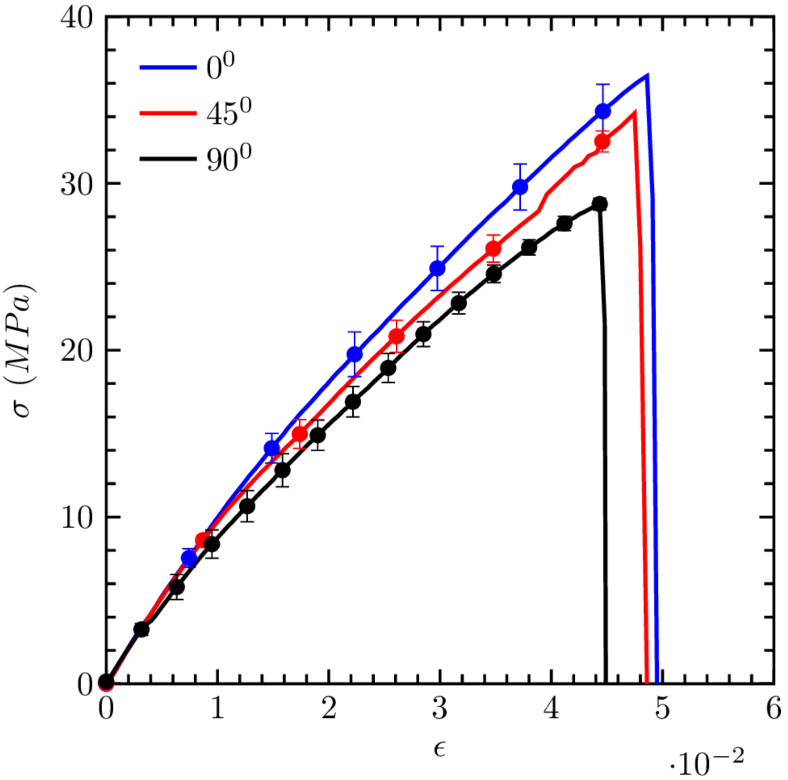

Figure 5.4: Stress - Strain Curve for PC with $h = 0.3$ mm

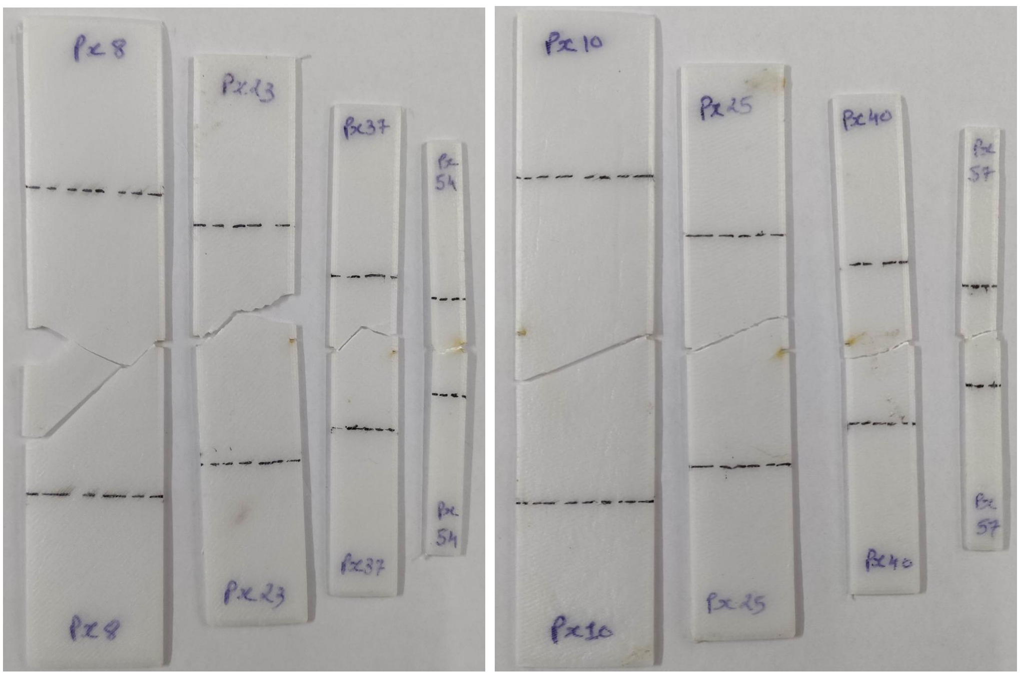

(a) $\theta = 45°$

(b) $\theta = 67°$

Figure 5.5: DENT specimens after tensile testing (a) $\theta = 45°$ (b)$\theta = 67°$

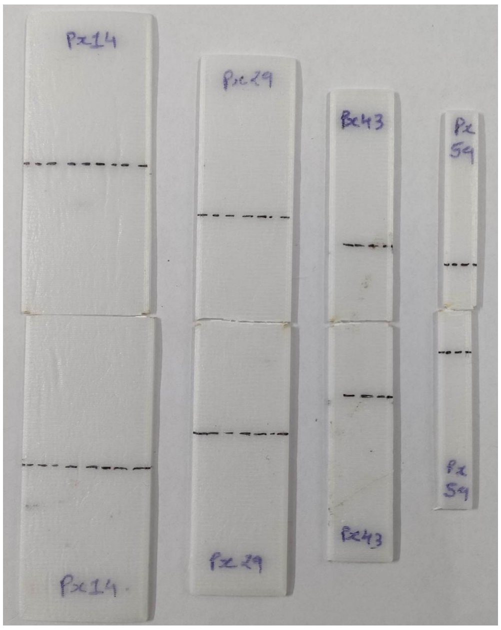

(a) $\theta = 90°$

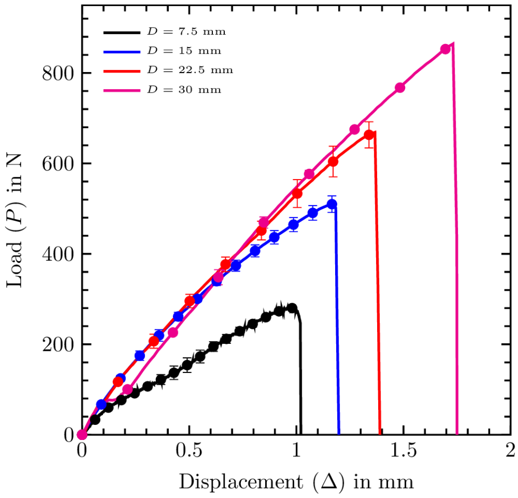

(b) $\theta = 45°$

Figure 5.6: (a)DENT specimens after tensile testing $\theta = 90°$ (b)$P - \Delta$ diagram of DENT specimens

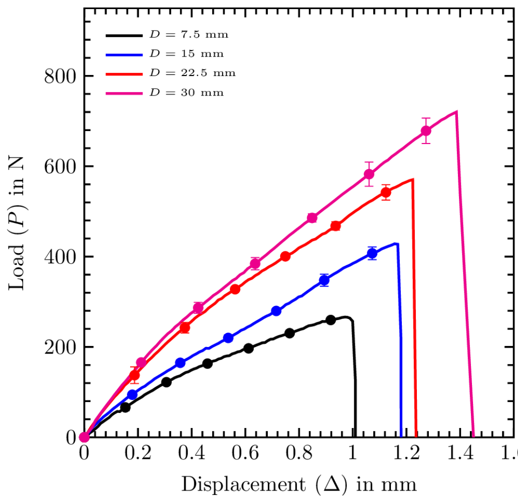

(a) $\theta = 67°$

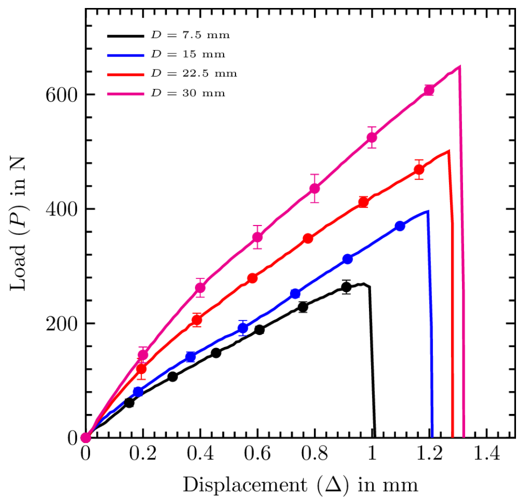

(b) $\theta = 90°$

Figure 5.7: (b)$P - \Delta$ diagram of DENT specimens

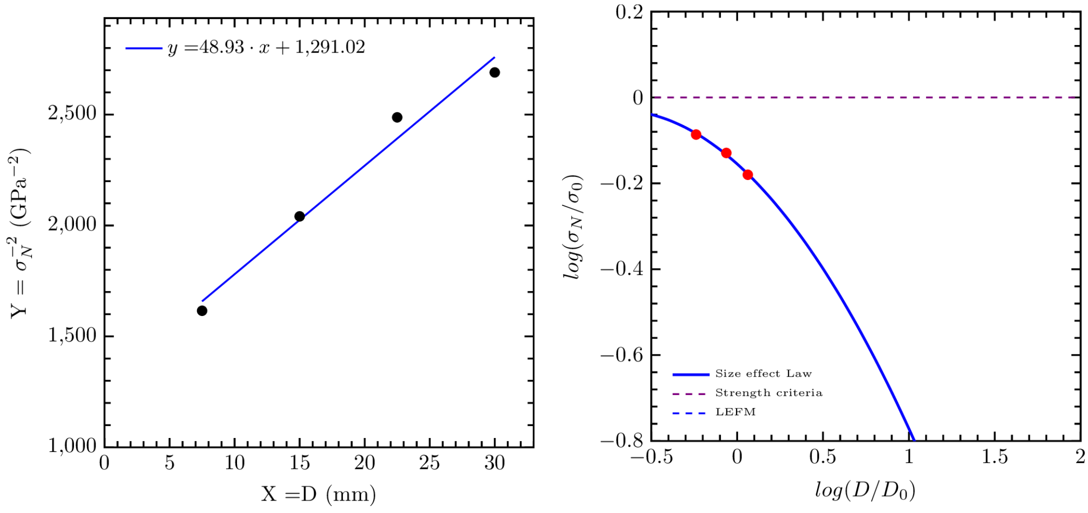

(a) (b)

Figure 5.8: PC DENT specimens ($\theta = 45°$): (a) Regression analysis for size effect parameters; (b)Derived SEL

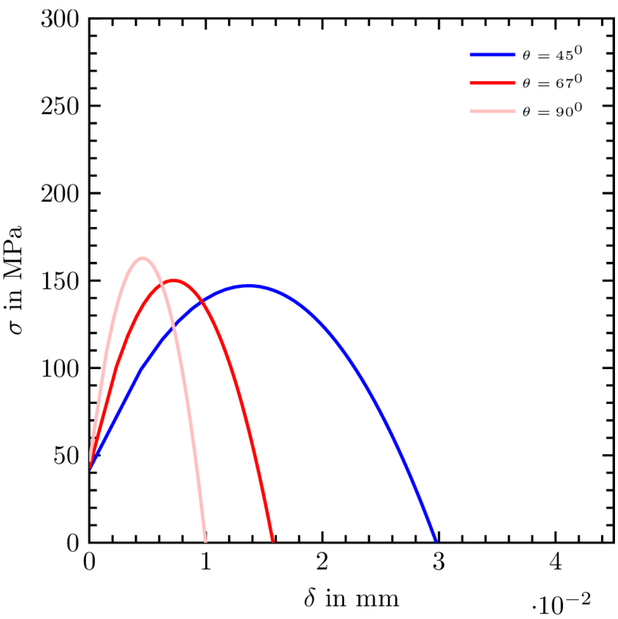

Figure 5.9: Traction-separation Curve for PC

The regression analysis curve and SEL are shown in Figure 5.8a and Figure 5.8b for $\theta = 45°$.As observed in Table 5.1, FDM manufactured PC specimens observes size effect and its parameters are mentioned in table 5.1. From Table 5.2 observes that both the fracture energy (G_f) and the FPZ length (c_f) exhibit a downward trend as rater angel θ increases. The TSC was also derived from SEL for the PC DENT

Table 5.1: Summary of Extracted Size Effect Parameters for PC DENT Specimens

θ	D_0 (mm)	σ_0 (MPa)	Derived Size Effect Law
45°	26.39	27.82	$\sigma_N = 27.82(1+\beta)^{-\frac{1}{2}}$
67°	13	28.1	$\sigma_N = 28.1(1+\beta)^{-\frac{1}{2}}$
90°	7.6	30.01	$\sigma_N = 30.01(1+\beta)^{-\frac{1}{2}}$

Table 5.2: Comparison of G_f values for PC DENT specimens derived via SEL and TSC

θ	G_f by SEL (kJ/m^2)	c_f in mm	G_f by TSC (kJ/m^2)
45°	3.06	1.64	3.45
67°	1.66	0.81	1.79
90°	1.13	0.47	1.19

specimens and is shown in Figure 5.9. The area under this curve, representing G_f, is presented in Table 5.2, and the values agree with the SEL derived value.

Chapter 6

EWF Analysis of FDM Specimens Fabricated from Polycarbonate

In this chapter, an Essential Work of Fracture (EWF) analysis was conducted on Polycarbonate (PC) laminates fabricated by FDM. The PC laminates exhibited ductile behavior when at least one lamina possessed a raster angle of $0°$. Due to this , the standard SEL law is inapplicable. Consequently, the EWF approach specifically tailored for ductile materials was employed. To facilitate this analysis, precracked DENT specimens were fabricated from PC filaments using the FDM process, as per adhering to EWF testing requirements.

6.1 Materials and Experimental Methods

EWF specimens with total thickness t 1.2 mm were fabricated using the FDM process. The manufacturing utilized the same process parameters previously detailed in Section 5.1. The PC laminates were printed with a raster angel sequence of $[0/45/90/-45]$. Post fabrication, notches were generated using a laser to create the necessary variations in ligament length. Schematics illustrating the PC specimens with varying ligament lengths are presented in Figure 6.1. Based on these dimensions, FDM PC specimens were fabricated with a layer height of $h = 0.3$ mm and a total thickness of $t = 1.2$ mm. The raster angle for each layer is shown in Figure 6.2. Figure 6.3 shows the FDM specimens after the notches were created using a laser.

6.2 EWF theory

The theoretical framework for the Essential Work of Fracture (EWF) method is grounded in Broberg's unified theory of fracture [59, 60, 61]. According to this theory, stable crack propagation is driven by energy input into an inner FPZ, which

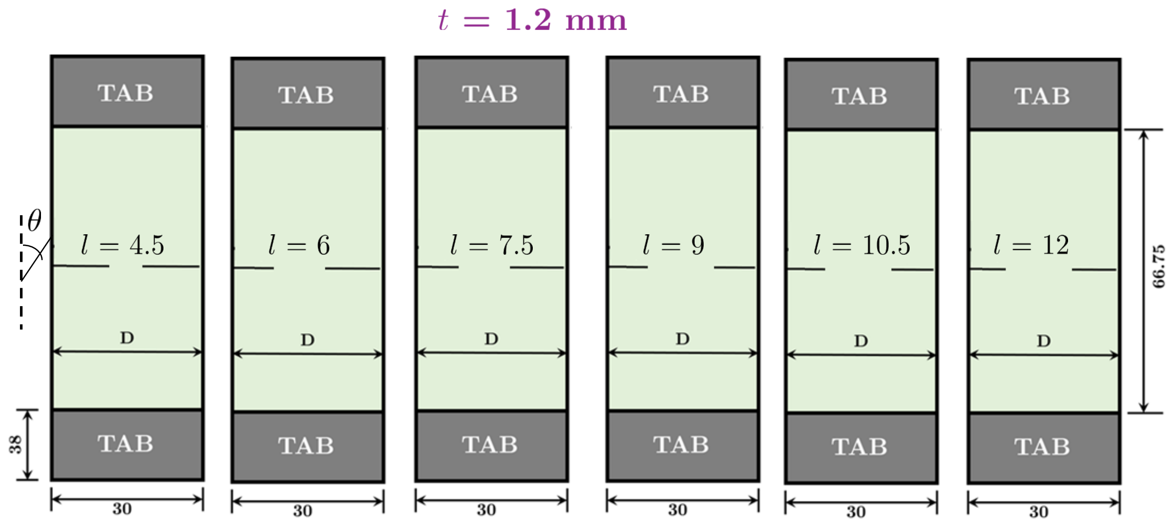

Figure 6.1: Schematic of DENT specimens for EWF (Dimensions are in mm)

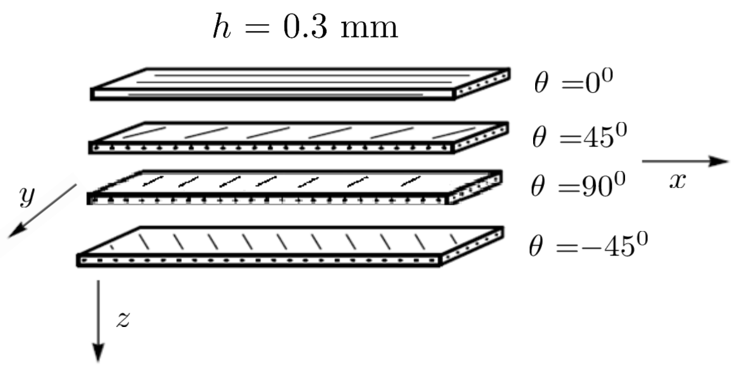

Figure 6.2: Layer wise raster angle (θ)

is screened by dissipative work occurring in the surrounding material. Consequently, the total energy required for fracture is the sum of the dissipative work in the outer plastic zone and the essential work performed within the inner FPZ. The essential work is considered a fundamental material property (toughness), whereas the non-essential or plastic work is a geometry dependent parameter. The EWF technique was formally developed for plane stress ductile fracture by Cotterell and Reddel [59, 62]. Through experiments on different ligament DENT specimens in Mode-I, they demonstrated that the energy dissipated at the crack tip is constant for a given specimen thickness. The total work of fracture (W_f) is calculated by integrating the load displacement curve shown in Figure 6.4. This total energy is theoretically split into two primary components:

1. The essential work of fracture (W_e), consumed in the FPZ to generate new

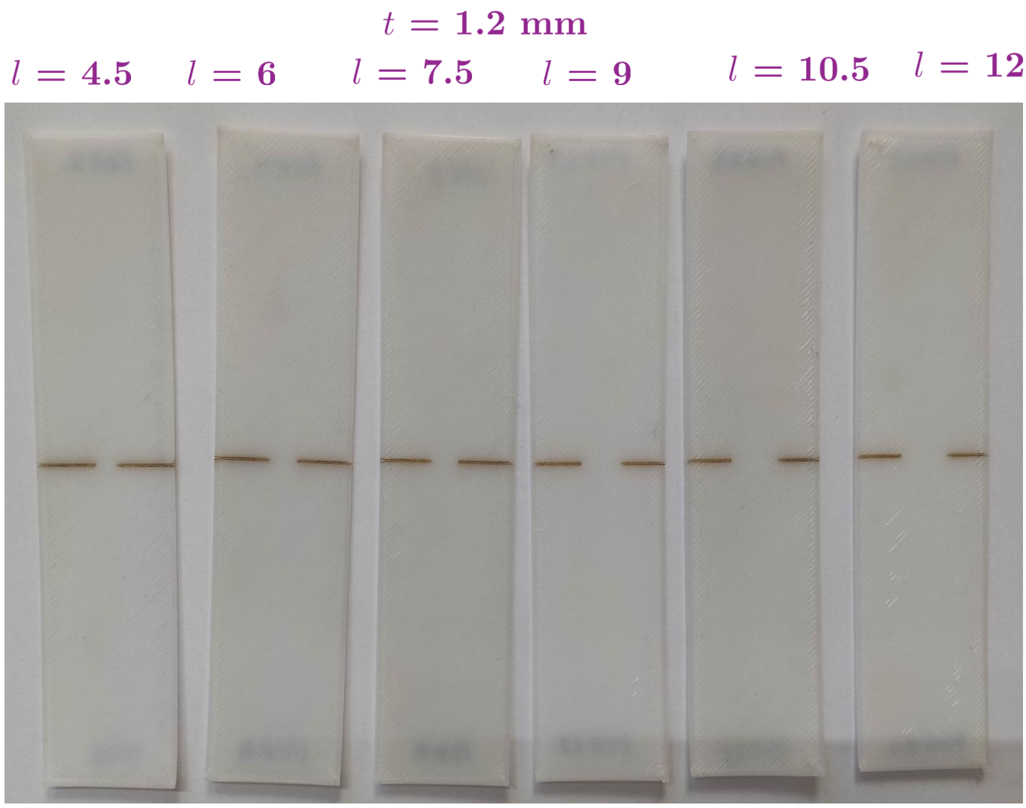

Figure 6.3: FDM fabricated PC DENT specimens

surfaces.

2. The non essential plastic work (W_p), dissipated in the outer plastic deformation zone.

This relationship is expressed in Eq. 6.1:

$$W_f = W_e + W_p \tag{6.1}$$

Assuming the ligament is fully yielded and the plastic zone is confined within the ligament of the specimen, Eq. 6.1 can be expanded. The essential work scales with the ligament cross sectional area (lt), while the plastic work scales with the volume of the plastic zone ($\propto l^2 t$). This leads to Eq. 6.2:

$$W_f = w_e l t + \beta w_p l^2 t \tag{6.2}$$

where l represents the ligament length, t is the specimen thickness, w_e is the specific essential work of fracture (surface energy), w_p is the specific non essential work of fracture, and β is a shape factor related to the geometry of the outer plastic dissipation zone.

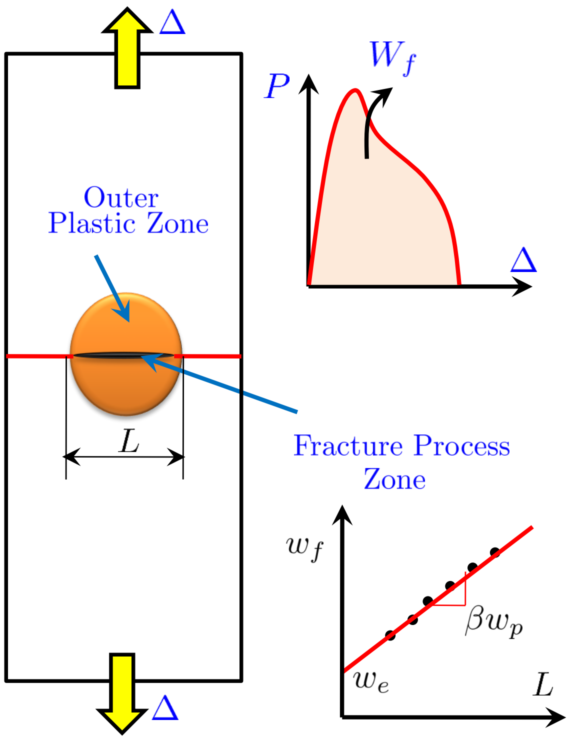

Figure 6.4: Schematic diagram for EWF geometry with FPZ

Dividing Eq. 6.2 by the cross sectional area (lt) yields the specific total work of fracture (w_f), as shown in Eq. 6.3:

$$w_f = w_e + \beta w_p l \tag{6.3}$$

Equation 6.3 forms the basis for the data reduction method. By testing specimens with varying ligament lengths and plotting the specific work of fracture (w_f) against the ligament length (l), a linear regression can be performed. The intercept of this line at $l = 0$ provides the specific essential work of fracture (w_e), while the slope yields the non essential plastic work term (βw_p).

6.3 Experimental results

Tensile testing of all FDM fabricated PC DENT specimens was performed on a UTM with a loading rate of 1 mm/min. Figure 6.5a shows the gripping of the UTM, and Figure 6.5b shows a close up view near the crack. Figure 6.6 shows the DENT specimens after tensile testing for different ligament lengths (l). The corresponding $P - \Delta$ curves for varying ligament lengths are shown in Figure 6.7. From Figure 6.7, it can be seen that the specimens exhibit $D_L > 0.85$, confirming that ductile behavior is observed. Additionally, the $P - \Delta$ curves are self similar for different l. This behavior is attributed to the fact that one of the laminae has a raster angle of $\theta = 0°$. Therefore, using the EWF approach, w_e can be derived from the intercept of the linear regression at zero ligament length. This w_e is termed the fracture energy for that laminate.

(a) (b)

Figure 6.5: (a) DENT specimen gripped on UTM (b) Closed view near FPZ

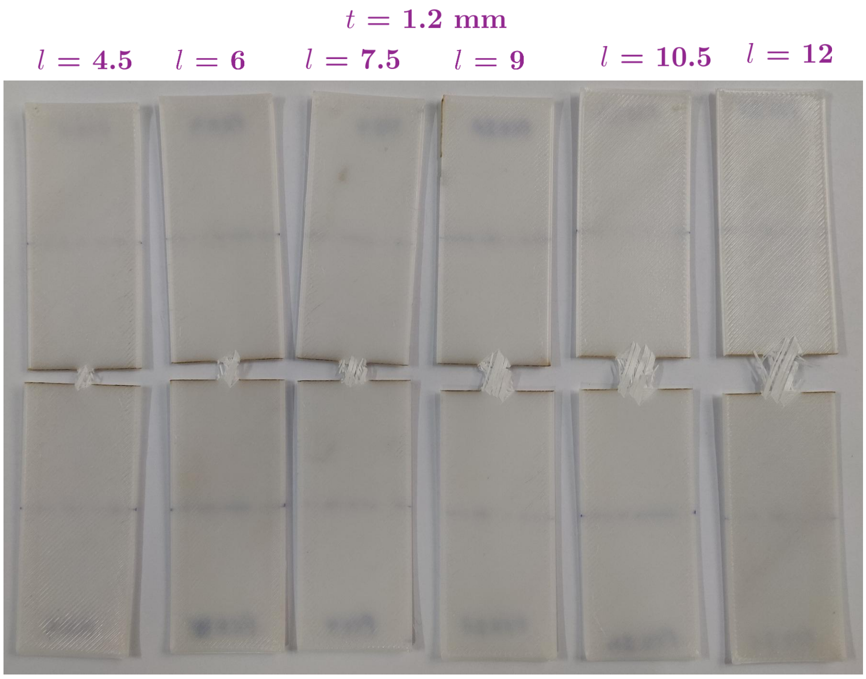

Figure 6.6: DENT specimens after tensile testing for EWF

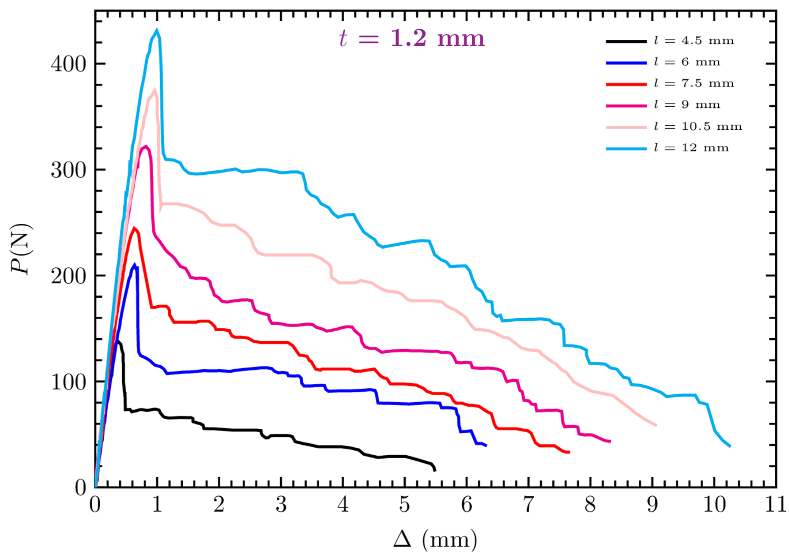

Figure 6.7: $P - \Delta$ curves for DENT specimens with varying l

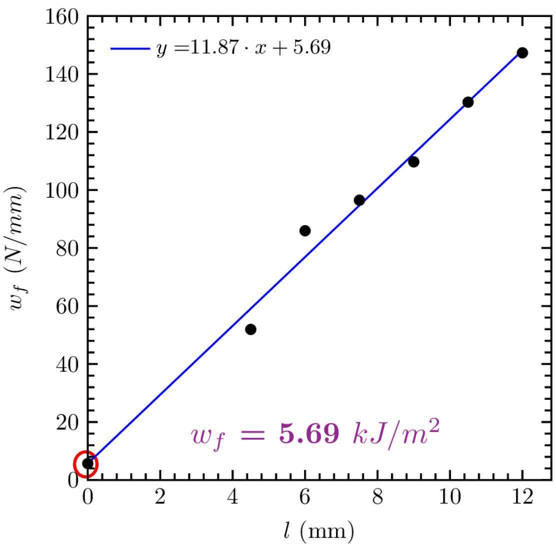

Figure 6.8: Linear regression for w_f

To derive the specific essential work of fracture (w_e) for PC, the area under the $P - \Delta$ curve for each DENT specimen in Figure 6.7 was measured to obtain the total work of fracture. This value was then divided by the thickness (t) and ligament length (l) to calculate w_f. By plotting the specific work of fracture (w_f) against the ligament length (l)(see Figure 6.8), a linear regression was performed. The intercept of this line at $l = 0$ yields w_e, which represents the fracture energy of the laminate. In this case, a value of $w_e = 5.69\ kJ/m^2$ was obtained.

Chapter 7

Conclusions and Future Scope

7.1 Conclusions

In this research work, FDM fabricated specimens with filaments of CPLA and PC have been analyzed. ASTM standard dog-bone specimens were prepared using the FDM process, and the Elastic Modulus in E_1 and E_2 was measured for the laminate material. These mechanical properties were used to derive Fracture Energy G_f using SEL if the material failed in a quasi brittle manner. SENT and DENT specimens were fabricated, fractured on a UTM, and the recorded data were analyzed. The effect of thickness for CPLA and the effect of raster angle for PC specimens were discussed. From SEL, the TSC was also derived and used in FE simulation to compare with experimental results for CPLA specimens. If the material exhibited ductile behavior, then the EWF approach was used and discussed.

- Tests performed on CPLA laminates manufactured via FDM confirm that nominal strength (σ_N) is dependent on the specimen size. When applied to the SEL, the data for identical notched specimens demonstrates a clear trend: smaller specimens exhibit ductility, while larger structures follow LEFM. This transition, visible on a logarithmic scale, confirms that the CPLA parts exhibit quasi brittle behavior.

- SENT and DENT specimens with CPLA filaments using FDM process were manufactured, SEL for both specimens derived and it shows that SEL depends on specimen geometry and thickness also. It also shows that as structure size D increases, σ_N decreases. Their logarithmic plot shows a transition from ductile to LEFM behavior for CPLA material.

- The SEL method can be used to calculate fracture parameters such as FPZ length and G_f. The results of the study showed that the fracture energy of SENT and DENT geometry depends on thickness. The fracture energy decreases with increasing thickness.

- The R curve and length of the FPZ can also be determined from these characteristics. The specimen thickness affects the R curve's shape as well. The length of the FPZ also increases with decreases in thickness.

- The TSC was also derived for both geometries and for all thicknesses. It was observed that though the size and shape of the TSC were different but the cohesive energy which is the area under the TSC was similar and hence, it should be treated as a material properties.

- The fracture energy was numerically verified to check applicability of SEL. TSC was derived from SEL, and a numerical analysis was done using cohesive zone modeling technique. Good agreement was found between the fracture energy values derived by SEL and TSC.

- The experimentally derived cohesive law using SEL (for each thickness) is used for the FE simulations using Abaqus software. Same cohesive model is used for other ligament length of same thickness and same specimen type to measure response of model and it shows good agreement with experimental results.

- Ductility level (D_L)is important parameter to look before applying crack characterization method. D_L should be less than 0.15 for implementation of SEL.

- PC FDM fabricated material shows the size effect law(SEL)for raster angle greater than 45^0 and which depends on raster angle of specimen. Fracture energy decreases G_f as raster angle θ of PC material raster angle (θ) increases

- PC FDM printed laminate material behavior with one of the lamina with raster angle 0^0 observes the ductile behavior. as D_L value is grater than 0.15. EWF approach can be applied for evaluating fracture energy.

7.2 Future Scope

- In the present work, the FDM process was used to fabricate specimens. Future studies could extend this research by utilizing other Additive Manufacturing (AM) techniques, such as Stereolithography (SLA) or Selective Laser Sintering (SLS), to compare fracture performance across different manufacturing modalities.

- This study focused on specific filaments; however, other common FDM materials like ABS, PETG, and HIPS could be investigated. Fabricating and analyzing specimens from these materials would provide a broader understanding of fracture mechanics in 3D printed polymers.

- Numerical simulations and FE analysis should be extended to these additional materials. This would help in predicting their failure mechanisms and validating experimental behavior under various loading conditions.

- Further experiments should be conducted to evaluate the influence of various FDM process parameters—such as layer height, nozzle temperature, and print speed—on the Size Effect Law (SEL) applicability and the specific fracture energy (G_f).

- A detailed analysis of the FPZ in FDM printed materials should be performed.

Appendix A: Matlab Code

Below is the MATLAB script used for the calculation of laminate stiffness matrices and effective properties.

```
clear all;
clc;
close all;

%% 1. Laminate Geometry Setup
% Total thickness of the composite specimen
lam_thk = input('Enter the thickness of specimen = ');
% Count of plies/layers
n_layers = input('Enter number of layers in specimen = ');
% Calculated thickness per individual layer
ply_h = lam_thk / n_layers;

%% 2. Layer Orientation Input
% Input vector for angles (e.g., [30 -45 0 -45 30])
theta_vec = input('Enter the orientation vector of specimen = ');

%% 3. Material Properties Input
Mod_L = input('Enter Long. Young modulus (E1) [MPa] = ');
Mod_T = input('Enter Trans. Young modulus (E2) [MPa] = ');
PR_LT = input('Enter Major Poisson ratio (v12) = ');
% Calculate Minor Poisson ratio
PR_TL = PR_LT * Mod_T / Mod_L;
Shear_LT = input('Enter In-plane Shear modulus (G12) [MPa] = ');

%% 4. Compute Reduced Stiffness Matrix (Q)
% Denominator term for stiffness calculation
denom = (1 - PR_LT * PR_TL);

Stiff_11 = Mod_L / denom;
Stiff_22 = Mod_T / denom;
Stiff_12 = (PR_TL * Mod_L) / denom;
Stiff_66 = Shear_LT;

% Transformed Reduced Stiffness Calculation (Q_bar)
```

```
% Pre-calculating trig functions for cleaner code
c_t = cosd(theta_vec);
s_t = sind(theta_vec);

Bar_Q11 = Stiff_11.*(c_t).^4 + Stiff_22.*(s_t).^4 + 2.*(Stiff_12
 + 2.*Stiff_66).*(s_t).^2.*(c_t).^2;
Bar_Q12 = (Stiff_11 + Stiff_22 - 4.*Stiff_66).*(s_t).^2.*(c_t).^2
  + Stiff_12.*((c_t).^4 + (s_t).^4);
Bar_Q22 = Stiff_11.*(s_t).^4 + Stiff_22.*(c_t).^4 + 2.*(Stiff_12
 + 2.*Stiff_66).*(s_t).^2.*(c_t).^2;
Bar_Q16 = (Stiff_11 - Stiff_12 - 2.*Stiff_66).*(c_t).^3.*s_t - (
 Stiff_22 - Stiff_12 - 2.*Stiff_66).*c_t.*(s_t).^3;
Bar_Q26 = (Stiff_11 - Stiff_12 - 2.*Stiff_66).*(s_t).^3.*c_t - (
 Stiff_22 - Stiff_12 - 2.*Stiff_66).*s_t.*(c_t).^3;
Bar_Q66 = (Stiff_11 + Stiff_22 - 2.*Stiff_12 - 2.*Stiff_66).*(s_t
 ).^2.*(c_t).^2 + Stiff_66.*((c_t).^4 + (s_t).^4);

% Storage for loop
for i = 1:n_layers
Q_Mat_Global(:,:,i) = [Bar_Q11(i) Bar_Q12(i) Bar_Q16(i);
Bar_Q12(i) Bar_Q22(i) Bar_Q26(i);
Bar_Q16(i) Bar_Q26(i) Bar_Q66(i)];
end

% Z-coordinate locations of plies
z_loc = (-n_layers/2 : n_layers/2) * ply_h;

%% 5. Calculation of Extensional Stiffness Matrix [A]
Ex_Stiff_11 = 0; Ex_Stiff_12 = 0; Ex_Stiff_22 = 0;
Ex_Stiff_16 = 0; Ex_Stiff_26 = 0; Ex_Stiff_66 = 0;

for k = 1:n_layers
dz = z_loc(k+1) - z_loc(k);
Ex_Stiff_11 = Ex_Stiff_11 + Bar_Q11(k) * dz;
Ex_Stiff_12 = Ex_Stiff_12 + Bar_Q12(k) * dz;
Ex_Stiff_22 = Ex_Stiff_22 + Bar_Q22(k) * dz;
Ex_Stiff_16 = Ex_Stiff_16 + Bar_Q16(k) * dz;
Ex_Stiff_26 = Ex_Stiff_26 + Bar_Q26(k) * dz;
Ex_Stiff_66 = Ex_Stiff_66 + Bar_Q66(k) * dz;
end

%% 6. Calculation of Coupling Stiffness Matrix [B]
Coup_Stiff_11 = 0; Coup_Stiff_12 = 0; Coup_Stiff_22 = 0;
Coup_Stiff_16 = 0; Coup_Stiff_26 = 0; Coup_Stiff_66 = 0;

for k = 1:n_layers
```

```
dz_sq = (z_loc(k+1))^2 - (z_loc(k))^2;
Coup_Stiff_11 = Coup_Stiff_11 + Bar_Q11(k) * dz_sq;
Coup_Stiff_12 = Coup_Stiff_12 + Bar_Q12(k) * dz_sq;
Coup_Stiff_22 = Coup_Stiff_22 + Bar_Q22(k) * dz_sq;
Coup_Stiff_16 = Coup_Stiff_16 + Bar_Q16(k) * dz_sq;
Coup_Stiff_26 = Coup_Stiff_26 + Bar_Q26(k) * dz_sq;
Coup_Stiff_66 = Coup_Stiff_66 + Bar_Q66(k) * dz_sq;
end

% Factor of 1/2 for B Matrix
Coup_Stiff_11 = 0.5 * Coup_Stiff_11;
Coup_Stiff_12 = 0.5 * Coup_Stiff_12;
Coup_Stiff_22 = 0.5 * Coup_Stiff_22;
Coup_Stiff_16 = 0.5 * Coup_Stiff_16;
Coup_Stiff_26 = 0.5 * Coup_Stiff_26;
Coup_Stiff_66 = 0.5 * Coup_Stiff_66;

%% 7. Calculation of Bending Stiffness Matrix [D]
Bend_Stiff_11 = 0; Bend_Stiff_12 = 0; Bend_Stiff_22 = 0;
Bend_Stiff_16 = 0; Bend_Stiff_26 = 0; Bend_Stiff_66 = 0;

for k = 1:n_layers
dz_cub = (z_loc(k+1))^3 - (z_loc(k))^3;
Bend_Stiff_11 = Bend_Stiff_11 + Bar_Q11(k) * dz_cub;
Bend_Stiff_12 = Bend_Stiff_12 + Bar_Q12(k) * dz_cub;
Bend_Stiff_22 = Bend_Stiff_22 + Bar_Q22(k) * dz_cub;
Bend_Stiff_16 = Bend_Stiff_16 + Bar_Q16(k) * dz_cub;
Bend_Stiff_26 = Bend_Stiff_26 + Bar_Q26(k) * dz_cub;
Bend_Stiff_66 = Bend_Stiff_66 + Bar_Q66(k) * dz_cub;
end

% Factor of 1/3 for D Matrix
Bend_Stiff_11 = (1/3) * Bend_Stiff_11;
Bend_Stiff_12 = (1/3) * Bend_Stiff_12;
Bend_Stiff_22 = (1/3) * Bend_Stiff_22;
Bend_Stiff_16 = (1/3) * Bend_Stiff_16;
Bend_Stiff_26 = (1/3) * Bend_Stiff_26;
Bend_Stiff_66 = (1/3) * Bend_Stiff_66;

%% 8. Assembly of ABD Matrix
Mat_A = [Ex_Stiff_11 Ex_Stiff_12 Ex_Stiff_16; Ex_Stiff_12
 Ex_Stiff_22 Ex_Stiff_26; Ex_Stiff_16 Ex_Stiff_26 Ex_Stiff_66];
Mat_B = [Coup_Stiff_11 Coup_Stiff_12 Coup_Stiff_16; Coup_Stiff_12
  Coup_Stiff_22 Coup_Stiff_26; Coup_Stiff_16 Coup_Stiff_26
 Coup_Stiff_66];
Mat_D = [Bend_Stiff_11 Bend_Stiff_12 Bend_Stiff_16; Bend_Stiff_12
```

```
    Bend_Stiff_22 Bend_Stiff_26; Bend_Stiff_16 Bend_Stiff_26
   Bend_Stiff_66];

ABD_Global = [Mat_A Mat_B; Mat_B Mat_D];
Inv_ABD = inv(ABD_Global);

%% 9. Semi-Inverse Approach and Effective Properties
inv_A = inv(Mat_A);
star_C = Mat_B * inv_A;
star_D = Mat_D - Mat_B * inv_A * Mat_B;
star_B = -inv_A * Mat_B;


delta_A = inv_A - star_B * inv(star_D) * star_C;
delta_B = star_B * inv(star_D);
delta_D = inv(star_D);

% Normalizing by thickness
norm_A = lam_thk * delta_A;

% Final Material Properties Output

Eff_Gxy = 1 / norm_A(3,3)
Eff_NUxy = -(norm_A(1,2) / norm_A(1,1))
Eff_Ey = 1 / norm_A(2,2)
Eff_Ex = 1 / norm_A(1,1)
```

Listing A.1: MATLAB script for Effective Property calculation

Appendix B: MATLAB Code for Fracture Energy and TSC

The following MATLAB script performs the calculation of the Fracture energy, TSC and conducts R-curve analysis for fracture mechanics.

```
clear all;
clc;
close all;

%% 1. Laminate Geometry
% thickness of laminate
thickness = input('Enter the thickness of specimen = ');
% number of layers
N = 6;
% thickness of each layer
h = thickness/N;

%% 2. Orientation of Layers
% Stacking sequence
t = [45 -45 0 0 -45 45];

%% 3. Laminate Properties
E1 = 1980;    % Longitudinal Modulus (MPa)
E2 = 980;     % Transverse Modulus (MPa)
nu12 = 0.36; % Major Poisson's ratio

nu21 = nu12*E2/E1;
G12 = 699;    % Shear Modulus (MPa)

%% 4. Compute Reduced Stiffness (Q) and Transformed (Q_bar)
Q12 = nu21*E1/(1-nu12*nu21);
Q22 = E2/(1-nu12*nu21);
Q11 = E1/(1-nu12*nu21);


Q66 = G12;

```

```
% Calculation of Transformed Reduced Stiffness

bQ12 = (Q11+Q22-4.*Q66).*(sind(t)).^2.*(cosd(t)).^2 + Q12.*((cosd
  (t)).^4 + (sind(t)).^4);
bQ11 = Q11.*(cosd(t)).^4 + Q22.*(sind(t)).^4 + 2.*(Q12+2.*Q66).*(
  sind(t)).^2.*(cosd(t)).^2;
bQ22 = Q11.*(sind(t)).^4 + Q22.*(cosd(t)).^4 + 2.*(Q12+2.*Q66).*(
  sind(t)).^2.*(cosd(t)).^2;
bQ26 = (Q11-Q12-2.*Q66).*(sind(t)).^3.*cosd(t) - (Q22-Q12-2.*Q66)
  .*sind(t).*(cosd(t)).^3;
bQ66 = (Q11+Q22-2.*Q12-2.*Q66).*(sind(t)).^2.*(cosd(t)).^2 + Q66
  .*((cosd(t)).^4 + (sind(t)).^4);
bQ16 = (Q11-Q12-2.*Q66).*(cosd(t)).^3.*sind(t) - (Q22-Q12-2.*Q66)
  .*cosd(t).*(sind(t)).^3;


for i = 1:N
bQ_Mat(:,:,i) = [bQ11(i) bQ12(i) bQ16(i);
bQ12(i) bQ22(i) bQ26(i);
bQ16(i) bQ26(i) bQ66(i)];
end

z = (-N/2:N/2)*h;

%% 5. Calculation of P Matrix (Formerly A Matrix)
P11 = 0; P12 = 0; P22 = 0;
P16 = 0; P26 = 0; P66 = 0;

for k = 1:N
dz = z(k+1)-z(k);
P11 = P11 + bQ11(k)*dz;
P12 = P12 + bQ12(k)*dz;
P22 = P22 + bQ22(k)*dz;
P16 = P16 + bQ16(k)*dz;
P26 = P26 + bQ26(k)*dz;
P66 = P66 + bQ66(k)*dz;
end

%% 6. Calculation of H Matrix (Formerly B Matrix)
H11 = 0; H12 = 0; H22 = 0;
H16 = 0; H26 = 0; H66 = 0;

for k = 1:N
diff_sq = (z(k+1))^2 - (z(k))^2;
H11 = H11 + bQ11(k)*diff_sq;
H12 = H12 + bQ12(k)*diff_sq;
```

```
H22 = H22 + bQ22(k)*diff_sq;
H16 = H16 + bQ16(k)*diff_sq;
H26 = H26 + bQ26(k)*diff_sq;
H66 = H66 + bQ66(k)*diff_sq;
end

% Applying 0.5 factor
H11 = 0.5*H11; H12 = 0.5*H12; H22 = 0.5*H22;
H16 = 0.5*H16; H26 = 0.5*H26; H66 = 0.5*H66;

%% 7. Calculation of F Matrix (Formerly D Matrix)
F11 = 0; F12 = 0; F22 = 0;
F16 = 0; F26 = 0; F66 = 0;

for k = 1:N
diff_cub = (z(k+1))^3 - (z(k))^3;
F11 = F11 + bQ11(k)*diff_cub;
F12 = F12 + bQ12(k)*diff_cub;
F22 = F22 + bQ22(k)*diff_cub;
F16 = F16 + bQ16(k)*diff_cub;
F26 = F26 + bQ26(k)*diff_cub;
F66 = F66 + bQ66(k)*diff_cub;
end

% Applying 1/3 factor
F11 = (1/3)*F11; F12 = (1/3)*F12; F22 = (1/3)*F22;
F16 = (1/3)*F16; F26 = (1/3)*F26; F66 = (1/3)*F66;

%% 8. Assembly of PHF Matrix (Global Stiffness)
Mat_P = [P11 P12 P16; P12 P22 P26; P16 P26 P66];
Mat_H = [H11 H12 H16; H12 H22 H26; H16 H26 H66];
Mat_F = [F11 F12 F16; F12 F22 F26; F16 F26 F66];

Global_Stiff = [Mat_P Mat_H; Mat_H Mat_F];
Inv_Global = inv(Global_Stiff);

%% 9. Semi-Inverse and Material Properties
sP = inv(Mat_P);
sH = -inv(Mat_P)*Mat_H;
sC_star = Mat_H*inv(Mat_P);
sF = Mat_F - Mat_H*inv(Mat_P)*Mat_H;

dP = sP - sH*inv(sF)*sC_star;
dD = thickness*dP;

% Effective Modulus
```

```
Ex = 1/dD(1,1);

%% 10. Geometry Parameters and Fitting
% Calculate rho and lambda
rho     = (sqrt(E1*E2))/(2*G12)-sqrt(nu12*nu21);
Y       = (0.1*(rho-1)+1+0.002*(rho-1)^3-0.015*(rho-1)^2+)*((1+rho
  )/2)^(-0.25);
lambda = E2/E1;
E_final = Ex;

% Width values and stress
D_vals = [7.5 15 22.5 30];
sigmaN1 = input('Enter the value of sigmaN in MPa (ex.[40 50 60])
   = ');
sigmaN = sigmaN1/1000;

X_fit = D_vals;
Z_fit = (sigmaN).^(-2);
K_fit = polyfit(X_fit, Z_fit, 1);

A_param = K_fit(1);
C_param = K_fit(2);
sigma0 = C_param^(-0.5)*1000;
D0 = C_param/A_param;

%% 11. Specimen Selection and Fracture Calculation
fprintf('Enter 2 for DENT \n');
fprintf('Enter 1 for SENT \n');
fprintf('Enter 4 for Three Point Bend \n\n');
fprintf('Enter 3 for Center Crack \n');


x_sel = input('Select type of Specimen by entering 1/2/3/4 = ');
fprintf('\n');

switch x_sel
case 1
disp('You have selected SENT Specimen')
a0 = D_vals/5;
alpha0 = a0/D_vals;
N1 = input('Enter No. of interval required = ');
alpha = alpha0:(0.33249-alpha0)/N1:0.33249;

% Calculation of g(alpha)
term_poly = (10.55*(alpha.^2) - 0.231*alpha - 21.71.*(alpha.^3) +
   30.38*(alpha.^4) +1.122  );
```

```
g = Y^2* alpha . * pi * term_poly.^2;

% g1 is derivative of g
d_poly = (-0.231 + 21.1*alpha - 65.13.*alpha.^2 + 121.53*alpha.^3);
g1 = Y^2 * pi * (term_poly.^2 + 2*alpha .* term_poly .* d_poly);

cf = (g(1)/g1(1))*D0;

case 2
disp('You have selected DENT Specimen')
a0 = D_vals/16;
alpha0 = a0/D_vals;
N1 = input('Enter No. of interval required = ');
alpha = alpha0:(0.397671875-alpha0)/N1:0.397671875;

% Calculation of g(alpha) & g'(alpha)
cos_term = cos((pi*alpha)/2);
tan_term = tan((pi*alpha)/2);
g = 2*(tan_term).*(1+0.122*(cos_term).^4).^2;

% Derivative approximation logic for DENT
term_A = (1+0.122*(cos_term).^4);
term_B = (sec((pi*alpha)/2).^2);
term_C = (0.244*tan_term.*sin(pi*alpha).^2);
g1 = pi * term_A .* (term_A .* term_B - term_C);

cf = (g(1)/g1(1))*D0;

case 3
disp('You have selected Center Crack Test Specimen')
case 4
disp('You have selected Three Point Bend Test Specimen')
end

%% 12. R-Curve Calculation and Plotting
Gf = (((sigma0)^2)*D0*g(1))/E_final;
ccf = (g1(1)/g(1))*((g./g1)-alpha+alpha0);
c_inc = cf*(g1(1)/g(1))*((g./g1)-alpha+alpha0);

R1 = (g1/g1(1)).*(ccf);
R_val = Gf*(g1/g1(1)).*(ccf);

r_coord = 0:c_inc/N1:c_inc;
delta = sqrt(r_coord*Gf/(pi*E_final));
delta_1 = sort(delta,'descend');
```

```
I_poly = polyfit(delta_1, R_val, 3);
CK = I_poly(1)*3*(delta_1).^2 + I_poly(2)*2*(delta_1) + I_poly(3)
 ;

S_area = trapz(delta_1, CK);
fprintf('Area of traction curve = %f\n', S_area);

% Plotting results
figure(1); plot(ccf, R1); title('FPZ vs R/Gf');
figure(2); plot(r_coord, delta); title('Opening vs FPZ');
figure(3); plot(delta_1, R_val); title('Opening vs Energy');
figure(4); plot(delta_1, CK); title('Traction Separation Curve');
figure(5); plot(X_fit, Z_fit); title('Z vs X Fitting');
```

Listing B.1: MATLAB script for Fracture Energy nd TSC

Appendix C: Size Effect Analysis Curves

Linear Regression and size effect Curve

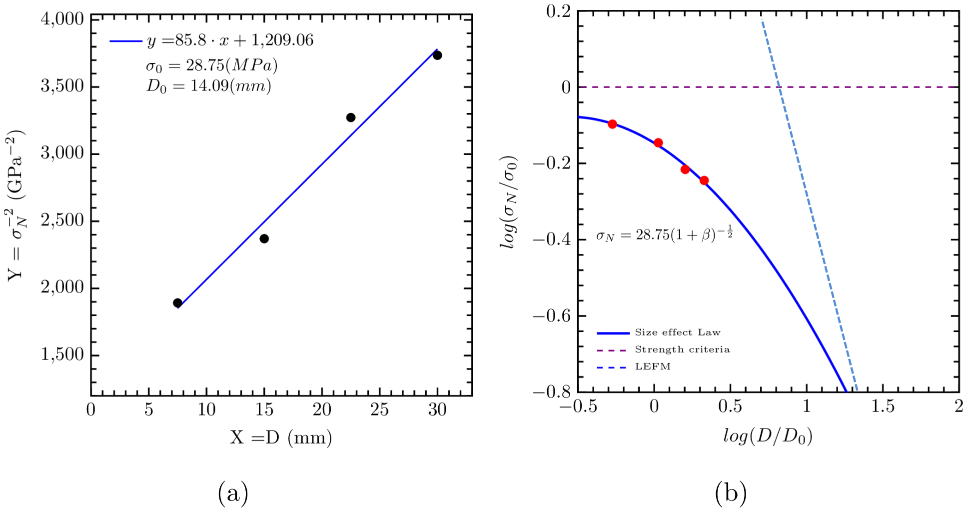

Figure C.1: SENT specimens (t = 1.4 mm): (a) Regression analysis for size effect parameters; (b) Obtained Size Effect Law

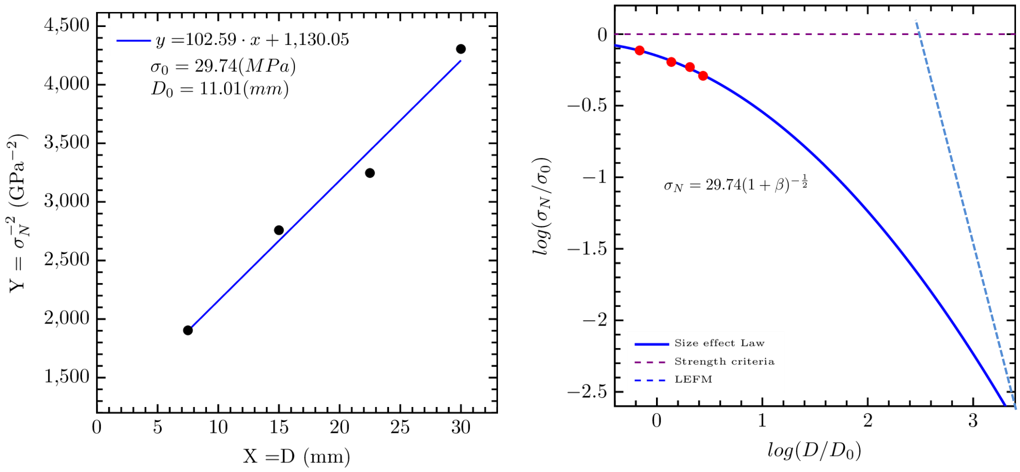

(a) (b)

Figure C.2: SENT specimens (t = 2.1 mm): (a) Regression analysis for size effect parameters; (b) Obtained Size Effect Law

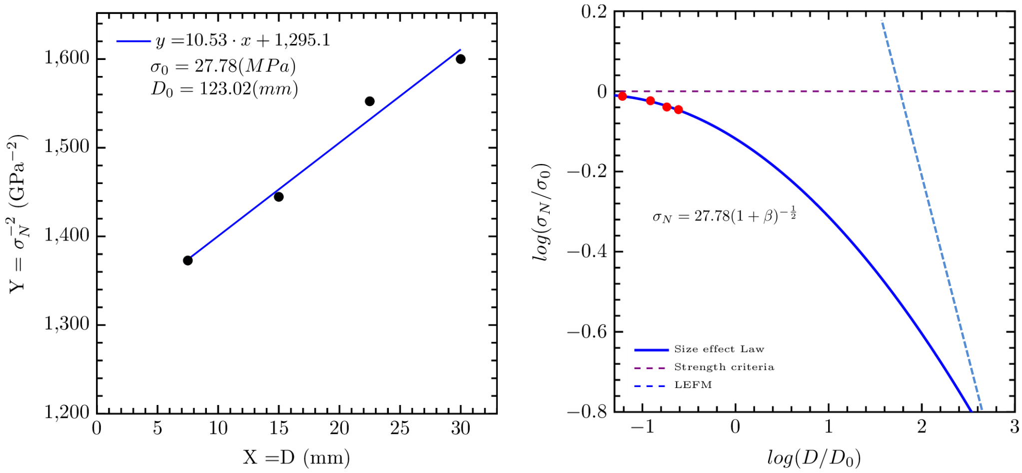

(a) (b)

Figure C.3: DENT specimens (t = 0.7 mm): (a) Regression analysis for size effect parameters; (b) Obtained Size Effect Law

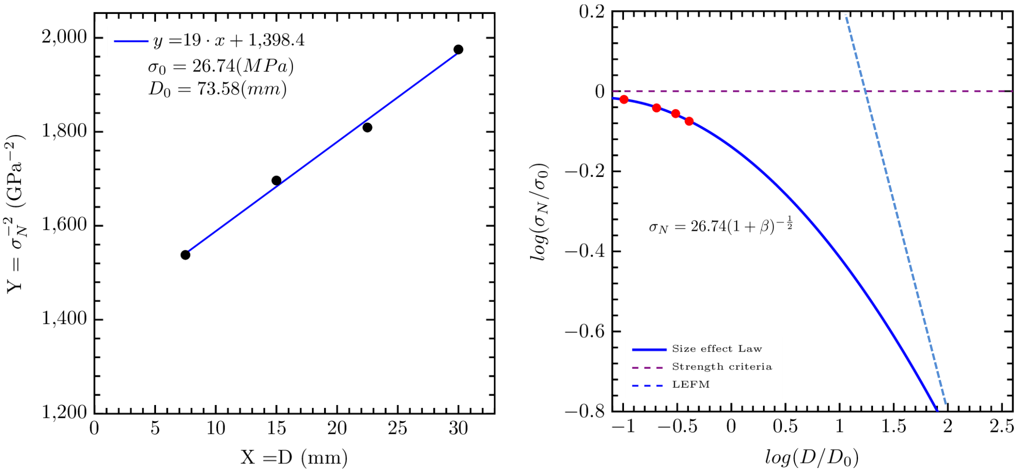

(a) (b)

Figure C.4: DENT specimens ($t = 1.4$ mm): (a) Regression analysis for size effect parameters; (b) Obtained Size Effect Law

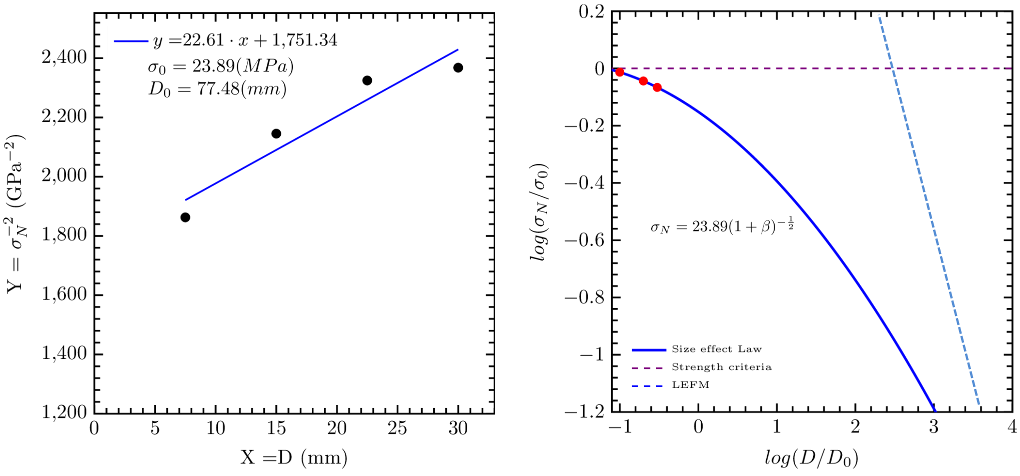

(a) (b)

Figure C.5: DENT specimens ($t = 2.1$ mm): (a) Regression analysis for size effect parameters; (b) Obtained Size Effect Law

References

[1] X. Wang, M. Jiang, Z. Zhou, J. Gou, and D. Hui, "3D printing of polymer matrix composites: A review and prospective," *Composites Part B: Engineering*, vol. 110, pp. 442–458, feb 2017.

[2] S. Raut, V. S. Jatti, N. K. Khedkar, and T. Singh, "Investigation of the Effect of Built Orientation on Mechanical Properties and Total Cost of FDM Parts," *Procedia Materials Science*, vol. 6, pp. 1625–1630, 2014.

[3] O. A. Mohamed, S. H. Masood, and J. L. Bhowmik, "Mathematical modeling and FDM process parameters optimization using response surface methodology based on Q-optimal design," *Applied Mathematical Modelling*, vol. 40, pp. 10052–10073, dec 2016.

[4] A. Garg and A. Bhattacharya, "An insight to the failure of FDM parts under tensile loading: finite element analysis and experimental study," *International Journal of Mechanical Sciences*, vol. 120, pp. 225–236, jan 2017.

[5] R. Zou, Y. Xia, S. Liu, P. Hu, W. Hou, Q. Hu, and C. Shan, "Isotropic and anisotropic elasticity and yielding of 3D printed material," *Composites Part B: Engineering*, vol. 99, pp. 506–513, aug 2016.

[6] W. Wu, W. Ye, Z. Wu, P. Geng, Y. Wang, and J. Zhao, "Influence of Layer Thickness, Raster Angle, Deformation Temperature and Recovery Temperature on the Shape-Memory Effect of 3D-Printed Polylactic Acid Samples," *Materials*, vol. 10, p. 970, aug 2017.

[7] A. Bagsik and D. Manufacturing, "Mechanical Properties of Fused Deposition Modeling Pards with Ultem* 9085," *In Proceedings of the 14th International Scientific Conference on Polymeric Materials*, vol. 15, pp. 307–315, 2011.

[8] F. Talagani, S. DorMohammadi, R. Dutton, C. Godines, H. Baid, F. Abdi, V. Kunc, B. Compton, S. Simunovic, C. Duty, L. Love, B. Post, and C. Blue, "Numerical simulation of big area additive manufacturing (3d printing) of a full size car," *Sampe Journal*, vol. 51, p. 27, 2015.

[9] P. A. Kobryn, N. R. Ontko, L. P. Perkins, and J. S. Tiley, "Additive Manufacturing of Aerospace Alloys for Aircraft Structures," 2006.

[10] L. E. Murr, "Frontiers of 3D Printing/Additive Manufacturing: from Human Organs to Aircraft Fabrication," 2016.

[11] R. Marudhappan and U. Chandrasekhar, "Additive manufacturing in india aerospace manufacturing and mro industry: Challenges and opportunities," *Journal of The Institution of Engineers (India): Series C*, vol. 103, pp. 1013–1030, 8 2022.

[12] S. Ji and M. Guvendiren, "Recent Advances in Bioink Design for 3D Bioprinting of Tissues and Organs," 2017.

[13] Z. P. Bazant, "Size Effect in Blunt Fracture: Concrete, Rock, Metal," *Journal of Engineering Mechanics*, vol. 110, pp. 518–535, apr 1984.

[14] D. S. Dugdale, "Yielding of steel sheets containing slits.," *Journal of the Mechanics and Physics of Solids*, vol. 8, pp. 100–104, 1960.

[15] B. G.I., "The formation of equilibrium cracks during brittle fracture.General ideas and hypothesis. Axisymmetrical cracks.," *Journal of Applied Mathematics and Mechanics*, vol. 23, pp. 622–636, 1959.

[16] H. Li and N. Chandra, "Analysis of crack growth and crack-tip plasticity in ductile materials using cohesive zone models.," *International Journal of Plasticity*, vol. 19, pp. 849–882, 2003.

[17] H. TAN, C. LIU, Y. HUANG, and P. GEUBELLE, "The cohesive law for the particle/matrix interfaces in high explosives," *Journal of the Mechanics and Physics of Solids*, vol. 53, pp. 1892–1917, aug 2005.

[18] A. Needleman, "A continuum model for void nucleation by inclusion debonding," *Journal of Applied Mechanics*, vol. 54, pp. 525–531, 1987.

[19] J. H. Rose, J. Ferrante, and J. R. Smith, "Universal Binding Energy Curves for Metals and Bimetallic Interfaces," *Physical Review Letters*, vol. 47, pp. 675–678, aug 1981.

[20] J. H. Rose, J. R. Smith, and J. Ferrante, "Universal features of bonding in metals," *Physical Review B*, vol. 28, pp. 1835–1845, aug 1983.

[21] A. Needleman, "An analysis of decohesion along an imperfect interface," *International Journal of Fracture*, vol. 42, pp. 21–40, 1990a.

[22] V. Tvergaard and J. W. Hutchinson, "The relation between crack growth resistance and fracture process parameters in elastic-plastic solids," *Journal of the Mechanics and Physics of Solids*, vol. 40, pp. 1377–1397, 1992.

[23] S. Suresh, "Micromechanisms of fatigue crack growth retardation following overloads," *Engineering Fracture Mechanics*, vol. 18, pp. 577–593, jan 1983.

[24] G. Camacho and M. Ortiz, "Computational modeling of impact damage in brittle materials," *International Journal of Solids and Structures*, vol. 33, pp. 2899–2938, 1996.

[25] K. Park and G. H. Paulino, "Cohesive zone models: A critical review of traction-separation relationships across fracture surfaces," *Applied Mechanics Reviews*, vol. 64, 2011.

[26] C. K. Desai, "Determination of numerical cohesive zone length of adhesive joints.," *National Conference on TFMS*, pp. 425–431., 2012.

[27] C. K. Desai, S. Basu, and V. Parameswaran, "Determination of Traction Separation Law for Interfacial Failure in Adhesive Joints at Different Loading Rates," *The Journal of Adhesion*, vol. 92, pp. 819–839, oct 2016.

[28] A. B. Martínez, J. Gámez-Pérez, M. Sánchez-Soto, J. I. Velasco, O. O. Santana, and M. L. Maspoch, "The essential work of fracture (EWF) method analyzing the post-yielding fracture mechanics of polymers," *Engineering Failure Analysis*, vol. 16, no. 8, pp. 2604–2617, 2009.

[29] S.-H. Ahn, M. Montero, D. Odell, S. Roundy, and P. K. Wright, "Anisotropic material properties of fused deposition modeling abs," *Rapid Prototyping Journal*, vol. 8, no. 4, pp. 248–257, 2002.

[30] O. S. Es-Said, J. Foyos, R. Noorani, M. Mendelson, R. Marloth, and B. A. Pregger, "Effect of Layer Orientation on Mechanical Properties of Rapid Prototyped Samples," *Materials and Manufacturing Processes*, vol. 15, pp. 107–122, jan 2000.

[31] Y. Zhao, Y. Chen, and Y. Zhou, "Novel mechanical models of tensile strength and elastic property of FDM AM PLA materials: Experimental and theoretical analyses," *Materials and Design*, vol. 181, p. 108089, 2019.

[32] T. Yao, Z. Deng, K. Zhang, and S. Li, "A method to predict the ultimate tensile strength of 3D printing polylactic acid (PLA) materials with different printing orientations," *Composites Part B: Engineering*, vol. 163, pp. 393–402, 2019.

[33] W. Wu, P. Geng, G. Li, D. Zhao, H. Zhang, and J. Zhao, "Influence of Layer Thickness and Raster Angle on the Mechanical Properties of 3D-Printed PEEK and a Comparative Mechanical Study between PEEK and ABS," *Materials*, vol. 8, pp. 5834–5846, sep 2015.

[34] B. Tymrak, M. Kreiger, and J. Pearce, "Mechanical properties of components fabricated with open-source 3-D printers under realistic environmental conditions," *Materials & Design*, vol. 58, pp. 242–246, jun 2014.

[35] J. J. Laureto and J. M. Pearce, "Anisotropic mechanical property variance between ASTM D638-14 type i and type iv fused filament fabricated specimens," *Polymer Testing*, vol. 68, pp. 294–301, jul 2018.

[36] C. Casavola, A. Cazzato, V. Moramarco, and C. Pappalettere, "Orthotropic mechanical properties of fused deposition modelling parts described by classical laminate theory," *Materials & Design*, vol. 90, pp. 453–458, jan 2016.

[37] I. Durgun and R. Ertan, "Experimental investigation of FDM process for improvement of mechanical properties and production cost," *Rapid Prototyping Journal*, vol. 20, pp. 228–235, apr 2014.

[38] H. Al Abadi, H. T. Thai, V. Paton-Cole, and V. I. Patel, "Elastic properties of 3D printed fibre-reinforced structures," *Composite Structures*, vol. 193, pp. 8–18, 2018.

[39] Y. Song, Y. Li, W. Song, K. Yee, K.-Y. Lee, and V. Tagarielli, "Measurements of the mechanical response of unidirectional 3D-printed PLA," *Materials & Design*, vol. 123, pp. 154–164, jun 2017.

[40] T. Kozior and C. Kundera, "Evaluation of the influence of parameters of fdm technology on the selected mechanical properties of models," *Procedia Engineering*, vol. 192, pp. 463–468, 2017.

[41] C. Valean, L. Maravina, M. Marghita, E. Linul, J. Razavi, F. Berto, and R. Brighenti, "The effect of crack insertion for fdm printed pla materials on mode i and mode ii fracture toughness," *Procedia Structural Integrity*, vol. 28, pp. 1134–1139, 1 2020.

[42] A. Nurizada and K. Kirane, "Induced anisotropy in the fracturing behavior of 3d printed parts analyzed by the size effect method," *Engineering Fracture Mechanics*, vol. 239, p. 107304, 11 2020.

[43] Z. P. Bazant and J. Planas, *Fracture and Size Effect in Concrete and other Quasibrittle Materials.* CRC Press, Boca Raton, 1998.

[44] Z. P. Bazant, I. M. Daniel, and Z. Li, "Size Effect and Fracture Characteristics of Composite Laminates," *Journal of Engineering Materials and Technology*, vol. 118, p. 317, jul 1996.

[45] M. Salviato, K. Kirane, S. Esna Ashari, Z. P. Bažant, and G. Cusatis, "Experimental and numerical investigation of intra-laminar energy dissipation and size effect in two-dimensional textile composites," *Composites Science and Technology*, vol. 135, pp. 67–75, oct 2016.

[46] B. Chen, T. Tay, P. Baiz, and S. Pinho, "Numerical analysis of size effects on open-hole tensile composite laminates," *Composites Part A: Applied Science and Manufacturing*, vol. 47, pp. 52–62, apr 2013.

[47] T. Panneerselvam, S. Raghuraman, and N. V. Krishnan, "Investigating mechanical properties of 3d-printed polyethylene terephthalate glycol material under fused deposition modeling," *Journal of The Institution of Engineers (India): Series C*, vol. 102, pp. 375–387, 4 2021.

[48] J. Maszybrocka, M. Dworak, G. Nowakowska, P. Osak, and B. Łosiewicz, "The influence of the gradient infill of pla samples produced with the fdm technique on their mechanical properties," *Materials*, vol. 15, 2 2022.

[49] S. Rouf, A. Raina, M. I. U. Haq, N. Naveed, S. Jeganmohan, and A. F. Kichloo, "3d printed parts and mechanical properties: Influencing parameters, sustainability aspects, global market scenario, challenges and applications," *Advanced Industrial and Engineering Polymer Research*, vol. 5, pp. 143–158, 7 2022.

[50] V. D. Sagias, K. I. Giannakopoulos, and C. Stergiou, "Mechanical properties of 3d printed polymer specimens," *Procedia Structural Integrity*, vol. 10, pp. 85–90, 1 2018.

[51] J. R. Ai and B. D. Vogt, "Size and print path effects on mechanical properties of material extrusion 3d printed plastics," *Progress in Additive Manufacturing*, vol. 7, pp. 1009–1021, 10 2022.

[52] ASTM, "ASTM D638 - 14 Standard Test Method for Tensile Properties of Plastics,"

[53] R. M. Jones, *Mechanics of Composite Materials*. Philadelphia, PA: Taylor & Francis, 2nd ed., 1999. First edition published 1975.

[54] B. D. Agarwal, L. J. Broutman, and K. Chandrashekhara, *Analysis and performance of fiber composites*. John Wiley, 2006.

[55] Z. P. Bažant, L. Cedolin, W. F. Chen, and E. M. Lui, “ Stability of Structures: Elastic, Inelastic, Fracture and Damage Theories ,” *Journal of Structural Engineering*, vol. 119, no. 3, pp. 1001–1002, 1993.

[56] G. Bao, S. Ho, Z. Suo, and B. Fan, “The role of material orthotropy in fracture specimens for composites,” *International Journal of Solids and Structures*, vol. 29, no. 9, pp. 1105–1116, 1992.

[57] Z. P. Bazant, Y. Xi, and S. G. Reid, “Statistical Size Effect in Quasi Brittle Structures I Is Weibull Theory Applicable,” *Journal of Engineering Mechanics*, vol. 117, pp. 2609–2622, nov 1991.

[58] Dassault Systèmes, Vélizy-Villacoublay, France, *Abaqus 2018 Documentation*, 2018. Version 2018.

[59] B. Cotterell and J. K. Reddel, “The essential work of plane stress fracture.,” *International journal of fracture*, vol. 13, pp. 267–277, 1977.

[60] B. Cotterell, T. Pardoen, and A. G. Atkins, “Measuring toughness and the cohesive stress-displacement relationship by the essential work of fracture concept.,” *Engineering Fracture Mechanics*, vol. 72, pp. 827–848, 2005.

[61] Y. G. Mai and B. Cotterell, “On the essential work of ductile fracture in polymers.,” *International Journal of Fracture*, vol. 32, pp. 105–125, 1986.

[62] B. Cotterell, “The past, present and future of fracture mechanics.,” *Engineering fracture mechanics*, vol. 69, pp. 533–553, 2002.

List of Publications

[**1**] Sumit Patel and C.K.Desai, "Experimental and Numerical Investigation of Fracture Energy and Size Effect in Carbon Powder Reinforced PLA Parts Manufactured by Fused Deposition Modeling," *Journal of The Institution of Engineers (India): Series C,* May 2024.

[**2**] Sumit Patel and C.K.Desai, "Effect of Layer Height on Tensile Strength of Fused Deposited Modeling Printed Carbon Polylactic Acid Part," *International Journal of Scientific Research in Engineering and Management* ISSN: 2582-3930, Volume: 08 Issue: 08, Aug 2024.